ABSTRACT

HEYWARD, IRVINE KEITH. Acoustic Wave Dynamics in the Post-Bounce Phase of Core Collapse Supernovae. (Under the direction of John M Blondin).

How a core collapse supernova successfully “explodes” is only partially understood. Computer models indicate that the accretion shock wave stalls around 200 km from the newly formed proto-neutron star. Despite the abundance of energy from the gravitational collapse and theories predicting how this energy might reenergize the accretion shock, simulations still fail to produce a robust explosion. Hydrodynamic models play an important role in this analysis. I will describe in detail the acoustic waves driven by the PNS and the dissipation of thermal energy by these waves into the critical “Gain Region”. Using the criteria laid out in the Janka model, I will then discuss the impact that this energy has on the restart mechanism. In addition, numerical issues associated with the hydrodynamic supernova model will be discussed.

Acoustic Wave Dynamics in the Post-Bounce Phase of Core Collapse Supernovae

by
Irvine Keith Heyward

A dissertation submitted to the Graduate Faculty of
North Carolina State University
In partial fulfillment of the
Requirements for the degree of
Doctor of Philosophy

Physics

Raleigh, North Carolina

2008

APPROVED BY:

_____	_____
Dr. John M. Blondin Committee Chair	Dr. David Brown
_____	_____
Dr. Pierre A. Gremaud	Dr. Stephen P. Reynolds

DEDICATION

To my father, Ike Heyward, who was interested in everything. He had a passion to understand life, from the physical universe we live in to what lies beyond. No subject was out of bounds, and no rabbit hole was too deep. For my father, life was rich with complexity. There were no short answers, and every topic was worthy of debate.

Some of my fondest memories are sitting at the dinner table with my father, long after the meal was over, discussing science, politics, religion and every subject in between. We did not always share the same views and may not have ever concluded any of our conversations, but it did not matter. Because of my father, I learned that life itself is interesting, and seeking answers to its mysteries is what makes you feel alive. It doesn't matter if the mysteries are ever solved. It is the journey that makes it worthwhile.

Thank you, Dad. I miss our talks.

BIOGRAPHY

It is difficult to know what you want to do with your life when you are young, and it is more difficult to change the path you are on when you are older. I had no aspirations of teaching physics when I was young, though I have always been interested in physics. Fortunately, I had the opportunity to change my path and become a physicist and a teacher. These have always been my life's ambitions. I just didn't know it until I was forty.

"We know what we are, but know not what we may be."

- William Shakespeare, *Hamlet*

ACKNOWLEDGMENTS

It is easy to think of the many deserving people I should thank, though my words here cannot express how sincerely grateful I am for all of the encouragement and guidance I have received. I could not have begun, survived or completed this process without the help of so many unselfish, caring and intelligent people.

I will first and foremost thank my wife, Jane, who is at the top of the list whether ordered chronologically, by importance, or any other scheme. Jane encouraged me to go back to school, which at this stage in our lives was not an easy decision to make. She recognized, perhaps more than I did, how important it was for me to make this life change. The process turned out to be a longer commitment than we anticipated, but regardless, Jane continued to support me in every conceivable way. As I drew closer to finishing my degree, Jane and I talked about the fact that it would soon be her turn to do something for herself. She liked the idea, but did not know what she would do. Now I have finished my degree and will be employed in the fall. It is time for Jane's well deserved turn. I wonder what she will do. I would also like to thank my children, Nat and Corey, for bearing with me all of these years. When I took my first class at NC State in the fall of 2001, Nat was in the 6^{th} grade and Corey was in the 4^{th} grade. Now Corey is getting ready to start her junior year in high school and Nat will be a freshman in college. We all joked about the "scary physics study sessions" I would have at our house. I hope the children have not been permanently damaged by the experience.

From NC State, I would like to thank Michael Paesler who was the Director of Graduate Programs for the Physics Department when I entered the graduate program. Michael was very positive and encouraging when I inquired about the program at NC State.

Though I had been out of school for nearly twenty years and was not involved professionally with math or physics, Michael took a chance and accepted me into the program. Michael is now the Physics Department Head and has hired me to teach physics at the University beginning this fall semester. I doubt that I would be on the verge of a teaching career in physics if not for the encouragement and efforts of Michael Paesler.

I am grateful to my advisor, John Blondin, for taking me into his research group and for providing exceptional guidance and support. Much like my situation when I entered the Graduate School, I entered John's group with little more than a keen interest in astrophysics and computer modeling. If it was a trying experience for John, he never showed it. Thank you, John, for the opportunity, the education and your friendship.

Many people have helped me to appreciate and learn about physics education, including John Blondin, Ruth Chabay, Prabha Ramakrishnan, Bob Beichner, and Bruce Sherwood. I would like especially to thank Bruce for his time as he guided me through my first lecture course and was always available to discuss physics and teaching physics. I fed off of the enthusiasm and teaching knowledge of all of these people and am glad to have that foundation as I embark on my own teaching career.

I would also like to thank my office mates over the years from Daniels, "The Cave" and Riddick for their friendship and willingness to help me through many tough classes. That especially applies to my core study group who were there at the beginning as we learned so much together; Frisco Rose, Ako Emanuel and Trey Walker. Thanks also to Jenny Allen who was Michael Paesler's secretary for many years and was always so cheerful and helpful, and to Andrew Brown for the Python programs he wrote that greatly enhanced my ability to view and evaluate my research data.

I could name nearly every faculty member I know at NC State as someone who helped me in some significant way. That certainly applies to the members of my research committee, and I owe them a debt of thanks. The NCSU Physics Department consists of a wonderful group of individuals, and I feel very fortunate to have received my education there and to have become acquainted with so many thoughtful and interesting people.

TABLE OF CONTENTS

LIST OF FIGURES

ISOTHERMAL ATMOSPHERE

VARYING SOUND SPEED

LIST OF TABLES

Chapter 1 – Introduction

1.1 Core Collapse Supernovae

How a core collapse supernova successfully "explodes" is only partially understood. A star, for the majority of its life, resists collapse under its own gravitational weight by thermal pressure. The energy required to sustain this thermal pressure comes from nuclear reactions in the core of the star, essentially consisting of lighter elements fusing to form progressively heavier elements and releasing energy in the process. Ultimately, if the star is large enough (greater than 8-10 solar masses), iron is produced which has the lowest binding energy of any element. Further fusion with iron to produce heavier elements absorbs energy rather than releases it and the production of thermal energy stops. At this point, without additional thermal energy to resist the inward pull of gravity, pressure in the core builds. This increases the temperature in the core, which in turn cause photodisintegration of iron atoms in an endothermic reaction that escalates the whole process. Soon, the pressure and density reach a critical point where the atomic structure itself collapses in a process known as reverse beta decay where protons and electrons combine to form neutrons and electron neutrinos, and the star begins to collapse under its own weight.

In a fraction of a second, the core of the star, approximately the size of the earth, collapses into a proto-neutron star (hereafter referred to as 'PNS') with a radius of 20 to 50 km. Infalling matter then rebounds off of this newly formed hard core, which has the same density as an atomic nucleus. The still infalling stellar core meets this rebounding matter producing a shock wave that moves away from the PNS. The shock wave slows down as it

expands into an ever larger spherical shell and loses energy through dissipation. When it has traveled only about 200 km from the center, it stalls.

1.2 The Restart Problem

This is where the mystery begins. To create the supernova explosion we observe, the stalled shock wave, known as the "accretion shock", must somehow be reenergized and progress past the outer boundaries of the star. What is the mechanism that causes this restart, and where does the energy come from?

At this moment, according to the Janka model [Janka 2001] the system is very nearly in steady-state, and the star can be thought of in three main regions: 1) the PNS, 2) the post-shock atmosphere between the PNS and the stalled accretion shock and 3) the infalling atmosphere above the accretion shock. Let's do a quick energy budget, starting with the gravitational binding energy released when the core collapses. Using the Newtonian definition of gravitational potential energy, we can find the total potential energy of a self gravitating sphere by integrating over all mass points:

$$U = -\int_m \frac{GM(r)dm(r)}{r},$$

which is equivalent to

$$U = -q\frac{GM^2}{R}, \tag{1.1}$$

where q is a dimensionless constant that depends on the mass distribution of the star. According to Hansen & Kawaler [Hansen 1994] and Cox [Cox 1984] q should be greater than 3/5 (the value for a uniform sphere) but still of order of magnitude 1.0.

Using the approximation that q=1.0 and assuming that a core of 1.2 solar masses (estimates on this mass vary, but approximate values are fine for this "ball park" analysis) is reduced from a sphere the size of the earth to one with a radius of 20 km, energy on the order of 10^{53} ergs is released in the form of neutrinos. 1% of that energy or 10^{51} ergs is absorbed via neutrino capture on neutrons,

$$\nu_e + n \rightarrow e^- + p, \tag{1.2}$$

and to a lesser extent scattering off free nucleons, and ultimately transferred to the kinetic energy of the ejecta [Janka 2001]. Using equation (1.1) again, we can estimate the energy required to expel 15 solar masses of ejecta from the exploding star to be about 10^{50} erg. So in the broad picture, there appears to be enough energy available, but there is trouble in the details.

In his 2001 paper, Janka describes a delicate balance between the mass and energy deposited in the "Gain Region" (refer to Figure 1.1) that is necessary for a successful explosion and how time-dependent variables play a critical role in this balance.

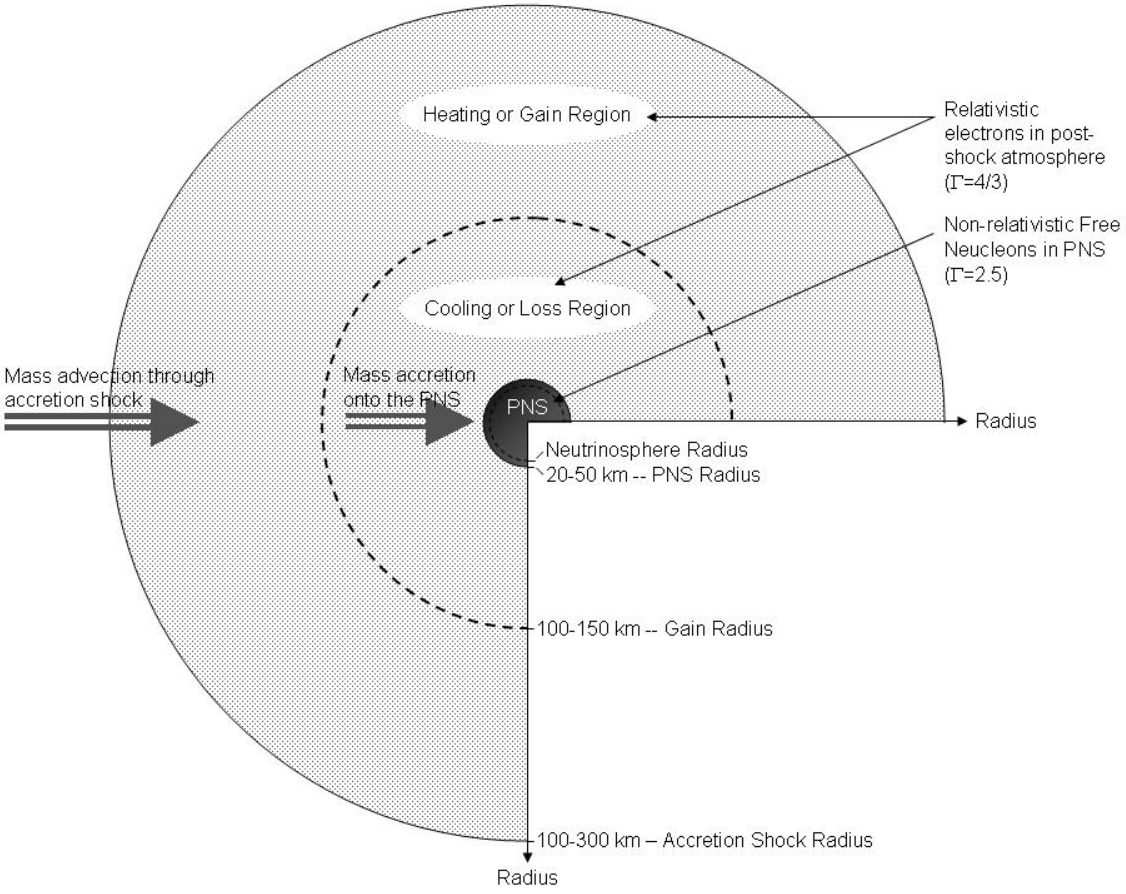

Figure 1.1 - Cross section of inner star during post-bounce phase. Regions correspond to the Janka model. Basic regions are: the "neutrinosphere", which is just inside the PNS radius and is defined by its opaqueness to neutrinos; The PNS, which is defined by non-relativistic free nucleons; the Cooling Region, where net energy is lost, and consists of relativistic free nucleons; and the Gain Region, where net energy is gained and also consists of relativistic free nucleons. The "post-shock atmosphere" discussed in this paper consists of the heating and cooling regions. The net energy gain and loss that defines the Gain and Cooling Regions is determined by neutrino heating and cooling, nuclear reactions and mass flow. The boundary between these two regions is generally about half-way between the PNS and the accretion shock [Janka 2001].

The upshot of Janka's paper is that for the shock to restart and progress, both the mass and energy in the Gain Region must increase over time. Mass is added to the Gain Region when relatively cool matter advects across the accretion shock from the pre-shock

atmosphere. Energy must then be added to the region via neutrino capture (first proposed by Colgate and White [1966]) and convection to compensate for this influx of cool matter. Matter also flows out of the gain region at a rate that depends on how efficiently matter can cool and accrete onto the PNS. This cooling takes place in the "cooling layer" surrounding the PNS as a result of neutrino emissions and convection. The process of cooling and subsequent accretion onto the PNS is slowed by increased neutrino emissions from the stellar core that subsequently heat the matter in the cooling layer.

The PNS is largely opaque to neutrinos which must then escape over time. The generation, release and absorption of neutrinos is a time dependent process that is complicated by many factors, such as: the actively researched equation of state of dense nuclear matter; the neutrino spectra; the dynamical evolution of matter outside the PNS; and the convective currents within the PNS. The time-luminosity profile for neutrino emissions depends on the mechanisms for generation and transport of these neutrinos within the PNS. The transfer of energy to the post-shock atmosphere must also take into account factors such as energy loss from photodisintegration of iron nuclei, the recombination of free nucleons into alpha particles and the degree of secondary neutrino generation and absorption.

The resulting model produces a time evolution of the shock with a tenuous connection to these interacting variables. While there is enough energy to account for a full supernova explosion, a detailed analysis of the time-dependent release and use of that energy, as it is described by Janka, does not guarantee an explosion.

1.3 Restart Theories

Neutrino heating was first proposed by Bethe and Wilson in 1985 as a possible solution to the restart problem [Bethe 1985]. The problem was tackled with 1D simulations until Herant *et al*. [1992] produced the first 2D simulation with neutrino-driven convection in 1992 [Herant 1992]. The significance of hydrodynamic motion of the post-shock gas was recognized by Janka though not initially included in his analysis (with some minor exceptions) as he focused on other aspects of the problem. Many of the subsequent theories seeking an explanation to the mysterious restart of the accretion shock invoke the dynamic motion of acoustic waves in the post-shock region.

A significant study of the hydrodynamic motion of the atmosphere below the stalled shock came in 2003 by Blondin, Mezzacappa & DeMarino [Blondin 2003], where they observed in 2D hydrodynamic simulations that small perturbations grew into large standing acoustic waves between the PNS and the stalled accretion shock. They theorized that once oscillations began (as a result of any random perturbations in the system), they were fed by the dynamic response of the stalled accretion shock causing the oscillations to grow in amplitude. This dynamic was labeled the Spherical Accretion Shock Instability or SASI. The initial study indicated that there were oscillations, dominated by the l=1 mode, which appeared as a sloshing motion of the atmosphere below the accretion shock. In a subsequent study, angular modes were also observed, dominated by the m=1 harmonic, which appears as a spiral motion of the post-shock atmosphere [Blondin 2007]. The angular frequency of both modes was observed in simulations to be approximately 40 radians/second [Blondin 2003 for radial modes & 2007 for non-radial modes].

Foglizzo *et al*. [2007] subsequently proposed the Vortical-Acoustic Instability as another possible mechanism for feeding the growth of the SASI. According to this theory, entropy waves are advected inward (toward the PNS from the accretion shock) by the motion of the post-accretion shock gas. These entropy vorticity waves become pressure waves while still in the post-shock region and then propagate back out toward the accretion shock. These acoustic waves then reinforce the motion of the SASI, causing it to increase in amplitude. According to Foglizzo, *et al*., these radial acoustic waves drive the SASI and are therefore driven themselves at the observed frequency of the SASI frequency, 40 radians/second.

The "Acoustic Heating Mechanism" was postulated by Burrows *et al*. [2006] as another way to deposit thermal energy in the critical Gain Region. According to this theory, the PNS pulsates as a result of turbulence in the surrounding atmosphere. These pulsations in turn drive acoustic waves which dissipate heat as they travel through the post-shock atmosphere and assist in the expansion of the accretion shock. Acoustic waves, in this scenario, are driven by resonant pulsations of the PNS.

Up to now, hydrodynamic models produced by Janka, Blondin, Foglizzo, Burrows and others have only produced marginally better results than the original 2D models used in the 1990's. These hydro models, while producing explosions under certain conditions and exposing key details about the mechanism that drives the shock, have yet to demonstrate the dominant elements in this process and establish a clear path to the explosion. At times, explanations involving acoustic wave dynamics are speculative and may not coincide with realistic wave behavior in the supernova scenario. The possibility looms that all of the pieces have been identified, but each model, while producing significant results in its own right,

simplifies or leaves out entirely key aspects of the entire scheme which then prevents a robust explosion. More recent efforts seeking to incorporate much of the afore mentioned physics have produced some interesting, albeit preliminary, results that are encouraging. All in all, however, success remains tenuous.

1.4 Objectives

The form and location of energy in a developing supernova are integral to the theories that seek to explain how the stalled accretion shock restarts. This paper addresses the transfer of energy between the PNS and the post-shock atmosphere via acoustic waves in the post-shock atmosphere that is critical to these restart theories.

This will be accomplished by providing both a qualitative description of these waves as they propagate from the PNS surface through the hydrostatic post-shocked atmosphere and by providing a quantitative description of the energy dissipated by these waves into the post-shock atmosphere. These acoustic waves are affected by atmospheric conditions including pressure, density, sound speed and gravity that are radially dependent. The effect of these conditions on acoustic waves is studied in a series of test cases that isolate these conditions, culminating in realistic one and two dimensional hydrodynamic models that couple the PNS and post-shock atmosphere. Numerical issues and limitations as they relate to hydrodynamic simulations of the supernova problem will also be addressed. The outline of this paper is as follows:

- Describe the hydrodynamic model that will be used, including the background conditions for the post-bounce phase supernova.

- Discuss the oscillatory behavior of the PNS, which is theorized to be the fundamental source of acoustic waves in the post-shock atmosphere. Both analytical and numerical computer analysis will be used.
- Discuss the effect of specific conditions, such as decreasing background density and sound speed, on the behavior of acoustic waves. Idealized models will be used to isolate these conditions. Each model will be analyzed with both analytical and numerical computer analysis.
- Discuss the effect on acoustic waves due to the dynamic coupling between the PNS and the post-shock atmosphere using one and two dimensional numerical computer analysis.
- Summarize the results and draw conclusions about the impact of acoustic waves in the restart of the accretion shock.

Chapter 2 – Background Topics

This chapter will provide information and explain concepts that will be used throughout this paper. Topics include:

- A description of the hydrodynamic model and of the PNS and post-shock atmosphere in particular.
- Details of the linear analytical analysis that was applied to each atmospheric test model.
- A description of non-linear wave steepening.
- A description of the method used to measure energy dissipation.
- A description of the hydrodynamic code used: VH-1
- A definition of numerical resolution as it is applied in this paper.

2.1 The Hydrodynamic Model

The full hydrodynamic model in this study included the PNS and post-shock atmosphere in an initial state of hydrostatic equilibrium with the self gravity of the system. The stalled accretion shock was not included as this study will only address acoustic waves traveling away from the PNS and within the post-shock region.

During the post-bounce period, an actual supernova is not truly in a state of hydrostatic equilibrium as convection currents move mass and there is a steady flow of matter as it advects across the accretion shock and migrates through the post-shock atmosphere on its way to the PNS [Janka 2000]. The bulk velocity of this mass movement,

however, is small relative to the sound speed of the medium and short duration (< 1 sec) of the stalled accretion shock, and there is little net accumulation of mass in the post-shock region. As a result, it is a reasonable approximation to view the stellar structure in a state of hydrostatic equilibrium [Chevalier 1989; Bethe 1993; Fryer 1996; Janka 2000]. This assumption not only simplifies the dynamic model, but greatly simplifies the determination of the initial state of the system, such as the accretion shock radius and the density and pressure profiles.

The Proto-Neutron Star

The PNS consists primarily of nonrelativistic free nucleons. The thermodynamic properties of this baryon degenerate matter can be modeled with an adiabatic exponent of Γ=2.5 [Bethe 1979]. Though admittedly, little is known about baryon degenerate matter and how it actually responds to changes in pressure and density, this adiabatic exponent has been used with apparent success in many studies related to neutron stars and core collapse supernovae.

The PNS is assumed to be in a state of hydrostatic equilibrium, which means that the bulk velocity of the matter is zero and the pressure gradient balances the self gravity of the system. There are an infinite number of ways to distribute density and pressure so that the PNS is initially in a state of equilibrium. In this paper, the polytropic star model is used to define these states with a single variable, *n*, called the polytropic index, and two boundary conditions (typically the density and pressure at the center of the star).

The polytropic index (which is described in more detail in the Appendix) comes from the following equation that relates pressure and density:

$$p = K\rho^{\left(\frac{n+1}{n}\right)},$$

where K is a constant. When the matter is put into motion, this motion is governed by the Euler equations (to be discussed shortly), which include an internal energy term based on the equation of state:

$$p = S\rho^{\Gamma}, \tag{2.1}$$

where S is a function of entropy and Γ is the adiabatic exponent. The adiabatic exponent in this equation is a constant that represents how pressure and density relate to each other for a given type of matter. Often these two equations are compared to each other to obtain a relationship between n and Γ:

$$\Gamma = \frac{n+1}{n}, \tag{2.2}$$

but this definition of gamma refers strictly to the polytropic (i.e. hydrostatic) state of the star and is not necessarily equivalent to the adiabatic gamma. In this paper, we will avoid this potential confusion by sticking with the previous definitions of Γ as the adiabatic exponent (a property of the material) and n as the polytropic index (defining the initial hydrostatic state). This will be put into practice in the next chapter where a series of tests are conducted with varying polytropic states, defined by n, but only one type of matter, defined by Γ.

Setting $n \neq \Gamma$ requires that entropy vary with position. In an actual stable star, Γ is essentially equal to n because the atmosphere is considered to be adiabatic and isentropic

[Janka 2001]. Ultimately, the models discussed in this paper will use a polytropic index that is equivalent to the adiabatic exponent.

Further details of the polytropic star model can be found in the Appendix.

The Post-Shock Atmosphere

The post-shock atmosphere, which is the region between the PNS and the stalled accretion shock, is dominated by relativistic electrons, positrons and photons. The thermodynamic properties of this matter are modeled as an adiabatic gas with exponent of Γ=4/3. While there are contributions from free nucleons and alpha particles, stretching the adiabatic exponent closer to a value of 1.4 in places, this contribution is small and the entire atmosphere can be well modeled with an adiabatic exponent of 4/3 [Janka 2000; Lattimer & Swesty 1991]. Other common adiabatic exponent values are: Γ=5/3 for a nonrelativistic monatomic gas; Γ=7/5 for a nonrelativistic diatomic gas.

The post-shock atmosphere is assumed to be initially in a state of hydrostatic equilibrium, such that the pressure gradient balances the self gravity of the system and local fluid velocities are zero. Chevalier [1989] and Janka [2000] provide the equations governing this hydrostatic state. The basic relationships are

$$\rho \propto r^{\frac{-1}{(\Gamma-1)}}$$

$$p \propto r^{\frac{-\Gamma}{(\Gamma-1)}}.$$

For Γ=4/3, these states are approximated as

$$\rho = \rho_{sh}\left(\frac{r}{R_{sh}}\right)^{-3} \tag{2.3}$$

$$p = p_{sh}\left(\frac{r}{R_{sh}}\right)^{-4}, \tag{2.4}$$

Where the 'sh' subscript refers to values just behind the accretion shock front. The shock radius is set by the mass accretion rate, $\dot{M}$, which has different theoretical values. Refer to Chevalier [1989] for these theoretical values and resultant shock radii. The shock parameters are further defined by

$$\rho_{sh} = 7\rho_0$$

$$p_{sh} = {}^{6}\!/_{7}\,\rho u_{in}^2$$

$$u_{in} = \left(\frac{2GM}{r_{sh}}\right)^{1/2},$$

where

$$\rho_0 = \frac{\dot{M}}{4\pi r_{sh}^2 u_{in}}$$

The Hydrodynamic Equations

The motion and properties of the PNS and surrounding atmosphere are governed by Euler's equations for inviscid compressible fluid flow:

Continuity (or mass): $\rho_t + \nabla \cdot (\rho \boldsymbol{u}) = 0$, (2.5)

Momentum: $(\rho \boldsymbol{u})_t + \nabla \cdot (\rho \boldsymbol{u}^2) + \nabla p = \rho \boldsymbol{g}$, (2.6)

Energy: $$(\rho \mathrm{E})_t + \nabla \cdot (\rho \boldsymbol{u} \mathrm{E}) + \nabla \cdot (\boldsymbol{u} p) = 0, \tag{2.7}$$

where ρ is the density, p is the pressure, $\boldsymbol{u}$ is the velocity vector, $\boldsymbol{g}$ is the acceleration vector due to gravity and E is the total energy per unit mass of the system. This energy is defined as

$$\mathrm{E} = \tfrac{1}{2}\boldsymbol{u}^2 + \frac{1}{(\Gamma - 1)}\frac{p}{\rho} + \Phi, \tag{2.8}$$

and the gravitational potential, Φ, is defined by Poisson's equation for Newtonian gravity as

$$\nabla^2 \Phi = 4\pi G \rho. \tag{2.9}$$

We can also recognize that $\boldsymbol{g}$ and Φ are related by the equation

$$\boldsymbol{g} = -\nabla \Phi$$

The three terms in the energy equation (2.8) represent kinetic energy, internal energy and potential energy, respectively. In the internal energy term, Γ is the adiabatic exponent, which is a property of the material and describes how density and pressure relate to each other. Note that there are actually 3 adiabatic exponents (Γ_1, Γ_2 and Γ_3), which are discussed in more detail when the "Linear Adiabatic Wave Equation" for the PNS model is derived in section 3.2. The adiabatic exponent used here in the internal energy term is actually Γ_3, and the adiabatic exponent used later in the equation of state, $p=S\rho^{\Gamma}$, is Γ_1. In our case, however, which is that of degenerate matter, all three adiabatic exponents are equivalent [Hansen 1994]. Because of this fact, Γ will be written without a subscript in this paper to represent any one of the three adiabatic exponents.[1]

[1] Also worth noting is that you often see the equation of state written with a lower case gamma ($p=S\rho^{\gamma}$), but this can be confusing as a lower case gamma also refers to the ratio of specific heats: $\gamma=c_p/c_v$. This definition of gamma is not always equivalent to Γ_1 (or any other adiabatic exponent for that matter). Case in point, for an ideal gas, $\gamma=\Gamma_1=\Gamma_2=\Gamma_3$, but for the case of a degenerate gas, $\Gamma_1=\Gamma_2=\Gamma_3$ and $\gamma=\infty$ [Hansen 1994].

The hydrodynamic equations above are valid under the following assumptions:

- All interactions are adiabatic
- There are no net changes in chemical composition
- Fluid velocities are non-relativistic
- Space is “flat” such that the Newtonian definition of gravity is valid
- There are no magnetic forces (though this could be added)

2.2 Linear Analytical Analysis

Analytical analysis is performed in this study with linear theory. Acoustic waves in the post-shock atmosphere are expected to become non-linear as their amplitudes approach the sound speed of the atmosphere, and the resultant equations cannot be solved analytically. For small disturbances, however, these waves are linear to within a small error. This is the basis of linear theory, where the products of small perturbations to the background are neglected so that the hydrodynamic equations reduce to the linear wave equation, which can be solved analytically. This assumption of linearity will be used to find analytical solutions for PNS oscillations and dispersion relations for each idealized atmospheric model.

Following is the linear analytical derivation of the wave equation for a plane wave in a uniform atmosphere. This is the first test model discussed in Chapter 4 and is presented here as an example of the basic procedure that was used to solve each of the test models in Chapter 4.

To derive the analytical result in this case, we will start with Euler's equations for momentum and energy in 1D, Cartesian coordinates:

$$(\rho u)_t + (\rho u^2)_x + p_x = -\rho g \tag{2.10}$$

$$(\rho E)_t + (\rho u E)_x + (up)_x = 0\,, \tag{2.11}$$

where the minus sign on ρg comes from the direction of the gravitational force since g is no longer written as a vector. The 't' and 'x' subscript notation will be used throughout this paper to represent the time and spatial partial derivatives. Set g=0 and apply the following linear perturbations to pressure, density and velocity:

$$p = p_e + p' \tag{2.12}$$

$$\rho = \rho_e + \rho' \tag{2.13}$$

$$u = u_e + u' , \tag{2.14}$$

where p_e, ρ_e, and u_e are the unperturbed or equilibrium values, which are in general functions of x only, and p', ρ', and u' are the perturbed values, which are functions of t and x. For *this case*, p_e and ρ_e are constant in space and u_e=0, so the perturbations may be written:

$$p = p_c + p'$$

$$\rho = \rho_c + \rho'$$

$$u = u' ,$$

where p_c and ρ_c are constants. Looking first at the total energy, defined by equation (2.8), we see that the kinetic energy term can be neglected because it contains the product of small perturbed values, and the potential energy term can be deleted because there is no gravity. As a result, the total energy simplifies to just the internal energy term:

$$E = \frac{1}{(\Gamma - 1)} \frac{p}{\rho} . \tag{2.15}$$

Substituting (2.15) into (2.11), we get

$$p_t + (up)_x + (\Gamma - 1)(up)_x = 0 . \tag{2.16}$$

Now applying the linear perturbations to (2.10) and (2.16) and again dropping the terms that contain products of perturbed values, we get

$$(\rho_c u')_t + p'_x = 0 \tag{2.17}$$

$$p'_t + \Gamma (p_c u')_x = 0 . \tag{2.18}$$

By taking the time derivative of (2.17) and the spatial derivative of (2.18), we obtain

$$\rho_c u'_{tt} + p'_{xt} = 0 \tag{2.19}$$

$$p'_{xt} + \Gamma p_c u'_{xx} = 0 , \tag{2.20}$$

and then subtracting (2.19) from (2.20), we eliminate the p' terms and obtain the wave equation for the perturbed velocity:

$$u'_{tt} - \Gamma \frac{p_c}{\rho_c} u'_{xx} = 0 . \tag{2.21}$$

We can similarly obtain the wave equation for pressure by taking the time derivative of (2.18), the spatial derivative of (2.17) and subtracting the results to eliminate the velocity terms.

Before finding the solution for u' in equation (2.21), we observe that the coefficient in front of the second term is constant and equal to the square of the phase velocity or sound speed. Therefore, in *this* case, we can write the square of the sound speed as

$$c_s^2 = \Gamma \frac{p_c}{\rho_c} , \tag{2.22}$$

and rewrite equation (2.21) as

$$u'_{tt} - c_s^2 u'_{xx} = 0 , \tag{2.23}$$

where the sound speed, in *this* case, is constant in space and time. The solution to this wave equation is known by inspection, but for the purpose of evaluating more complex wave

equations in Chapter 4, the solution will be derived explicitly here, establishing the basic procedure.

Begin by using the separation of variables technique. Substitute

$$u' = X(x)T(t) \tag{2.24}$$

into the wave equation, (2.23), to obtain

$$XT_{tt} - c_s^2 TX_{xx} = 0. \tag{2.25}$$

Divide (2.25) by XT to obtain

$$\frac{T_{tt}}{T} - c_s^2 \frac{X_{xx}}{X} = 0. \tag{2.26}$$

Equation (2.26) is only true in general if the following equations are true:

$$\frac{T_{tt}}{T} = -\omega^2 \tag{2.27}$$

$$c_s^2 \frac{X_{xx}}{X} = -\omega^2, \tag{2.28}$$

where $-\omega^2$ is an arbitrary constant. The constant has been written in this form for convenience as ω later turns out to be the oscillation frequency of the system. Equations (2.27) and (2.28) can be rewritten as:

$$T_{tt} + \omega^2 T = 0 \tag{2.29}$$

$$X_{xx} + \frac{\omega^2}{c_s^2} X = 0. \tag{2.30}$$

Equations (2.29) and (2.30) are 2nd order ordinary differential equations with respective general solutions:

$$T = C_1 \,\mathrm{Re}\left(e^{\pm i\omega t}\right) \tag{2.31}$$

$$X = C_2 \,\mathrm{Re}\left(e^{\pm ikx}\right), \tag{2.32}$$

where C_1 and C_2 are arbitrary constants, k is the wave number (ω / c_s), and ω can now be seen from equation (2.31) to be the angular frequency of the system. Substituting (2.31) and (2.32) back into the original definition of u', equation (2.24), we finally obtain the solution to the perturbed velocity wave equation:

$$u' = u_0 \,\mathrm{Re}\left(e^{i(\omega t \pm kx)}\right),$$

which can be written as

$$u' = u_0 \cos\left(\omega t \pm kx\right), \tag{2.33}$$

where u_0 represents the amplitude of the perturbation velocity, u'.

2.3 Non-Linear Waves

As will be demonstrated with the test models in chapter 4, every acoustic wave has a tendency to steepen and develop into a shock. Even a very small disturbance in a uniform medium will develop into a shock, though over a greater distance scale. This is supported by the 1-D analysis of acoustic waves in an isentropic ideal gas by Shu [1992]. A summary of this analysis, with some elaboration, follows.

Begin with the continuity and momentum equations in 1-D:

$$\rho_t + (\rho u)_x = 0 \tag{2.34}$$

$$(\rho u)_t + (\rho u^2)_x + p_x = 0\,. \tag{2.35}$$

Expanding the derivatives in equation (2.35), the equation becomes

$$\rho_t u + \rho u_t + (\rho u)_x u + \rho u u_x + p_x = 0$$

or

$$u[\rho_t + (\rho u)_x] + \rho u_t + \rho u u_x + p_x = 0$$

and finally

$$\rho u_t + \rho u u_x + p_x = 0\,, \tag{2.36}$$

because the term in square brackets is zero from equation (2.34). Now consider the definition of sound speed:

$$c_s^2 \equiv \left(\frac{\partial p}{\partial \rho}\right)_S . \tag{2.37}$$

For an isentropic system, this is an exact differential:

$$c_s^2 = \frac{dp}{d\rho}\,,$$

which can then be written

$$p_x = c_s^2 \rho_x .$$

Using this relationship to replace p_x in equation (2.36), we obtain

$$\rho u_t + \rho u u_x + c_s^2 \rho_x = 0 . \tag{2.38}$$

We still have three variables in this equation, ρ, u and c_s, but ρ can be eliminated by writing it in terms of c_s. Substitute the equation of state, $p = S\rho^{\Gamma}$, into the sound speed equation (2.37) to obtain the isentropic sound speed:

$$c_s = \sqrt{\Gamma S}\,\rho^{\frac{1}{2}(\Gamma-1)} .$$

Take the derivative of the sound speed to obtain

$$dc_s = \sqrt{\Gamma S}\,\tfrac{1}{2}(\Gamma-1)\rho^{\frac{1}{2}(\Gamma-1)-1} d\rho = \tfrac{1}{2}(\Gamma-1) c_s \frac{d\rho}{\rho}$$

or

$$\frac{d\rho}{\rho} = \frac{2}{(\Gamma-1)} \frac{dc_s}{c_s} . \tag{2.39}$$

Before applying equation (2.39), divide equations (2.34) and (2.38) by ρ to get

$$\frac{\rho_t}{\rho} + \frac{\rho_x}{\rho} u + u_x = 0$$

$$u_t + u u_x + c_s^2 \frac{\rho_x}{\rho} = 0 .$$

Now apply equation (2.39) and these two equations become

$$\frac{2}{(\Gamma-1)} \frac{(c_s)_t}{c_s} + \frac{2}{(\Gamma-1)} u \frac{(c_s)_x}{c_s} + u_x = 0$$

$$u_t + u u_x + c_s^2 \frac{2}{(\Gamma-1)} \frac{(c_s)_x}{c_s} = 0$$

or

$$\frac{2}{(\Gamma-1)}(c_s)_t + \frac{2}{(\Gamma-1)}u(c_s)_x + c_s u_x = 0 \tag{2.40}$$

$$u_t + uu_x + \frac{2}{(\Gamma-1)}c_s(c_s)_x = 0. \tag{2.41}$$

We can obtain the characteristic equation by adding (2.40) and (2.41). Initially, this gives us

$$\left(\frac{2}{(\Gamma-1)}c_s + u\right)_t + u\left(\frac{2}{(\Gamma-1)}c_s + u\right)_x + c_s\left(\frac{2}{(\Gamma-1)}c_s + u\right)_x = 0.$$

Then by separating out the time and spatial operators, we get the characteristic equation:

$$\left[\frac{\partial}{\partial t} + (u + c_s)\frac{\partial}{\partial x}\right]\left(\frac{2}{\Gamma-1}c_s + u\right) = 0. \tag{2.42}$$

This characteristic equation gives us great insight into the dynamics of these acoustic waves. The operand (in large parenthesis) is an invariant quantity (with respect to this differential operator) known as the Riemann Invariant or characteristic. Defining this invariant as Q, the characteristic equation becomes:

$$Q_t + (u + c_s)Q_x = 0.$$

This equation describes the propagation of the characteristic Q for an acoustic wave, whether linear or nonlinear. The invariant characteristic wave propagates with velocity ($u + c_s$), where u is the velocity of the disturbance relative to the background sound speed, c_s. ($u + c_s$) is also the local velocity of the disturbance, which tells us that the peak of the wave is traveling at $c_s + u_0$, the trough of the wave is traveling at $c_s - u_0$ and the undisturbed 'middle' of the wave is traveling at c_s. Thus for any sound wave, steepening occurs, and if the steepening progresses far enough, a shock will form and the amplitude will decay. Even in

the linear regime where $u_0 << c_s$ and the difference between peak and trough velocities is very small, the steepening still occurs, albeit very slowly.

By this analysis, a perfect sine wave will travel with a constant amplitude until the peak catches up with the trough. The distance that the wave travels before this happens depends on the amplitude of the velocity perturbation. This can be seen in the *x*-*t* plot in Figure 2.1 that shows the first, third and fifth cycles of a Mach[2] 0.1 numerical simulation that was performed with the uniform atmosphere model to be covered in the next chapter. The three light lines track the peak, trough and undisturbed paths in space time. By the third cycle, the projected wave peak has passed the projected wave trough creating an unphysical situation. In reality, viscous forces in the atmosphere maintain a nearly vertical wave front (a shock wave) and in the process, reduce the amplitude, dissipate heat and create a discontinuity in atmospheric properties.

[2] Mach is the fraction of the perturbed velocity amplitude to the sound speed: $M = u_0 / c_s$

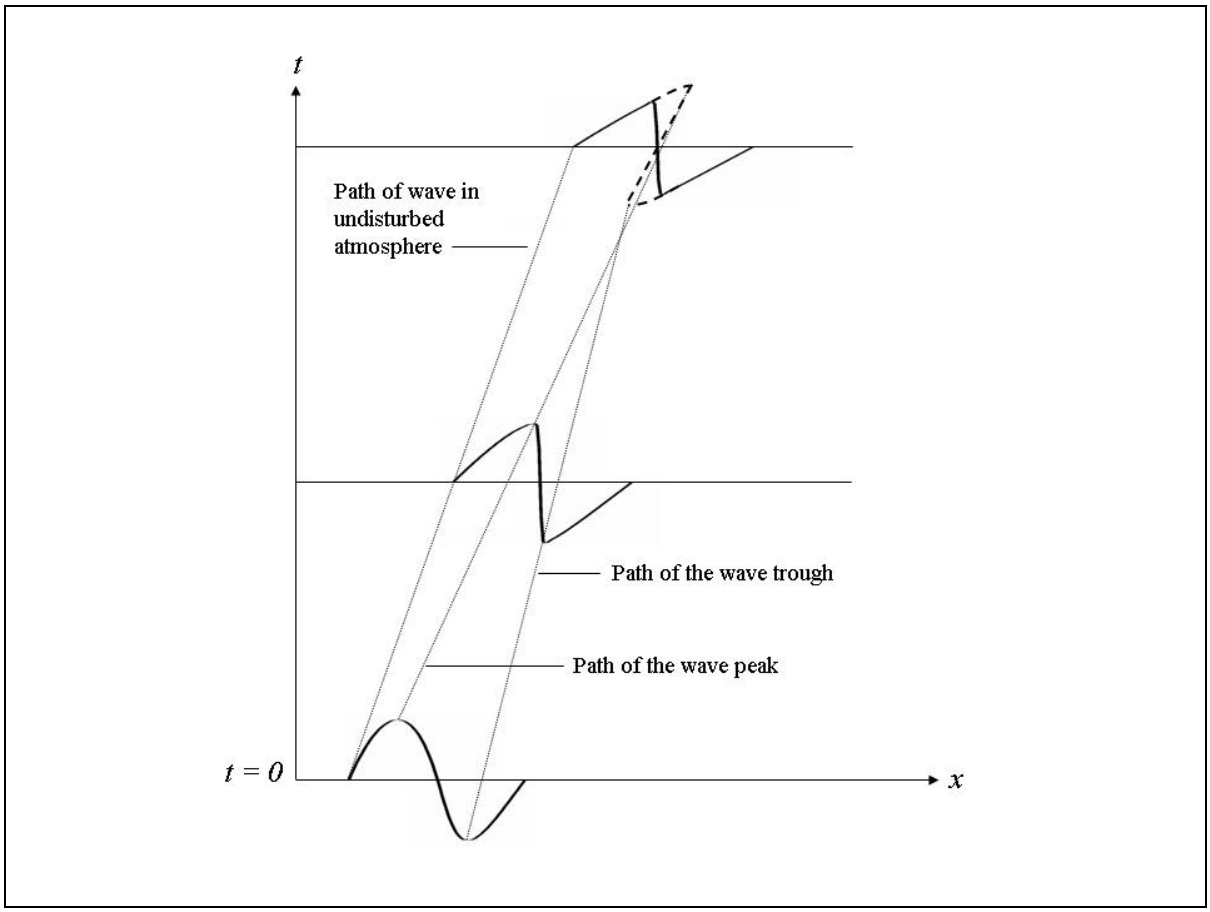

Figure 2.1 - Wave steepening and amplitude reduction of a Mach 0.1 velocity wave in a uniform atmosphere. The heavy dashed line shows the non-physical portion of the wave that must be dissipated by viscous forces. The waves in the plot are the 1st, 3rd and 5th cycles generated in a numeric simulation to be discussed in Section 4.2.

How far will a wave travel before it develops into a full shock? The time it takes for the peak to catch up with the trough is the relative distance between the peak and trough divided by the relative velocity, which is

$$\Delta t = \frac{\frac{1}{2}\lambda}{2u_0},$$

where λ is the wavelength, which is the sound speed divided by the frequency, so this equation becomes

$$\Delta t = \frac{\frac{1}{2}\left(\frac{c_s 2\pi}{\omega}\right)}{2u_0} = \frac{\pi c_s}{2\omega u_0}.$$

The distance that a wave travels in this time period is simply $c_s \cdot \Delta t$, which is then

$$\frac{\pi c_s^2}{2\omega u_0} \tag{2.43}$$

or

$$\frac{\lambda}{4M}. \tag{2.44}$$

Equation (2.43) shows us that the point where steepening begins is not only velocity dependent but also frequency and sound speed dependent, and equation (2.44) shows us that the number of wavelengths traveled before the amplitude begins to decay is simply $1/(4M)$. We can now see that the reason we do not experience much energy dissipation for a low Mach value such as .001, is that the shock does form until the wave has traveled 250 wavelengths. On the other hand, at Mach 1 the shock wave forms and energy dissipation begins in earnest after only a quarter of a wavelength.

2.4 Energy Dissipation

The analysis of energy dissipation by acoustic waves is central to this study. Fundamentally, we are interested in the rate that wave energy is dissipated and deposited into the surrounding medium as heat. Ideally, the energy lost by these acoustic waves is exactly equal to the thermal energy added to the medium so that the total energy is constant. As it turned out, in the numerical simulations to be discussed, the total energy in the simulation volume decreased over time because mass slowly advected out of the outer boundary carrying energy with it. This decreasing density is discussed in Chapter 4 for each atmospheric test case.

This bulk motion of the atmosphere causes some complications in the study as energy is added by acoustic wave dissipation and lost by this motion. If we consider a volume that expands with this bulk motion, then the expansion is adiabatic and we can separate out the change in internal energy due to expansion from the change in internal energy due to wave dissipation. During adiabatic expansion, the entropy is constant while the temperature, internal energy and of course density all change. On the other hand, when heat is added to the atmosphere by shocked wave dissipation, density is constant while temperature, internal energy and entropy all change. We can see how temperature and internal energy are functions of both entropy and density by quickly studying the appropriate equations. This will also give us insight into how the thermal energy added to the atmosphere by wave dissipation can be measured even while the atmosphere expands, which is ultimately the goal.

Start with internal energy per unit volume, which is

$$e = \frac{1}{(1-\Gamma)} p \, .$$

Using the equation of state, $p=S\rho^{\Gamma}$, this becomes:

$$e = \frac{1}{(1-\Gamma)} S\rho^{\Gamma} \, . \tag{2.45}$$

Now recognize two conditions:

1. When heat is added to the atmosphere, S increases and ρ is constant.
2. During the adiabatic expansion, S is constant and ρ decreases.

Therefore, S and ρ are independent variables and a change in e can be defined as

$$de = \left(\frac{\partial e}{\partial \rho}\right)_S d\rho + \left(\frac{\partial e}{\partial S}\right)_\rho dS \, .$$

The first term is the change in internal energy due to adiabatic expansion and the second term is the change due to heat transfer, which is the quantity we are interested in. Using the definition of internal energy from equation (2.8) and taking the derivative, we can write the change in internal energy due solely to heat transfer as

$$de_Q = \frac{1}{(1-\Gamma)} \rho^{\Gamma} dS \, ,$$

where the Q subscript indicates the change in internal energy due solely to heat transfer. Multiplying both sides by S, we get

$$Sde_Q = \frac{1}{(1-\Gamma)} S\rho^{\Gamma} dS \, ,$$

and again applying equation (2.45), this becomes

$$Sde_Q = edS$$

or

$$\frac{de_Q}{e} = \frac{dS}{S}. \tag{2.46}$$

So, we can measure the fraction of internal energy that changes solely due to heat transfer by measuring the fractional change in S!

We can use the same approach with temperature. From the ideal gas law, we can write temperature as

$$T = \frac{V}{nR} p,$$

written this way because V, n and R are constants in this case. Using the equation of state, we can substitute for p to obtain

$$T = \frac{V}{nR} S\rho^{\Gamma}. \tag{2.47}$$

Using the same reasoning as before, the change in temperature due solely to heat transfer is

$$dT_Q = \left(\frac{\partial T}{\partial S}\right)_{\rho} dS$$

or

$$dT = \frac{V}{nR} \rho^{\Gamma} dS.$$

Using equation (2.47), this can finally be written as

$$\frac{dT_Q}{T} = \frac{dS}{S}. \tag{2.48}$$

Just as with internal energy, we see that the fractional change in temperature due solely to heat transfer is equivalent to the fractional change in S!

Dividing both sides of equations (2.46) and (2.48) by the elapsed time, we now have a way in the numerical simulations to measure the rate of change of the energy fraction and temperature fraction. From here on, I will use the fractional rate of change of entropy ($dS/S/\Delta t$) to represent the fractional rate of change of either temperature or internal energy due to the transfer of heat. The one caveat to this method is that in the numerical simulations, the calculation volume is fixed. This means that the internal energy associated with the matter that moves out of the calculation volume will not be accounted for. In many simulations, we will see that the mass pushed out contains little thermal energy; however, this is an issue that must be considered in the final analysis.

One note on doing these calculations in the computer simulation: The fractional rate of change of entropy was calculated by $(S_f - S_i)/S_i/\Delta t$. As energy carried by acoustic waves was cyclical, the average entropy needed to be recorded over complete periods. To eliminate calculation errors that would be caused by the time step not landing precisely on the start and stop of each period, the time step in the program was adjusted dynamically to land precisely at these times.

2.5 The Hydrodynamic Program and Numerical Resolution

Numerical simulations were performed with VH-1, which is a multi-dimensional Lagrangian hydrodynamics program written in 1990 and 1991 by the numerical astrophysics group at the University of Virginia, including John Hawley, John Blondin, Greg Lindahl, Eric Lufkin and Kazimierz Borkowski. VH-1 uses the piecewise parabolic method described by Collella and Woodward [Colella 1984] to solve the equation of ideal, inviscid, compressible fluid flow described earlier in this chapter.

Numerical zones are evenly spaced along the spatial axis, and numerical zones per wavelength will be used to represent the resolution of a given computer simulation. As variables (such as density, pressure and velocity) are sinusoidal, steep parts of data curves, where data change rapidly, are not resolved as well as horizontal parts of these curves, where data change slowly. Using zones per wavelength, as I have done, understates the resolution in flat parts of the cycle and overstates it in steep parts of the cycle. For a purely sinusoidal wave, the number of zones per wavelength still allows us to compare the resolution between simulations, as the resolution scales everywhere on the curve the same. As a result the number of zones per wavelength is representative of the number of zones anywhere on the data curve and suits the purpose of this analysis.

In several models, the wavelength varies with distance, so zones per wavelength also varies. In these cases, I will define a point in space where the resolution (zones per wavelength) will be defined, usually at the PNS surface or a mid-way point in the post-shock atmosphere.

Chapter 3 – PNS Oscillations

3.1 General

In this chapter, I will discuss the natural radial oscillation frequency of the PNS using analytical and numerical analyses. With this frequency, I will then derive the peak surface velocity of a pulsating PNS.

In 1980, John P. Cox published radial mode oscillation frequencies of various polytropic stars determined analytically using an adiabatic exponent of Γ=5/3 [Cox 1980]. This analysis is described below. While the PNS in our model has an adiabatic gamma of 2.5, the Γ=5/3 analysis provides a qualitative understanding of PNS oscillation modes and frequencies. In chapter 5, the fundamental oscillation frequency of the PNS in the full coupled system with a PNS adiabatic gamma of 2.5 will be determined.

3.2 Analytical Analysis of PNS Oscillations

To describe the behavior of the PNS, Cox derived the "linear adiabatic wave equation" (LAWE) [Cox 1980]:

$$\frac{d}{dr}\left(\Gamma_1 p r^4 \frac{d\xi}{dr}\right) + \xi\left\{\sigma^2 \rho r^4 + r^3 \frac{d}{dr}\left[\left(3\Gamma_1 - 4\right)p\right]\right\} = 0\,,$$

where ξ is the pulsation amplitude, σ is the angular pulsation frequency, and they are defined by the relationship

$$\frac{\delta r}{r} = \xi(r)e^{i\sigma t}\,.$$

The LAWE is essentially an eigenvalue problem, yielding an infinite set of eigenfrequencies, σ, and eigenfunctions, ξ, that satisfy the 'standing wave' boundary conditions, which are:

1) By symmetry, there is no displacement at the center, i.e. at $r = 0$, $\delta r = 0$

2) Pressure vanishes o/s star, i.e. at $r = R$, $\delta p = 0$

According to Cox though, only the lowest or fundamental eigenfrequency needs to be considered, because higher order frequencies dissipate more quickly as nonadiabatic effects and friction become more significant.

Note that the only adiabatic exponent that appears in the LAWE is Γ_1. This is due to the fact that Γ_1, Γ_2 and Γ_3 are related to each other by their defining equations (shown on the next page), that eliminate one exponent. A second can be dropped when it is assumed that motion is adiabatic.

Derivation of the LAWE

Following is an overview of Cox's derivation of the Linear Adiabatic Wave Equation (LAWE).

As with the numerical model, the LAWE is derived from the Euler equations for an inviscid compressible gas and an energy equation:

$$\rho_t + \nabla \cdot (\rho \boldsymbol{u}) = 0$$

$$(\rho \boldsymbol{u})_t + \nabla \cdot (\rho \boldsymbol{u}^2) + \nabla p = \rho \boldsymbol{g}$$

$$(\rho E)_t + \nabla \cdot (\rho \boldsymbol{u} E) + \nabla \cdot (\boldsymbol{u} p) = 0$$

$$E = \tfrac{1}{2}u^2 + \frac{1}{(\Gamma_1 - 1)}\frac{p}{\rho} + \Phi .$$

The following adiabatic exponents are then substituted into the Euler equations:

$$\Gamma_1 = \left(\frac{d \ln p}{d \ln \rho}\right)$$

$$\Gamma_3 - 1 = \left(\frac{d \ln T}{d \ln \rho}\right)$$

$$\frac{\Gamma_2 - 1}{\Gamma_2} = \left(\frac{d \ln T}{d \ln p}\right).$$

The results are further simplified by the same set of assumptions used in the numerical model:

- All interactions are adiabatic
- There are no changes in chemical composition
- Fluid velocities are non-relativistic
- Space is "flat" such that Newton's law of gravity is valid
- There are no magnetic forces
- The perturbation of velocity, pressure and density are small compared to the background values

and still further simplified by the following assumptions:

- Spherical symmetry
- The temperature gradient with radius is smooth (i.e. local temperature doesn't change much with radius)

- Γ_1 is constant throughout the PNS
- No turbulence

As a matter of interest, according to Cox, when the analysis is performed without the assumptions that the system is adiabatic and linear, the resulting frequencies are only different by a few percentage points.

The fundamental oscillation frequencies found by Cox are shown at the end of this chapter in Table 3.1.

3.3 Numerical Analysis of PNS Oscillations

The objective was to set up a computer simulation with just the PNS using an adiabatic exponent of 5/3 to match the analytical analysis. To prevent calculation errors in the computer simulation as a result of zero density, an atmosphere also had to be included around the PNS. To minimize the effect of the atmosphere so that the numerical results could be compared directly to the analytical results, a very thin atmosphere ($\rho_{atm} << \rho_{pns}$) was used.

Simulations were run on a spherical coordinate grid in one dimension (with radius as the variable dimension). One dimension sufficed as Cox's analysis assumed angular symmetry. Simulations were run with polytropic states of n = 1.0, 1.5, 2.0, 3.0, 3.5 and 4.0, which are shown in Figure 3.1.

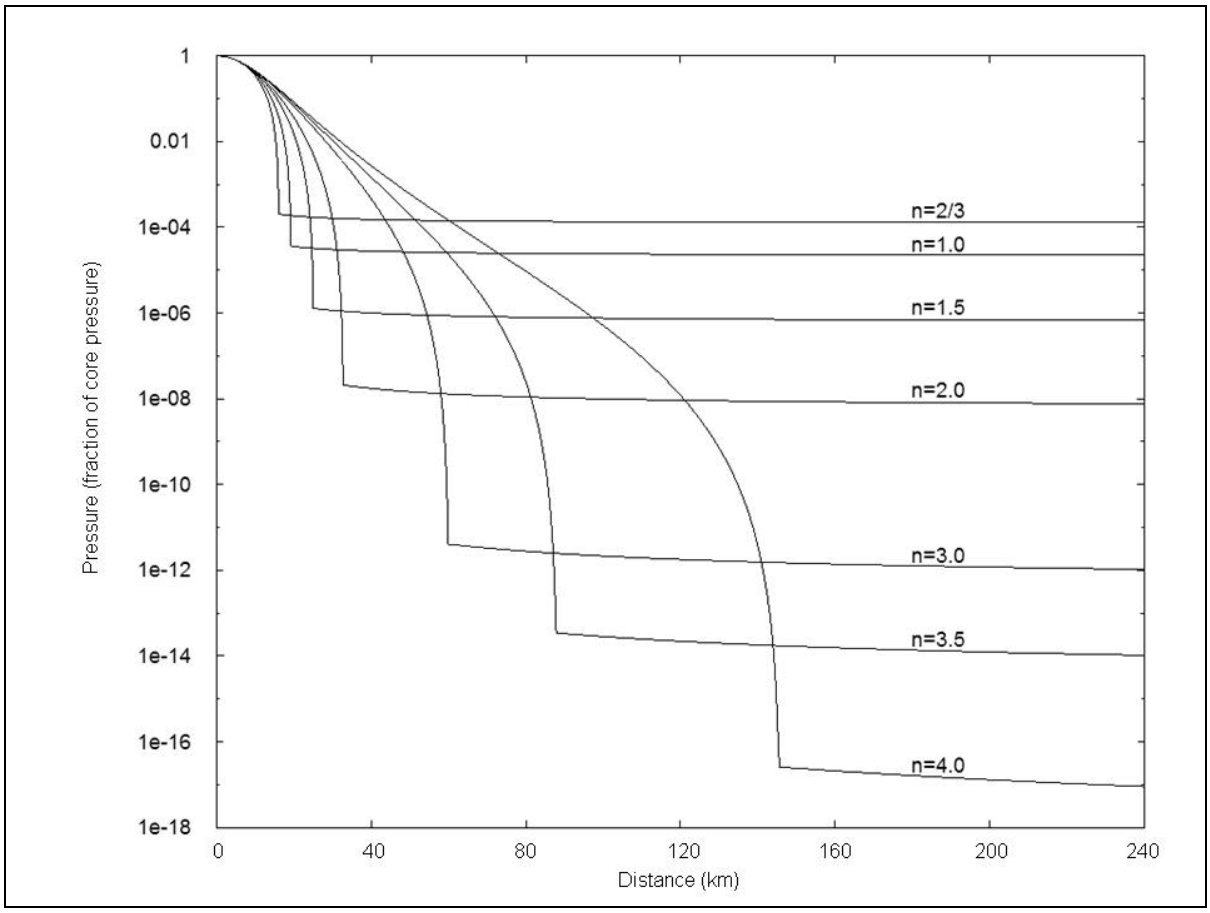

Figure 3.1 – Pressure for the initial polytropic states used in the analytical and numerical tests. The n=2/3 curve is shown here as it is the polytrope used in the full coupled model discussed in Chapter 5, however, it was not included in the analysis by Cox nor in the numerical simulations in this section.

To begin the simulation, the system was established in a state of hydrostatic equilibrium with one of the polytropic states indicated above. Radial oscillations were then initiated by perturbing the PNS (pressure or velocity). These oscillations were tracked by recording the central pressure of the star over time. As an example, Figure 3.2 shows these oscillations for a polytropic index of n=3.0. The oscillation initially included higher order harmonics, but these higher orders died out quickly so that only the fundamental frequency

remained. The first and second harmonics were extracted from this waveform and are also shown in Figure 3.2. The star oscillations in general were damped as the oscillation energy of the PNS was transferred into acoustic wave energy in the surrounding atmosphere. Higher order frequencies were damped more quickly as acoustic waves with greater frequency would draw energy away at a greater rate. Cox also points out that higher orders attenuate faster because temperature and pressure gradients are steeper which creates greater viscous forces [Cox 1980].

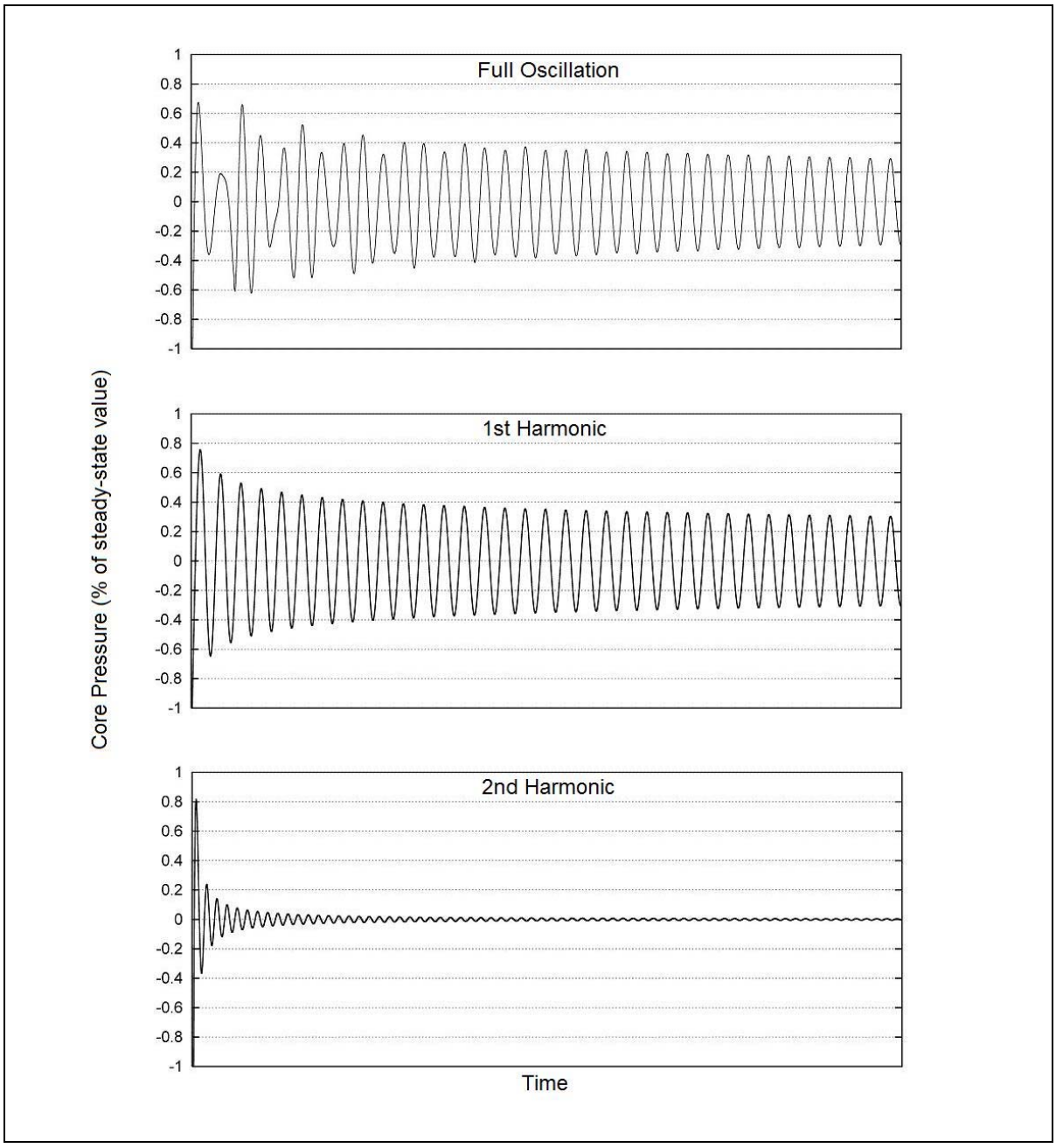

Figure 3.2 – Pressure oscillations of the PNS core for a numerical simulation with an $n = 3.0$ polytrope. The oscillation wave consists almost entirely of the 1st and 2nd harmonic, which are separated out in the Figure.

As it turned out when running numerical simulations, it was not easy to create steady-state oscillations for the n=3.5 and n=4.0 polytropic states. Pressure and density slope more gradually with radius and extend further out into the atmosphere for larger values of n. Essentially, with larger values of n, the point where the star ends and the atmosphere begins is less defined. This can be seen in Figure 3.1. As a result, as soon as the oscillations began in the simulation, the outer portion of the star spread into the atmosphere carrying the oscillation energy with it. This effect was not as dramatic for the n=3.5 polytrope and the star did resonate but not at the precise frequency predicted by Cox. As can be seen in the simulation, the pressure and density profiles of the star were altered enough, essentially moving the point where the star ends, that it became a different polytropic state, which therefore had a different resonant frequency. As a result, the star did resonate, but the frequency was somewhat different than that predicted by Cox [refer to Table 3.1].

That is not to say that it is impossible to create oscillations for the n=3.5 and n=4.0 polytropes. The oscillations that were observed for the n=3.5 polytrope, were achieved by adjusting the profile of the initial pressure drop as a function of radius to minimize the generation of higher order harmonics. With more effort, satisfactory results may be obtained for both the n=3.5 and n=4.0 polytropic states. For the purposes of this analysis, however, it was not necessary to make this effort. As the PNS would ultimately be modeled with a polytropic index of n=2/3, it was more important to see how the simulation performed with smaller values of n.

Table 3.1 shows the fundamental oscillation frequencies obtained with the computer simulation for each value of n versus the oscillation frequencies predicted analytically by

Cox. As can be seen, the computer simulation agrees very well with the analytical predictions for the n=1.0 through n=3.0 polytropes, which gives confidence that the simulation would provide accurate results for the n=2/3 polytrope.

Table 3.1 – Comparison of fundamental oscillation frequencies of a star obtained by analytical and numerical methods for six different polytropic states. Dimensionless units were calculated using $\omega^2 R^3/(GM)$. Frequencies were calculated for the PNS using M=1.2M_0 and R=20 km. While the adiabatic gamma was 5/3 here rather than 2.5 for the PNS, these values still provide an order of magnitude for an actual PNS. Given the numerical resolution of 2 significant figures, no statistical difference between the analytical and numerical results was found.

Polytropic Index (n)	Dimensionless Star Frequencies		Star Frequencies (rad/sec)
	Analytical[1]	Numerical	
1.0	1.892	1.9	8 k
1.5	2.712	2.7	10 k
2.0	4.00	4.0	20 k
3.0	9.261	9.3	40 k
3.5	12.69	13	60 k
4.0	15.38	no oscillations	70 k

We can find an approximate value for the n=2/3 polytrope (for the real supernova problem) by extrapolating the data. Fitting the average of the analytical and numerical data with a 2nd order polytropic equation, we find that the star oscillates at about 6k rad/sec. Keep in mind though that this is using an adiabatic gamma of 5/3. The actual PNS, which is modeled with a gamma of 2.5, is much stiffer and the frequency will be higher. In chapter 5, the PNS fundamental frequency will be found experimentally to be about 12k rad/sec.

3.4 PNS Surface Velocity

Using the oscillation frequency of the PNS and an assumption of available energy, the surface velocity of the PNS can be determined. Cox provides the basis for this calculation with an equation for the kinetic energy of a polytropic star due to purely radial oscillations [Cox 1980]:

$$\mathrm{T} = \int_M \tfrac{1}{2}\left\{\frac{\partial}{\partial t}\left[\mathrm{Re}\left(\zeta(r,t)\right)\right]\right\}^2 r^2\, dm\,, \tag{3.1}$$

where ζ is the displacement function of the surface of the star, defined by

$$\zeta(r,t) \equiv \frac{\delta r}{R}, \tag{3.2}$$

δr is the displacement, R is the nominal star radius and the integral is over mass. We can rewrite the displacement function with an amplitude and a sine function:

$$\zeta(r,t) = \left|\xi(r)\right| \sin(\omega t). \tag{3.3}$$

Substituting (3.3) into (3.1) and averaging the energy over one period, the average kinetic energy is

$$\overline{\mathrm{T}} = \tfrac{1}{4}\omega^2 \left|\xi(r)\right|^2 \int_M r^2\, dm\,, \tag{3.4}$$

and combining equations (3.2) and (3.3) yields

$$\frac{\delta r}{R} = \left|\xi(r)\right| \sin(\omega t)$$

or

$$\delta r = R\left|\xi(r)\right| \sin(\omega t). \tag{3.5}$$

Recognizing that velocity,u, is $\partial/\partial t(\delta r)$ and using equation (3.5) we can write velocity as

$$u = R\omega|\xi(r)|\cos(\omega t)$$

or

$$u^2 = R^2(\omega|\xi(r)|)^2\cos^2(\omega t).$$

The peak velocity is then

$$u_0^2 = R^2(\omega|\xi(r)|)^2. \tag{3.6}$$

Solving (3.6) for the displacement amplitude, ξ, and substituting this into equation (3.4), we obtain

$$\overline{T} = \tfrac{1}{4}\frac{u_0^2}{R^2}\int_M r^2 dm. \tag{3.7}$$

This equation relates the kinetic energy to the surface velocity, which is what we are looking for. The equation can be written in a slightly more useful form by multiplying by M/∫dm (where *M* in this case is mass, not Mach number), so that it becomes

$$\overline{T} = \tfrac{1}{4}u_0^2 M\frac{\int_M r^2 dm}{R^2\int dm},$$

and the fraction on the end is a dimensionless term that depends only on the Polytrope being used. This term was calculated numerically for the n=2/3 Polytrope to be 0.36, so the equation can be rewritten specifically for the n=2/3 Polytrope as

$$\overline{T} = \tfrac{1}{4}u_0^2 M\,0.36. \tag{3.8}$$

As previously discussed, it is generally assumed that there is 1e51 ergs or 1e44 Joules of energy available to explode the star when the stellar core collapses. Assuming, for the sake of argument, that all of this energy is stored in the oscillations of the PNS, we can plug

this value and the mass of the PNS (which we have been assuming is $1.2M_0$) into equation (3.8), and we find that the maximum surface velocity for the PNS is about 2e7 m/s (assuming that all of the available energy is in the kinetic energy of the PNS, and the PNS oscillates with a fundamental radial mode). This result will be put to use in Chapter 4.

Chapter 4 – Idealized Atmospheric Test Cases

4.1 General

Observations in two and three dimensional hydrodynamic simulations show acoustic waves with interesting behavior. As an example, in their simulations Burrows *et al*. claimed that the accretion shock restart was assisted by accoustic waves propagating away from the PNS, steepening into shocks well below the sound speed of the medium and dissipating a significant amount of energy [Burrows 2007]. But this is not a classical shock wave formed by supersonic motion. One then has to wonder if shocks will really form in the post-shock atmosphere, and if so, if enough energy can be dissipated to help the explosion.

Fully understanding the behavior of acoustic waves in the post-shock atmosphere is challenging because of the non-uniform interdependent conditions to consider. In the hydrodynamic model, some of the conditions to consider are:

- Density falls off as $1/r^3$, which causes the amplitude of the velocity wave to increase as there is less mass to push for the same amount of momentum in the wave.
- Sound speed falls off as $1/r^{½}$, which causes shortening of wavelengths and steepening of wave fronts as the back end of waves catch up with the front.
- The spherical nature of the system means that the energy density of outwardly propagating acoustic waves decreases as the surface area increases with radius. This effect is pronounced at the small radii of our system. Case in point, as acoustic waves travel from a radius of 20 km to 200 km, the surface area increases by 100 fold and the energy density therefore drops by a factor of 100 (based on the equation for energy

density of a plane wave given by Lighthill [2005]: $E = \frac{1}{2} \rho_0 u_0^2$, where ρ_0 is the background density and u_0 is the velocity amplitude).

- The self gravity of the atmosphere can be significant as the atmosphere accounts for as much as 10% of the mass of the system. This not only changes the radial dependence of the gravitational force, but may also affects its direction when there is significant motion of the atmosphere, which is predicted by the SASI.

To determine how acoustic waves behave in the post-shock atmosphere, I used four idealized test cases to break down the complexities of the environment. Each idealized test case was designed to isolate the effect of one or two conditions of the post-shock atmosphere. Following is a brief description of each test case.

Case 1: Uniform atmosphere, without gravity or variations in the background pressure, density or sound speed. Used to study plane waves without any complicating factors. In this case, wave steepening and energy dissipation and numerical issues were focused on.

Case 2: Isothermal atmosphere, where the sound speed and gravitational force are constant in space and the background density of the atmosphere decreases exponentially with distance. Used to study the growth in wave amplitude associated with a decreasing density in isolation.

Case 3: Atmosphere, where the sound speed decreased as $1/x^{\frac{1}{2}}$, as it does in the real supernova problem. Used to study wave steepening and decreasing wavelength and their effects on energy dissipation. This decreasing sound speed was created by

increasing the density while keeping the pressure constant so that gravity could be left out, simplifying the problem.

Case 4: Realistic atmosphere, which was used to quantify energy dissipation in the full supernova problem. In this case, spherical waves were driven through an atmosphere of realistically varying density and pressure (and therefore sound speed), and the gravitational force varied as $1/r^2$, which approximated the real problem.

In each test case, acoustic waves were driven through the atmosphere at various frequencies and amplitudes to test wave properties, energy dissipation and numerical issues. Each model was analyzed analytically with linear analysis and numerically with computer simulations. Using linear analysis, the dispersion relation for each test case was derived, which provided valuable insight into the dependence of wave properties on distance and frequency.

Linear Regime

At very subsonic velocities, waves remain linear and do not dissipate a significant amount of energy. This is defined as the linear regime. Any energy dissipation measured in the numerical simulations in the linear regime would then be due to numerical error.

To be considered in the linear regime, perturbed velocities must be much smaller than the sound speed of the medium; but how small? A reasonable breakpoint between the linear and nonlinear regimes turned out to be around Mach .01 (later, it will be shown that the sound speed of the post-shock atmosphere ranges from about 2e7 m/s near the accretion

shock to about 5e7 m/s near the PNS). As will be shown, there was no statistically significant energy dissipated below Mach .01, so that acoustic waves at this level (in a Γ = 4/3 atmosphere) could be considered completely linear, and any energy dissipation measured could be attributed to numerical error. With this in mind, simulations will be run in each test case well below this Mach value as a way to gauge numerical error.

Non-linear Regime

At larger perturbed velocities, waves quickly become non-linear and only numerical analysis can be used. This is the regime where energy is dissipated and is of primary importance to this study. What upper limit should then be considered for testing? To determine this, we can consider several limiting factors: The surface velocity of the PNS; the escape velocity of the system; and severe bulk motion caused by large perturbations.

The maximum surface velocity of the PNS was estimated in the last chapter to be about 2e7 m/s. Near the surface of the PNS, the sound speed of the post-shock atmosphere is about 5e7 m/s, so the PNS surface is moving at about Mach 0.4. On the one hand, this is a conservative estimate because it assumes all of the available energy is in the PNS oscillations. On the other hand, it assumes 1st order radial oscillations only. While higher order harmonics tend to die out more quickly, non-radial modes are a possibility, which have higher frequencies.

The escape velocity for gas around the PNS can be calculated by setting the potential energy equal to the kinetic energy and obtaining

$$u_{esc} = \sqrt{\frac{2GM}{r}} .$$

At the accretion shock radius (around 200 km), the escape velocity is about 4e7 m/s or Mach 2, and at the surface of the PNS (around 20 km), the escape velocity is about 13e7 m/s or Mach 2.5. The amplitude of velocity perturbations must certainly be below these values.

Another limiting factor is bulk motion that will be discussed when reviewing the simulations for the atmospheric tests. In these tests, it was found that above about Mach 0.2, much of the atmosphere is forced out with the initial sound wave quickly reducing the mass density to a small fraction of the original value and changing the properties of the atmosphere (refer to Figure 4.5 for an example of this dropping mass density). Limited acoustic analysis needs to be done in this regime, because the dynamics of system become dominated by this bulk motion. While Mach 0.2 was found to be a reasonable cut-off point, the cause of this bulk motion is not well understood and some latitude should be given to this cut-off point.

The escape velocity at the accretion shock gives a firm ceiling of Mach 2. The other two criteria, Mach .4 for PNS surface velocity and Mach .2 for bulk motion, are not as firm. At times, bulk motion limited the ability to gather reasonable data above Mach .2, but in many cases, energy dissipation analysis could be performed up to Mach 1.0, as long as mass loss was not much greater than 50%.

Each idealized model was set up in one dimension with a Γ=4/3 atmosphere (except for the isothermal case where gamma by definition had to be 1.0). In the numerical simulations, an oscillating wall was placed at the inner or left boundary, and oscillations were

simulated by forcing the local velocity of the atmosphere next to the boundary to oscillate sinusoidally. The opposite boundary was configured to allow waves to propagate off the grid with minimal reflection, simulating an infinite atmosphere. The first three models used Cartesian coordinates, and the fourth model used spherical coordinates.

When gravity was included in the idealized atmospheric models, the self gravity of the atmosphere was ignored. In the second model, the gravitational force was constant in space (pointing to the left), and in the fourth model, the gravitational force varied as $1/r^2$ and was calculated as if the PNS (the source of the gravitational force) were located entirely behind the oscillating boundary. These approximations simplified the analysis and allowed the results to be calculated analytically. In the full problem, self gravity is a significant factor as the ratio of the PNS mass to the atmosphere mass is dynamic but is generally around 9:1 (this is calculated in section 4.5). The full model discussed in the next chapter includes the self gravity of the atmosphere.

This chapter is separated into four sections, one for each idealized atmospheric model. Each section describes the model, the analytical and numerical results, and any numerical issues.

4.2 Test Case 1 – Uniform Atmosphere

4.2.1 Description

The goal of the first idealized atmospheric model was to learn the most basic issues about sound wave behavior in the post-shock atmosphere, considering just the nature of the relativistic electron gas (modeled with an adiabatic exponent of $\Gamma=4/3$). To keep the situation as simple as possible, gravity was excluded from the model and background values of pressure and density were set up uniformly, i.e. without any spatial variance. This meant that the sound speed of the medium was also uniform. Plane waves were propagated through this uniform atmosphere with various amplitudes ranging from very subsonic to supersonic, and their behavior was observed. Of key interest was how different amplitudes affected the non-linear behavior and dissipation of these acoustic waves as they propagated. Basic numerical issues and limitations associated with computer modeling in these conditions were also studied. By using this idealized model with a uniform background and no gravity, the effects of a spatially varying density, varying sound speed, spherical geometry, etc. were eliminated, and I was able to focus solely on how the amplitude of the perturbed velocity affected the behavior of acoustic waves in a $\Gamma=4/3$ gas. The effects of these complicating conditions will be discussed in subsequent sections that cover the other idealized models.

4.2.2 Linear Analytical Analysis

The linear wave equation in this case was derived using Euler's equations for momentum and energy, and following the prescription in Section 2.2. The momentum and energy equations in 1D Cartesian coordinates are:

$$(\rho u)_t + (\rho u^2)_x + p_x = -\rho g \tag{4.1}$$

$$(\rho E)_t + (\rho u E)_x + (up)_x = 0\,, \tag{4.2}$$

and the resultant wave equation is:

$$u'_{tt} - c_s^2 u'_{xx} = 0\,, \tag{4.3}$$

where the sound speed in *this* case is constant in time and space and is defined as:

$$c_s^2 = \Gamma \frac{p_c}{\rho_c}\,. \tag{4.4}$$

Using the separation of variables technique, also discussed in section 2.2, the equation for the velocity wave is found to be

$$u' = u_0 \cos(\omega t \pm kx)\,, \tag{4.5}$$

where u_0 is the velocity amplitude of the perturbation, ω is the driving frequency and k is the wave number ($k=\omega/c_s$).

The velocity wave is perfectly sinusoidal, with a constant amplitude and a length scale that depends only on the driving frequency and the sound speed. This result is exactly as one would expect, given the uniform conditions and assumption of linearity. The spatial dependence of amplitude and wavelength will become important as we look at non-uniform background conditions in subsequent idealized cases.

4.2.3 Numerical Analysis

Numerical analysis was performed in both linear and nonlinear regimes. As previously explained, acoustic waves of any amplitude will eventually steepen into shocks, but for the case where $u_0 << c_s$, this steepening takes place on a much larger distance scale than the size of the supernova post shock region. Simulations with such small amplitudes will have no statistically significant steepening or energy dissipation and will be used for numerical error analysis. Waves with larger amplitudes are no longer considered linear and must be evaluated with numerical simulations.

In the numerical simulations for the uniform atmosphere, the background pressure and density were set to p_e = 4e27 N/m^2 and ρ_e = 1e13 kg/m^3 (which are typical values at a radius of 100 km in the supernova post-shock atmosphere) and the adiabatic exponent, Γ, was set to 4/3. The sound speed, given by equation (2.22), evaluates to 2.3e7 m/s.

Numerical Issues – Peak Shaving

In the linear regime, sound waves should remain sinusoidal indefinitely. Using a Mach value of .0009, simulations were run and the results were compared to the sinusoidal wave predicted by linear analysis in equation (4.5). As can be seen in Figure 4.1, for a spatial resolution of 91 zones/wavelength, there was very little deviation. The only significant difference was in the peak values where the numerical result was "shaved". A blow-up of the circled region is shown in Figure 4.2. This peak shaving is caused by monotonicity constraints in the hydro code, which is used to help maintain numerical stability [Colella & Woodward 1984].

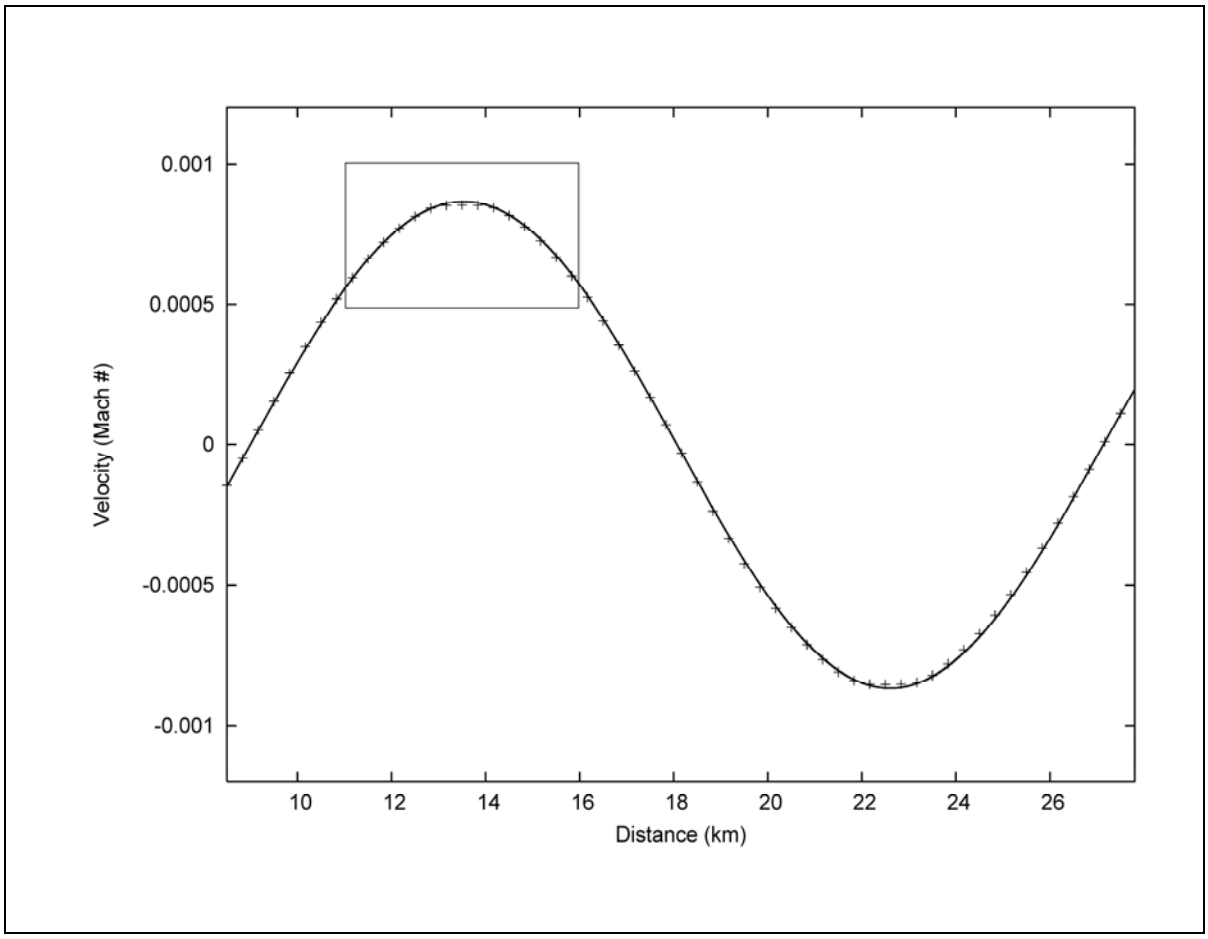

Figure 4.1 - Comparison of analytical and numerical perturbed velocity curves, using 54 zones per wavelength for the numerical simulation. The solid line is the analytical solution, which is a sine wave, and the numerical results are represented by + symbols. A blow-up of the boxed-in area is shown in the next Figure 4.2.

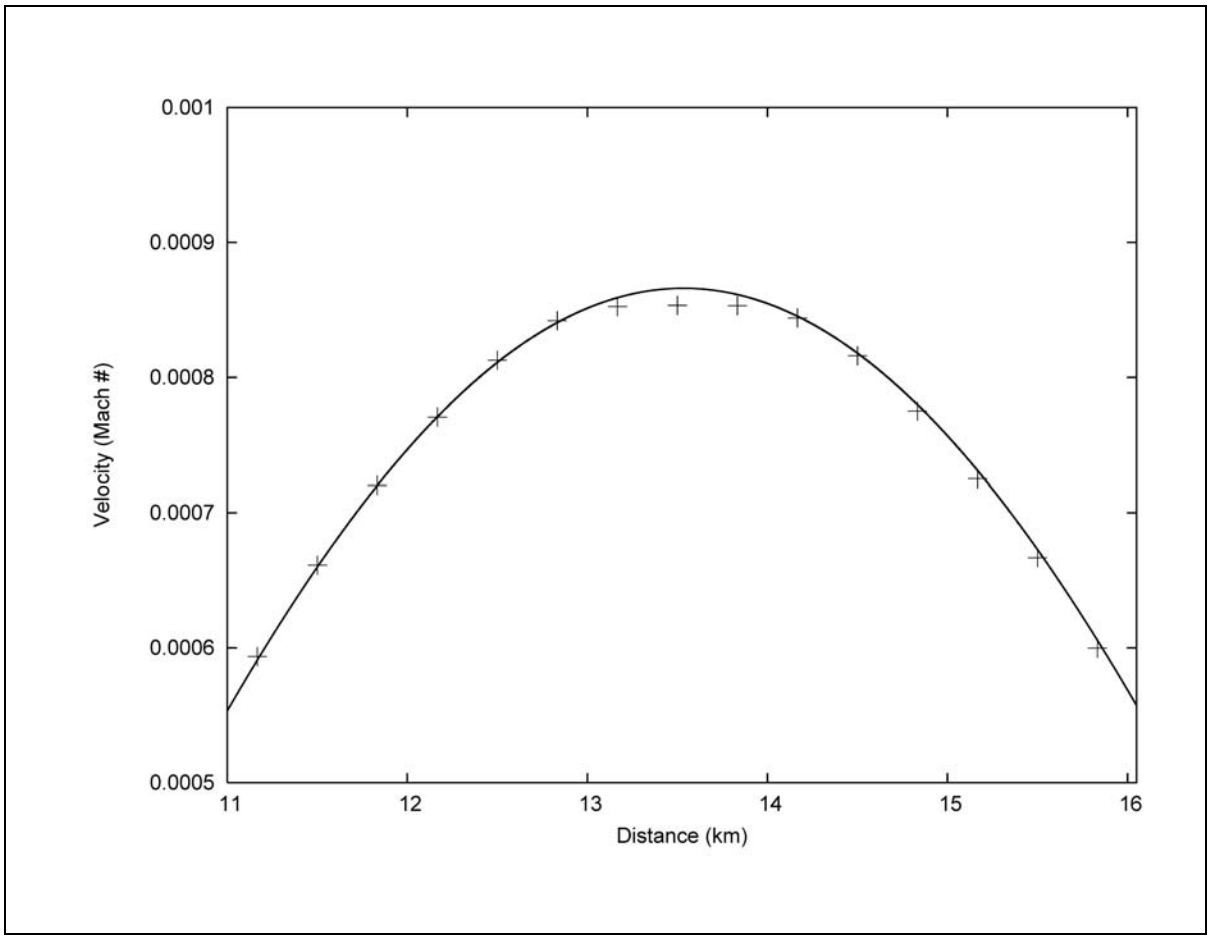

Figure 4.2 - Blow-up of the boxed-in area shown in Figure 4.1.

Figure 4.3 plots the peak shaving error as a function of resolution. This is plotted on a log-log plot to determine the order of convergence, which is defined as the negative of the slope. As shown in the Figure, the order of convergence was 1.5. While it is interesting to note this discrepancy and convergence, the real question is how this error affects measurements of energy dissipation. This issue will be discussed shortly.

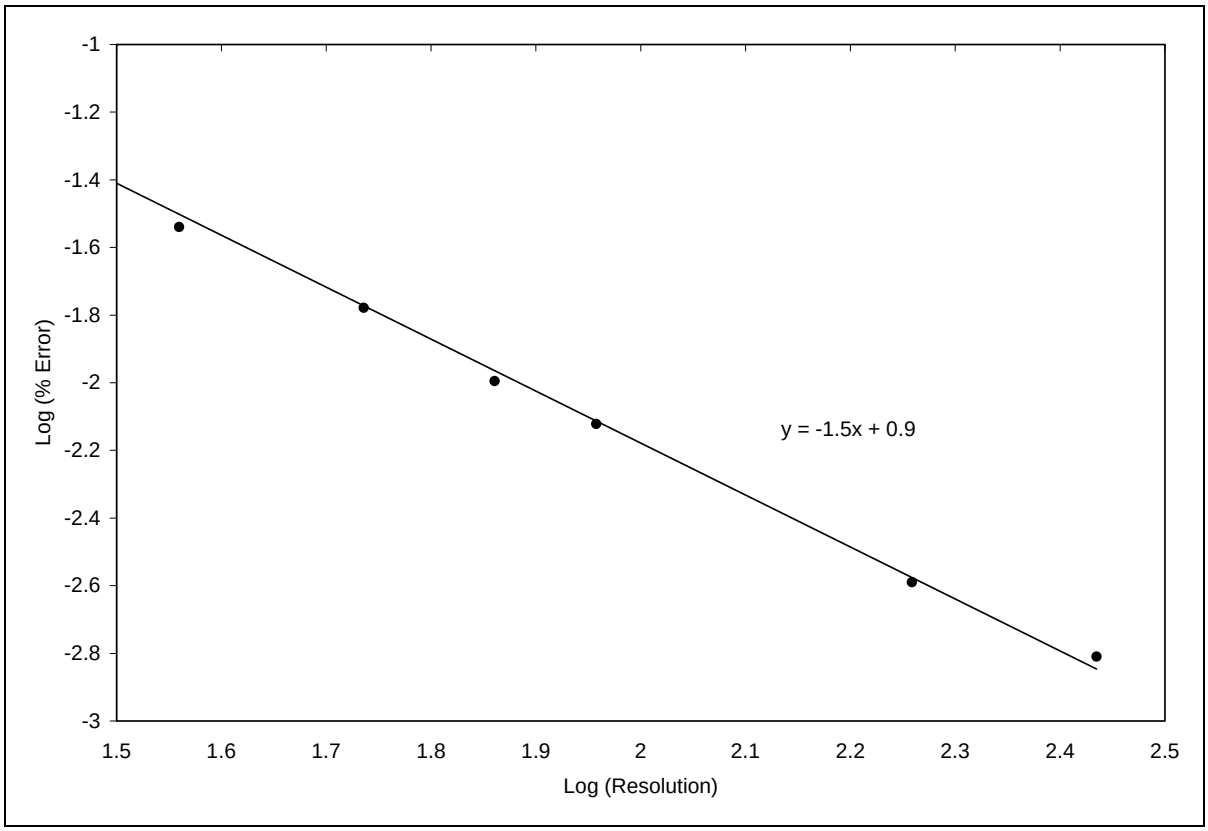

Figure 4.3 - Order of convergence of peak velocity. The order of convergence is the negative of the slope of the log-log plot of error versus resolution.

Numerical Issues – Sound Speed

As long as the background conditions do not change, the sound speed, or phase velocity, measured in the numerical simulations should agree with the sound speed defined by equation (4.4) in the analytical analysis. The sound speed in the numerical simulation was determined by measuring wavelength and using the basic wave relationship

$$c_s = \frac{\lambda\omega}{2\pi},$$

where ω is driving frequency of the system and λ is the wavelength. The wavelength in the numerical simulation was calculated from zero crossings of the velocity wave.

The computer simulation was run with a resolution of approximately 91 zones/wavelength and three different values of gamma. $\Gamma = 4/3$ was used as it is the adiabatic exponent for the post-shock atmosphere. I also used $\Gamma = 5/2$ as this is the adiabatic exponent for the PNS, and $\Gamma = 5/3$ as this was the adiabatic exponent used in chapter 4 for the PNS pulsation frequency analysis. The results, shown in Table 4.1, demonstrate a strong agreement between the linear analysis and the numerical results.

Table 4.1 - Comparison of the sound speed obtained by linear analysis and numerical simulations.

Adiabatic Exponent (Γ)	Sound Speed (m/s)		
	Linear Analysis	Numerical Simulation	% Error
4/3	2.30940E+07	2.30936E+07	-0.0018%
5/3	2.58199E+07	2.58192E+07	-0.0027%
5/2	3.16228E+07	3.16224E+07	-0.0012%

Numerical Issues – Energy Measurement

Computer simulations were run at Mach .0009, which is well into the linear regime, so any measurements of energy dissipation would be due to numerical error. To put this to the test, I used an extremely high 2721 zones/wavelength for about 0.14 s. The fractional dissipation rate ranged from 3.2e-10 to -8e-11 per second, with an average value of 1e-10 per second. Assuming a normal distribution, the uncertainty of this measurement is 4e-10 per second (for a 3σ or 99.7% confidence level). The bottom line being that within a 99%

confidence level, the actually fractional rate of energy dissipation is between zero and 6e-10 per second.

So how does the simulation do at more practical spatial resolutions? Assuming that there is zero energy dissipated at this low Mach value, which we can now say is a valid assumption to within an uncertainty of 6e-10 (fraction per second, in a typical time-scale of 1 second for the post-bounce period), any energy dissipation measured is due to numerical error. A log-log plot of this energy dissipation error as a function of resolution is shown in Figure 4.4. The data point circled in the figure corresponds to a resolution of 54 zones/wavelength, which we will later see is a moderate resolution to use in these types of simulations. The simulation at this resolution provided an error in the energy dissipation measurement of 8e-8 (fraction/sec). The order of convergence for energy, which is the negative of the slope of the line in this plot, was 2.3.

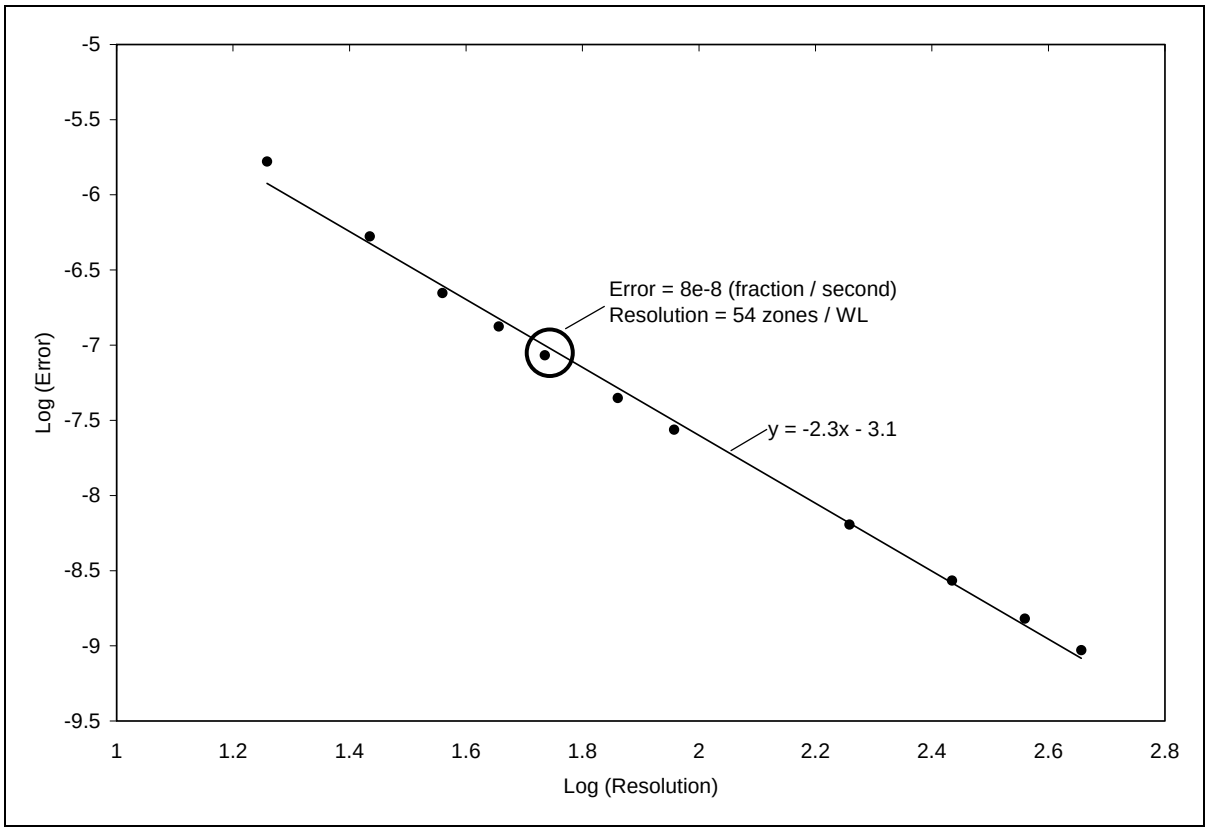

Figure 4.4 - Error plot of energy dissipation as a function of spatial resolution. The order of convergence is the negative of the slope of the log-log plot or 2.3. The energy dissipation (measured by monitoring S) was averaged over the simulation volume and over 10 periods to help smooth out noise and numerical sampling issues.

Bulk Motion

It was also observed that once acoustic waves were generated, the entire atmosphere migrated toward the outer boundary. In the uniform atmosphere, this bulk motion was only significant for perturbations above about Mach 0.1. Above Mach 0.1, this bulk motion caused a significant reduction in mass density, and above Mach 0.3 the background sound speed of the atmosphere noticeably increased, as evidence by an increased wavelength.

The reduction in mass density over time in the volume is shown in Figure 4.5. At Mach 0.4, the density drops a few hundredths in the first 20 ms (left edge of plot). Below

Mach 0.3, the density drops more gradually and the background properties were not significantly changed. The lowest two Mach values are flat in the plot though there is actually a slowly decreasing density in both cases that does not show up at this scale.

The effect of bulk motion on acoustic waves will be discussed further as the other test cases are reviewed.

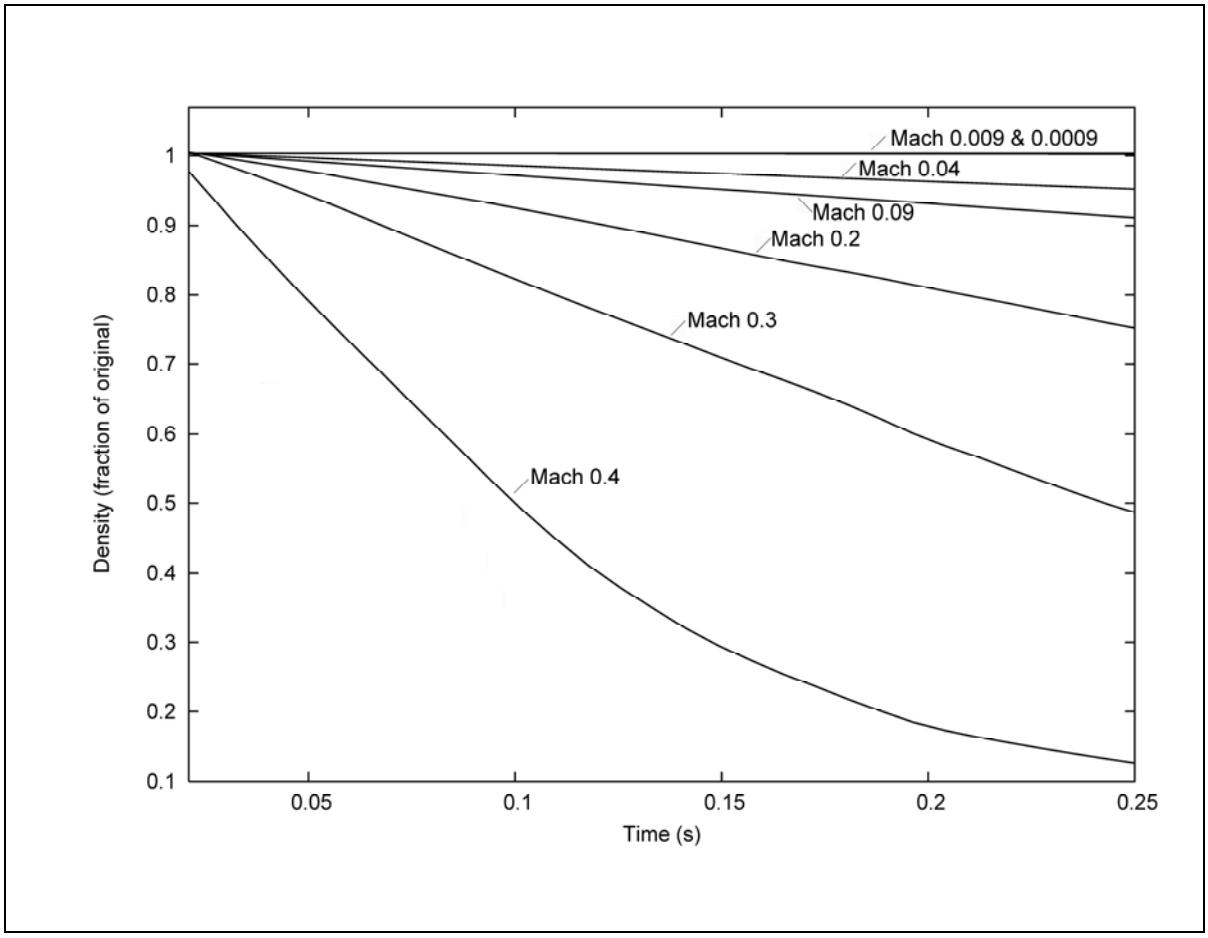

Figure 4.5 - Average density in the volume as a function of time for several Mach values. The density for the lowest Mach values do not change much.

Shockwave Formation

As previously indicated and observed in testing, no significant amount of energy is dissipated in the linear regime. Therefore, to study energy dissipation, tests must be performed in the non-linear regime, above Mach .01. In this regime, we see acoustic waves steepen and develop into shocks, at which point their amplitude begins to decay and energy is dissipated. This effect can clearly be seen in the Mach .04 simulations shown in Figure 4.6. To confirm that this amplitude decay is real and not a numerical artifact such as peak shaving, two simulations were run, one at a modest resolution of 51 zones/wavelength and the other at a very high resolution of 6,800 zones/wavelength. The results of these simulations are shown in Figure 4.6.

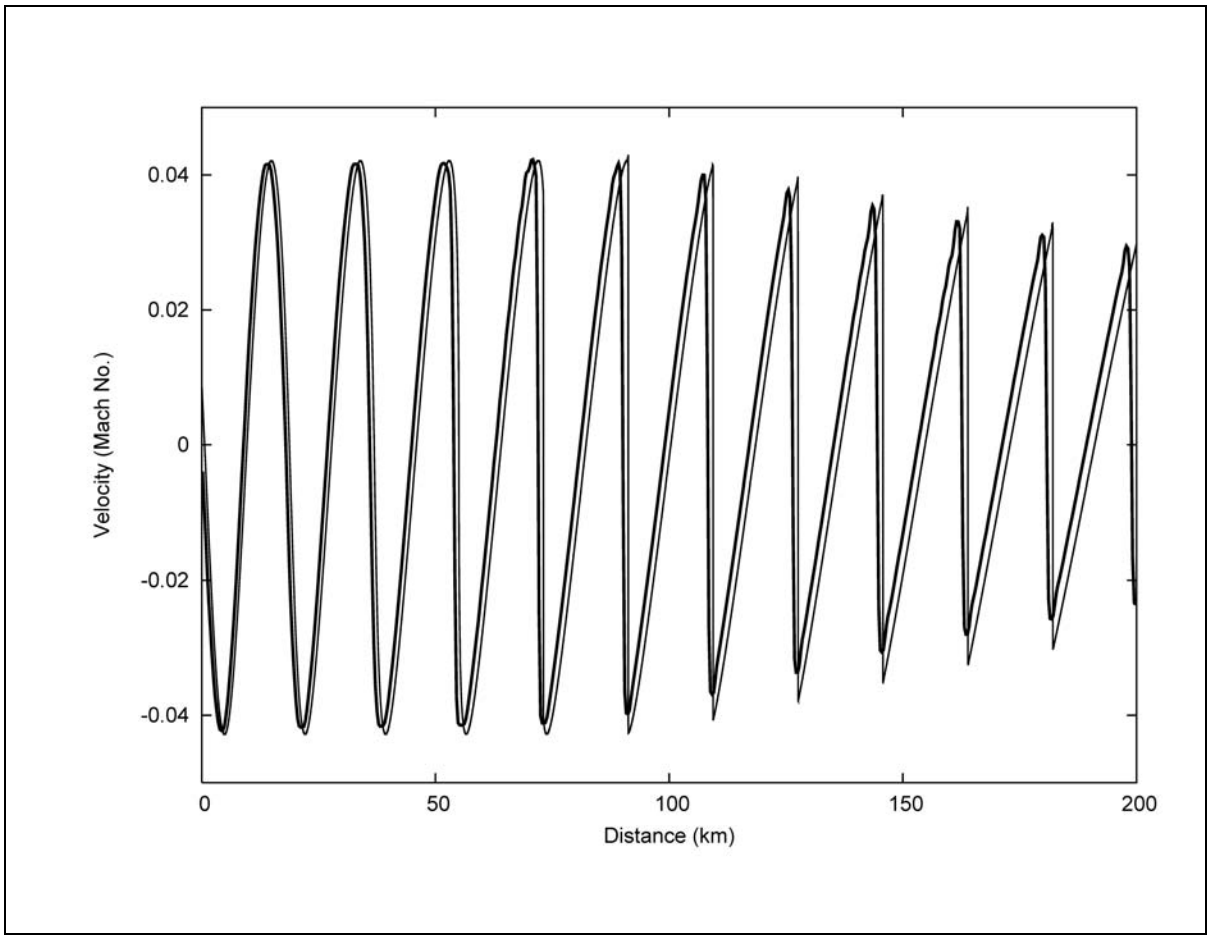

Figure 4.6 - Comparison of amplitude decay for 54 and 6,800 zones/cycle at Mach .04. The lower resolution waveform is the dark bold line, and the higher resolution waveform is the thin line. The phase of one velocity wave was intentionally shifted slightly so that the two waves could be seen on the same plot. This image shows velocity waves at a moment in time. In the full simulation, the waves propagate to the right such that the value at the left boundary would oscillate between (approximately) Mach -.04 and +.04.

While there was some difference in amplitude between the two simulations as a result of the peak shaving discussed earlier, the amplitude decay of both waves is much larger than this difference. There also appears to be little difference in the progression of wave steepening between the two simulations. This leads one to conclude that the steepening and amplitude reduction are in general real effects as described by Shu [1992] and discussed in

detail in Section 2.3. According to that analysis, the point where the amplitude begins to decay is the point where a wave develops into a full shock, and the distance to that point (for the case of a uniform atmosphere) is predicted by equation (2.43). In Figure 4.7, the velocity curves for a Mach .04 and a Mach .1 simulations are shown along with the predicted point where shocks form. By extending dashed lines over wave peaks, this point can also be found for the numerical simulation. As can be seen, there is little difference between the predicted and numerical points, again supporting Shu's description of wave steepening and shock formation.

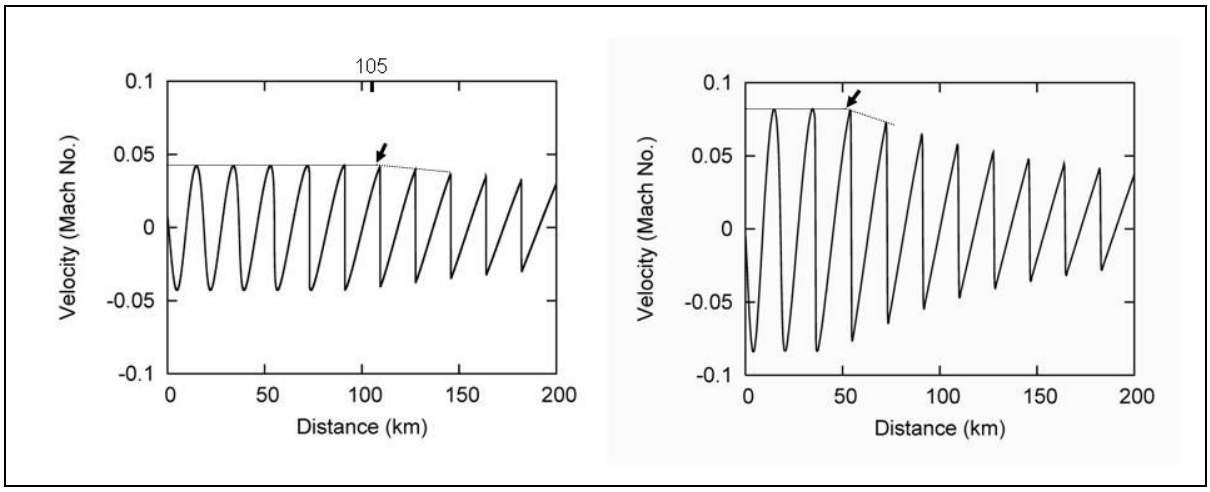

Figure 4.7 - Amplitude decay for Mach .04 and Mach .1 simulations (more precisely Mach .0433 and Mach .0866). The dashed lines are used to extrapolate wave peaks and determine the point where amplitude decay begins. This point is denoted by the arrow in each plot. The point that amplitude decay was predicted to begin by equation (2.43) was 105 km for the first plot and 52 km for the second plot.

Energy Dissipation

As indicated in Section 2.4, the fractional rate of change of internal energy due to wave dissipation can be represented by the fractional rate of change of S: $\Delta S/(S\,\Delta t)$, where S comes from the equation of state and is a function of entropy. This value is plotted as a

function of position for a Mach .04 simulation in Figure 4.8 along with the velocity wave from the numerical simulation and the velocity wave predicted by linear analysis, equation (4.5). As long as there was not a significant amount of bulk motion, the energy dissipation profile shown in this figure was very steady (i.e. the rate of energy dissipation did not increase or decrease over time). The only noticeable changes over time were associated with noise in the curve.

As can be seen in the figure, there was essentially no energy dissipation until the shock front clearly formed. From that point, the dissipation rate decreased as the velocity wave amplitude decreased. This correlation between the energy dissipation rate and wave amplitude was repeated in all of the atmospheric models that will be discussed in subsequent sections.

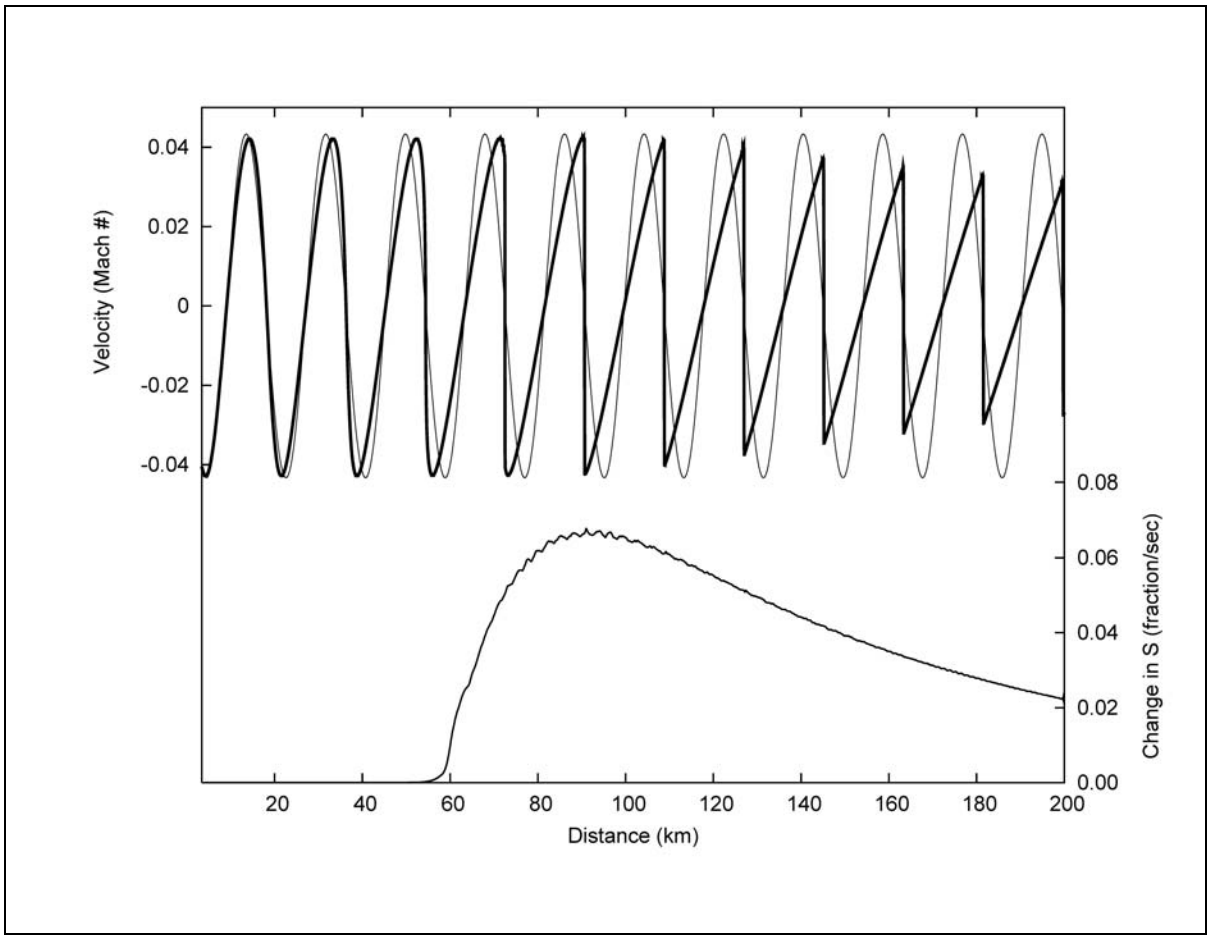

Figure 4.8 - Velocity waves from a Mach .04 perturbation shown for both a numerical simulation (dark line) and the linear analytical analysis (light line). The fractional rate of change of entropy is also shown. Aside from some noise, the rate of change in entropy remained steady during the simulation. The numerical simulation was run with a resolution of 56 zones per wavelength.

For larger perturbations, the average energy dissipation rate was predictably higher and waves developed into full shocks closer to the oscillating boundary as the velocity amplitude was larger. In addition, when the perturbations were large enough, some energy was dissipated near the oscillating boundary. This dissipation near the oscillating boundary seemed to be related to mass being forced away from the oscillating boundary and is probably a separate phenomenon from dissipation due to shock formation. We will see in

later test models that this dissipation at the boundary is more pronounced in some models than in others and may be tied to the background density profile. It does not appear to be a numerical artifact of the oscillating boundary, as it was also seen in the full coupled model where acoustic waves were driven by a pulsating PNS. Both energy dissipation effects can be seen in the Mach 0.2 plots shown in Figure 4.9.

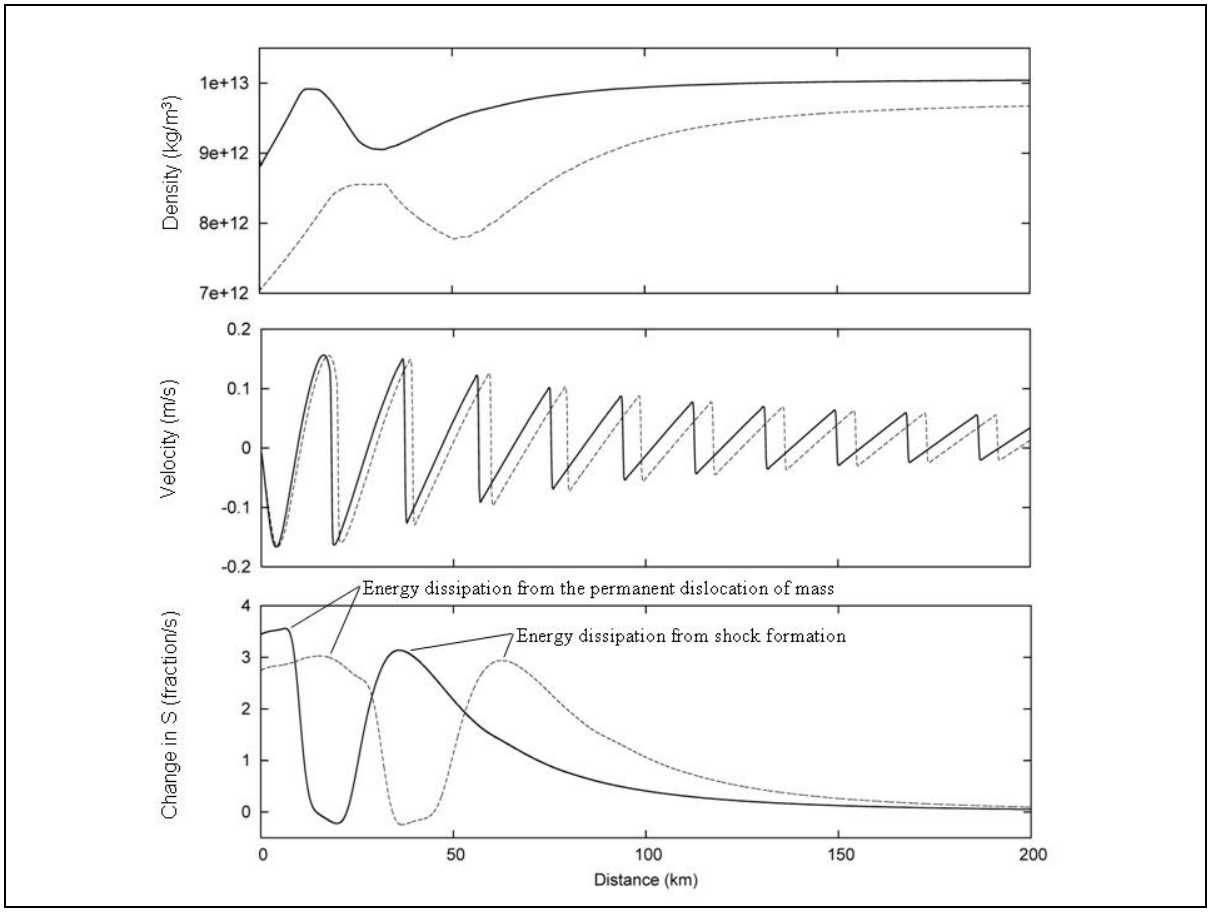

Figure 4.9 - Density, velocity and change in S are shown for a simulation with initial Mach value of 0.2. Data is shown for t = .05s (solid line) and t = .1s (dashed line).

When the perturbations were large enough to cause a significant amount of bulk motion (greater than Mach 0.1 per previous discussion), the rate of energy dissipation varied over time. Figure 4.10 shows this variation for several Mach values by plotting the average dissipation rate in the volume versus time. Above Mach .04, there was a characteristic initial rise in the fractional rate of change of entropy followed by a slow decline. This fluctuation was caused by shocks that would form and then spread out as mass advected out of the volume and the atmospheric properties changed. In contrast, at Mach .04 and below, the atmospheric properties remained relatively constant, so the energy dissipation rate also remained relatively constant. The peak values from Figure 4.10 are plotted in Figure 4.11 as a function of Mach number. It clearly shows the increasing dissipation rate at higher Mach values.

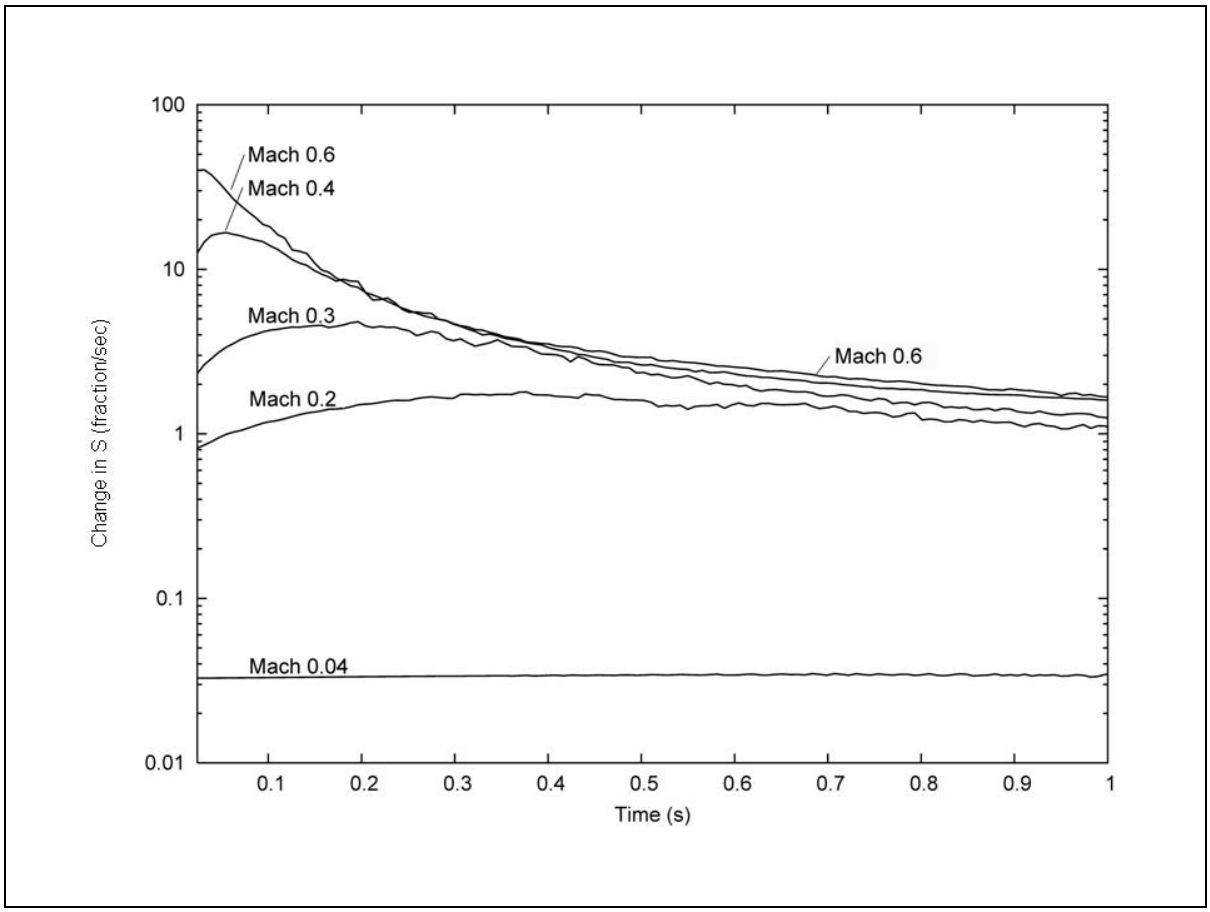

Figure 4.10 - Fractional rate of change of the average S in the volume for five different Mach values. The results for lower Mach values are essentially the same as the Mach .04 results in this plot.

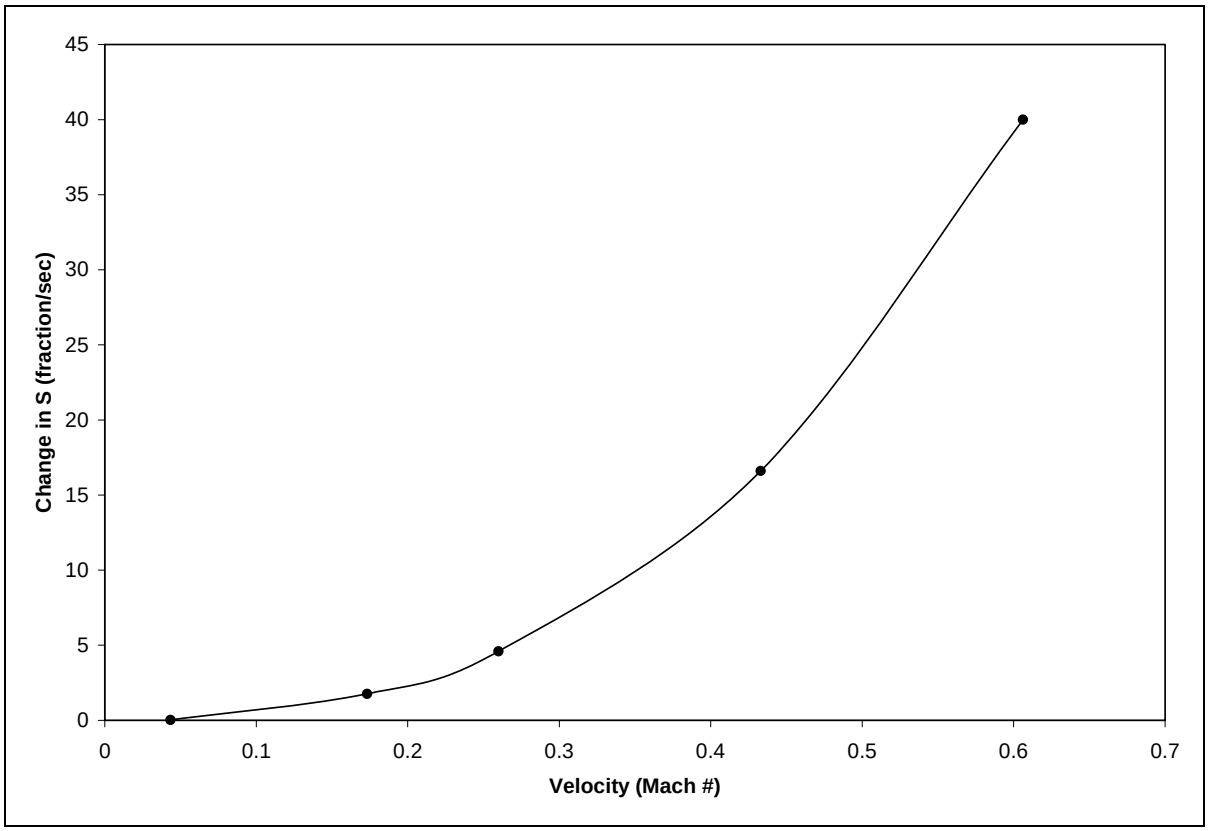

Figure 4.11 - Maximum change in *S* from Figure 4.10 plotted as a function of Mach number.

As wave energy is dissipated into the surrounding atmosphere, we would expect the temperature of the atmosphere to increase. Extending the analysis in Chapter 2 by integrating equation (2.48), we can use the relative value of *S* (which is proportional to temperature) for this purpose.

The relative temperature increase for the same simulations shown in Figure 4.10, can be seen in Figure 4.12. Interestingly, this increase is steady despite fluctuations in the energy dissipation profiles seen in Figure 4.10. By this view, we can clearly see how much the average atmospheric temperature has changed over time. As an example, after one second, the temperature for the Mach 0.6 simulation increased by 40 times its original value.

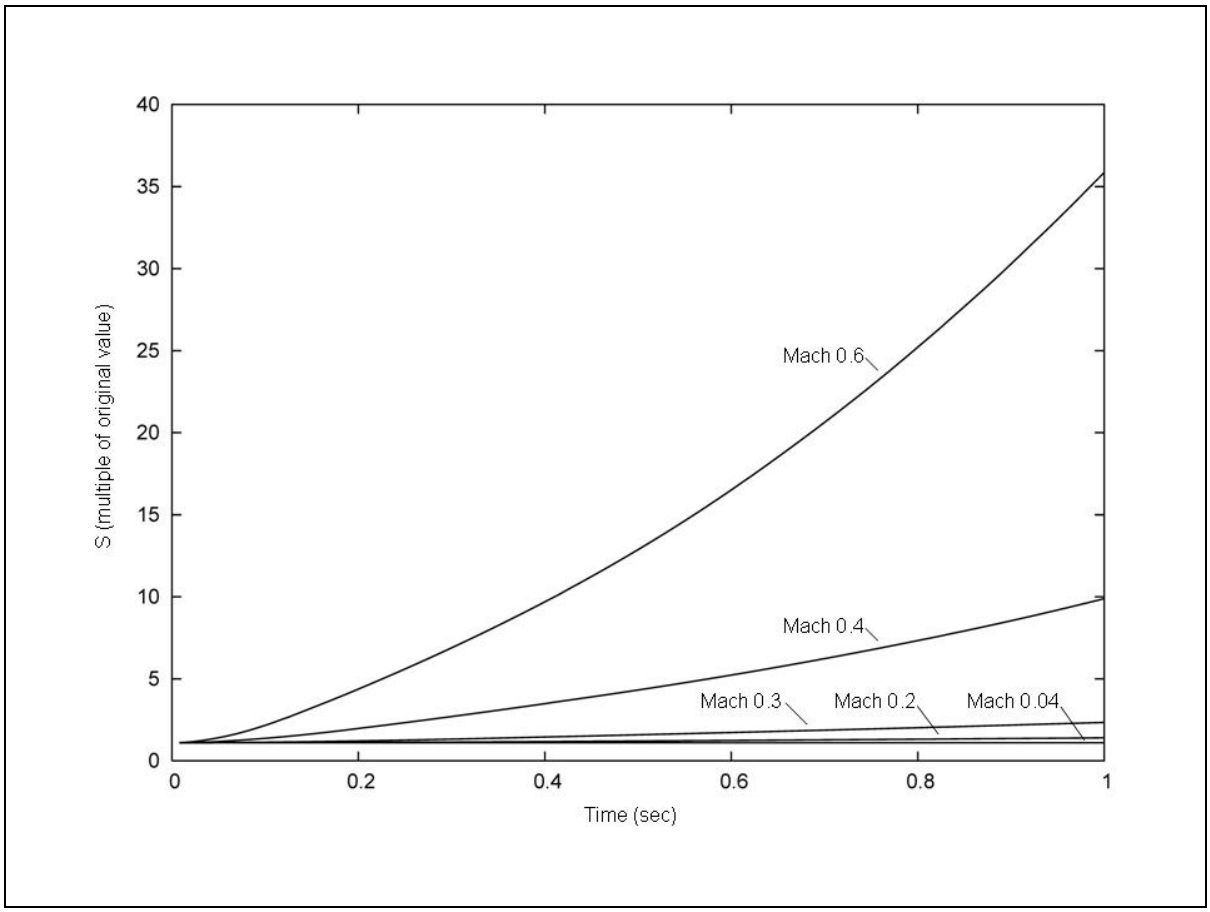

Figure 4.12 - *S*, averaged over the entire volume, is shown for several Mach values. *S* is used here as it is proportional to temperature.

By looking at the profile of *S* with distance, it is interesting to note that there is essentially no spreading of higher temperature regions within the 1 second time-scale of the stalled shock. As an example, Figure 4.13 shows the temperature profile at several time steps for a Mach .04 simulation. What we find is that the thermal energy essentially remains where it is deposited in the volume, which is reasonable given the steady state background conditions and the time scale that is much shorter than the diffusion rate of the thermal energy.

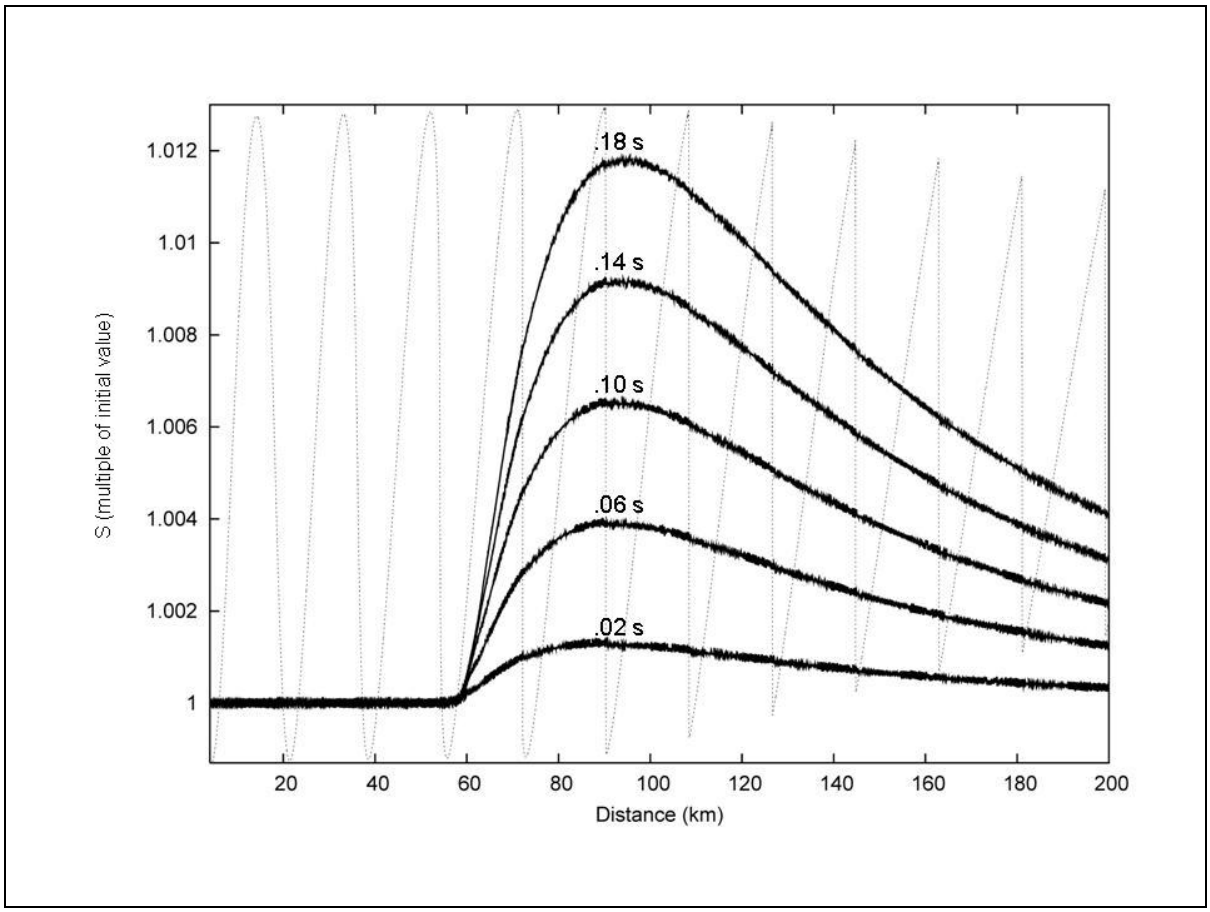

Figure 4.13 - Relative temperature profile in the volume (represented by *S*) for a Mach .04 simulation at .04 s time intervals. The light curve is the perturbed velocity wave shown for reference.

4.3 Test Case 2 – Isothermal EOS

4.3.1 Description

An isothermal equation of state was used to study sound waves in an atmosphere where the background density decreases with radius as it does in the real supernova problem. Sound speed and gravitational force were kept constant so that the effects of a varying background density could be studied without the effects of other complicating conditions.

For an ideal gas, an isothermal process requires that pressure and density be directly proportional (which can be seen from the ideal gas law, $pV = nRT$, where the right side of the equation is constant). Considering the polytropic equation of state, $p = S\rho^{\Gamma}$, this then requires that Γ be 1.0 and S be uniform throughout the atmosphere, which gives us the isothermal equation of state:

$$p = S\rho \tag{4.6}$$

From the definition of sound speed, equation (2.37), we can then recognize that the isothermal sound speed is simply $c_s = \sqrt{S}$ and is therefore constant in space.

Using the isothermal equation of state, we can also determine the background pressure and density profiles that must exist at equilibrium. Consider the Euler momentum equation, (2.6). At equilibrium, the time derivative term is zero and the velocity is also zero, so this equation becomes:

$$p_x = -\rho g\,, \tag{4.7}$$

which is known as the "equation of hydrostatic equilibrium". Taking the x-derivative of (4.6) and substituting the result into (4.7), we obtain:

$$S\rho_x = -\rho g\,, \tag{4.8}$$

which has the solution:

$$\rho_e = \rho_0 e^{-x/H}\,, \tag{4.9}$$

where: H is the scale height, S/g; the density is given a subscript e to indicate that it is the equilibrium (or unperturbed) value; and ρ_0 is the density at $t = 0$ and $x = 0$. The pressure has a similar solution:

$$P_e = S\rho_0 e^{\frac{-g}{S}x} \tag{4.10}$$

Because there is a pressure gradient, a gravitational force must be included in the system to balance it, but this gravitational force is constant in the model, which helps to avoid any complicating factors.

We have now fully specified the initial state of the system for both the numerical and analytical problems and can begin the analysis. In this analysis, plane waves were propagated through the hydrostatic atmosphere described by equations (4.9) and (4.10), using a 1D Cartesian scheme.

4.3.2 Linear Analytical Analysis

To derive the linear analytical result this time, we will start with the Euler's equations for continuity and momentum in 1D:

$$\rho_t + (\rho u)_x = 0 \tag{4.11}$$

$$(\rho u)_t + (\rho u^2)_x + p_x = -\rho g \tag{4.12}$$

From equation (4.6) and using the fact that S is constant in space, we can write

$$p_x = S\rho_x$$

Substituting this into equation (4.12), we obtain

$$(\rho u)_t + (\rho u^2)_x + S\rho_x = -\rho g \tag{4.13}$$

Linearizing equations (4.11) and (4.13) and dropping the small terms per the linearization discussion, we get:

$$\rho'_t + (\rho_e u')_x = 0 \tag{4.14}$$

$$\rho_e u'_t + S(\rho_e)_x + S\rho'_x = -g(\rho_e + \rho') \tag{4.15}$$

Now taking the spatial derivative of (4.14) and the time derivative of (4.15) and combine the results, we obtain

$$\frac{1}{S}\rho_e u'_{tt} - \frac{g}{S}(\rho_e)_x u' - \frac{g}{S}\rho_e u'_x - (\rho_e)_{xx} u' - 2(\rho_e)_x u'_x - \rho_e u'_{xx} = 0 \tag{4.16}$$

From equation (4.9), we can write:

$$(\rho_e)_x = -\frac{g}{S}\rho_e$$

and

$$(\rho_e)_{xx} = \left(\frac{g}{S}\right)\rho_e$$

Substituting these relationships into equation (4.16), we finally obtain the wave equation for the velocity:

$$\frac{1}{S}u'_{tt} + \frac{g}{S}u'_x - u'_{xx} = 0 \tag{4.17}$$

Using the separation of variables technique, we then obtain the solution and dispersion relation:

$$u' = u_0 e^{\frac{g}{2S}x} \cos\left(\frac{\sqrt{g^2 - 4\omega^2 S}}{2S} x - \omega t \right) \tag{4.18}$$

With this result, we can make a couple of observations:

1. There is a length scale in the solution that was not in the uniform atmosphere. This shows up in the amplitude that now increases exponentially with distance and approaches the sound speed of the atmosphere. This is shown in Figure 4.14. An increasing amplitude is reasonable because the background density decreases with distance, so there is less mass for a wave to push as it propagates with the same momentum. The implication is that energy will be dissipated at a greater rate as the amplitude grows. In this linear analysis, it also appears that a subsonic wave will evolve into a shock more quickly because its Mach number increases as it progress. In reality, this puts us into the non-linear regime, and equation (4.18) may no longer hold.
2. An interesting issue in the isothermal atmosphere is that there is a minimum value for ω, below which sound waves will not propagate. We find this point by recognizing that the radical in the dispersion relation must be real and therefore (g^2 - $4\omega^2 S$) must be positive. This gives us the constraint on ω:

$$\omega > \frac{g}{2\sqrt{S}}. \tag{4.19}$$

This constraint will be discussed further in the numerical analysis.

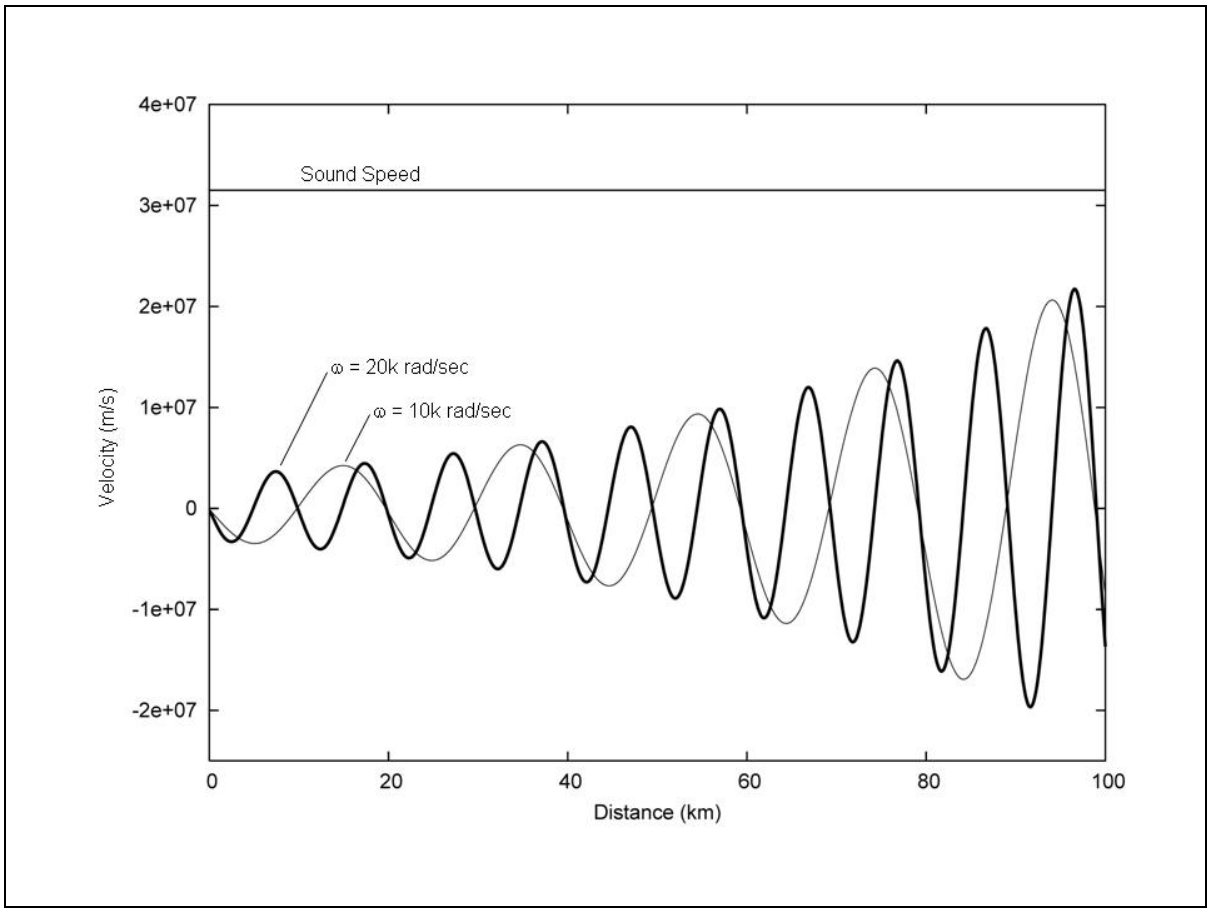

Figure 4.14 - Equation (4.18) from linear analysis is plotted for two frequencies along with the back ground sound speed.

4.3.3 Numerical Analysis

The numerical simulations were configured with g = 4.0e10 m/s^2, and S = 1.0e15 m^2/s^2, which makes the exponential scale height, according to equation (4.9), 25 km. The background density and pressure were configured such that the left-hand boundary (PNS face) had typical values of the atmosphere just above the PNS during the supernova post-bounce phase, i.e. ρ_0 = 1.6e14 kg / m^3 and p_0 = 1.6e29 N / m^2. The density and pressure then fell exponentially according to equations (4.9) and (4.10). From prior analysis, Γ should be

set to 1.0, but in the computer simulation, Γ=1.0 will give "divide by zero" errors because of the energy equation (2.8). This problem was avoided in the analytical analysis as the ($\Gamma - 1$) terms dropped out before the final solution. To circumvent this problem in the computer simulation, Γ was set to 1.00001, which did not give "divide by zero" errors and provided very nearly the same results.

A simulation was first run with a low initial velocity perturbation of Mach .002 at a resolution of 56 zones / wavelength. Figure 4.15 shows both this velocity wave and the velocity wave predicted by linear analysis according to equation (4.18). Initially, the amplitude of both waves increased exponentially, which was expected as the density decreased with distance and there was therefore less mass to move for a given amount of momentum in the wave. As discussed in section 2.3, acoustic waves continuously steepen because of the difference in peak and trough velocities. For a uniform atmosphere, a disturbance generated at Mach .002 would travel 125 wavelengths before the peak catches up with the trough and the wave develops into a full shock. In an atmosphere defined by an isothermal equation of state, where the density drops exponentially, the peak velocity of the wave grows exponentially and wave steepening therefore progresses much more rapidly. In Figure 4.15, steepening becomes noticeable after a wave has traveled about 11 wavelengths, and develops into a full shock after having traveled only about 20 wavelengths. The rate of energy dissipation (represented by the change in *S*) shown in the Figure 4.15 picks up around this point but then levels off. The dissipation rate levels off because the velocity wave amplitude levels off. For this perturbation, the amplitude decay caused by dissipation is

approximately canceled by the amount of growth caused by decreasing density. The rate of energy dissipation tracks with the velocity wave amplitude.

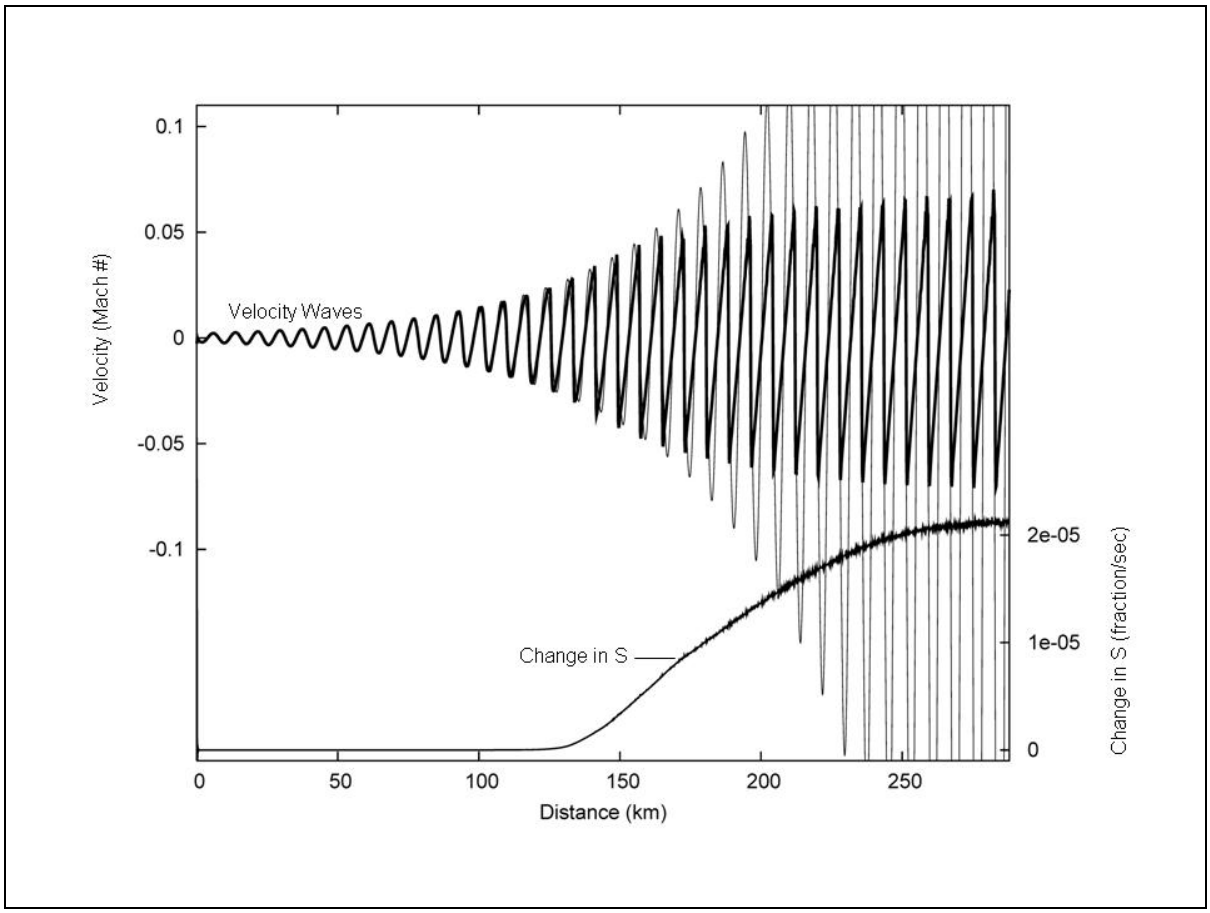

Figure 4.15 - Velocity waves from a Mach .002 perturbation shown for both the numerical simulation (dark line) and the linear analytical analysis (light line). The fractional rate of change of entropy is also shown. The change in entropy curve is established immediately and, aside from some noise, remains steady throughout the simulation. This numerical simulation was run with a resolution of 56 zones per wavelength.

Increasing Amplitude

The simulation was repeated with larger perturbations. Figures 4.16 and 4.17 show results for initial disturbances of Mach 0.1 and 1.0 respectively. In these scenarios, the shock

formed sooner, so energy dissipation began sooner. As can be seen in both cases, once the shock fully formed the wave amplitude began to decay. This is because the amount of amplitude decay from dissipation was greater than the amount of amplitude growth from the decreasing density. As a result of this net amplitude decay, the amount of energy dissipation also decreased. This basic energy dissipation profile was seen in all tested perturbations (up to Mach 1.0). The peak rate of energy dissipation, where it occurs and the subsequent rate fall off were all dependent on the magnitude of the perturbation. Figure 4.18 shows the peak rate of energy dissipation for each simulation plotted as a function of the initial perturbation velocity.

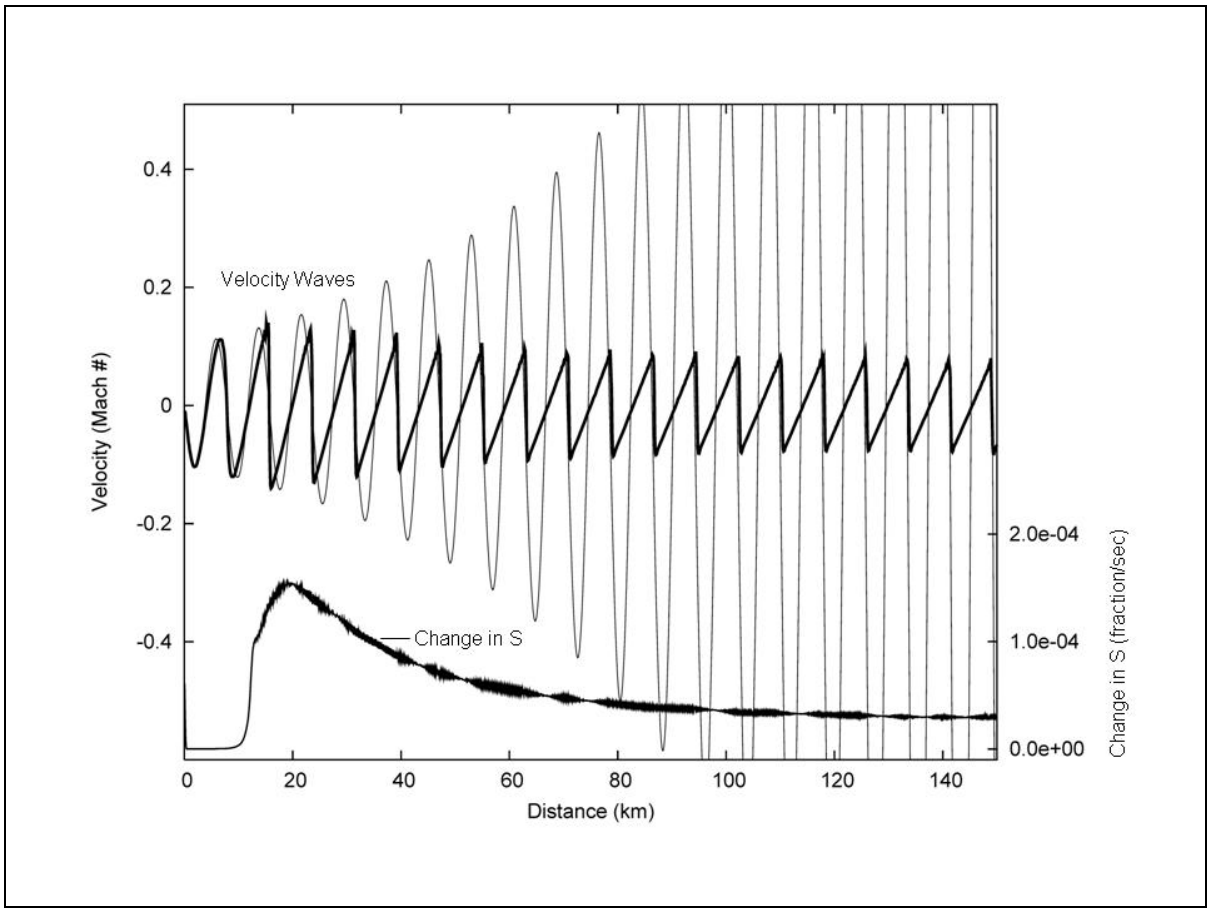

Figure 4.16 - The velocity wave and the rate of change of entropy are shown for a Mach 0.1 perturbation. The dark line is velocity wave from the numerical simulation and the light line is the velocity wave from the linear analytical analysis. Recall that the exponential scale height of the pressure and density was 25km. As in the Mach .002 simulation, the rate of change in entropy remained steady throughout the simulation. This simulation was also run with a resolution of 56 zones per wavelength.

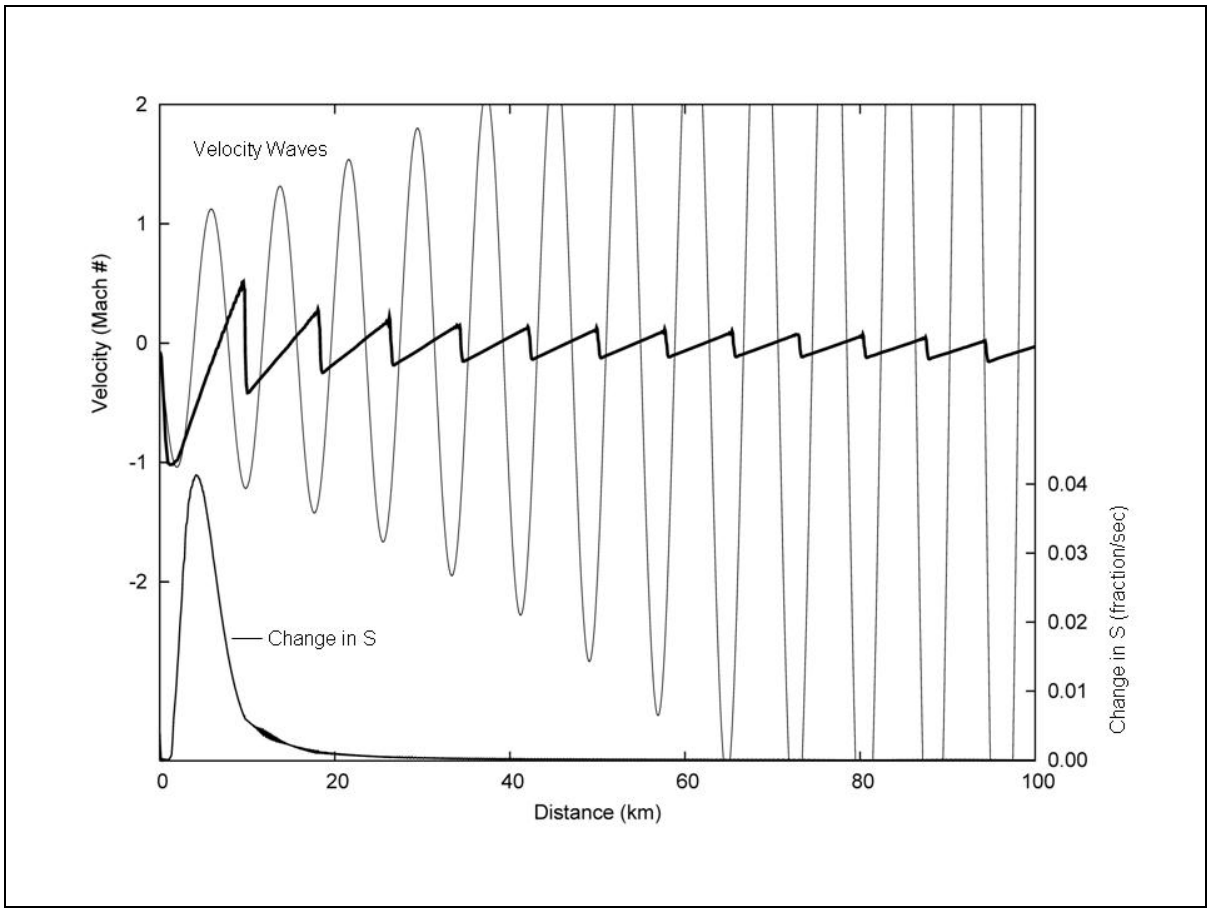

Figure 4.17 - The velocity wave and the rate of change of entropy are shown for a Mach 1.0 perturbation. The dark line is velocity wave from the numerical simulation and the light line is the velocity wave from the linear analytical analysis. As in the Mach .002 simulation, the rate of change in entropy remained steady throughout the simulation. This simulation was also run with a resolution of 56 zones per wavelength.

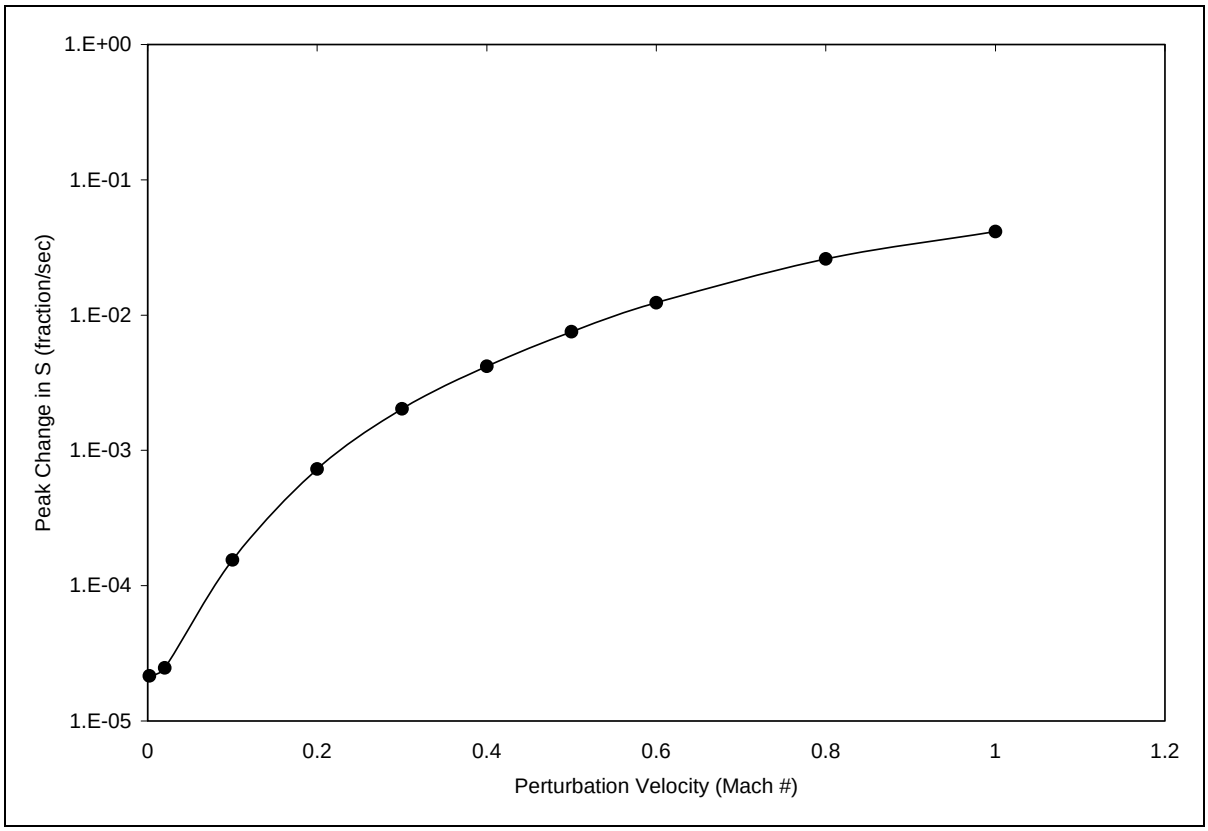

Figure 4.18 - The peak energy dissipation rate is shown as a function of the initial perturbation velocity. Measurements from the simulations are represented by the dots, and a polynomial trend line is superimposed.

Frequency Dependence

There is frequency dependence in the isothermal atmosphere that did not exist in the uniform atmosphere. In general, there was a predictable spatial dependence on frequency as the point where shocks would form and dissipation began tracked with the number of wavelengths, which was of course affected by frequency. This can be seen in Figures 4.19, 4.20 and 4.21, which show results at three different frequencies. The peak energy dissipation rate was not affected by changes in frequency.

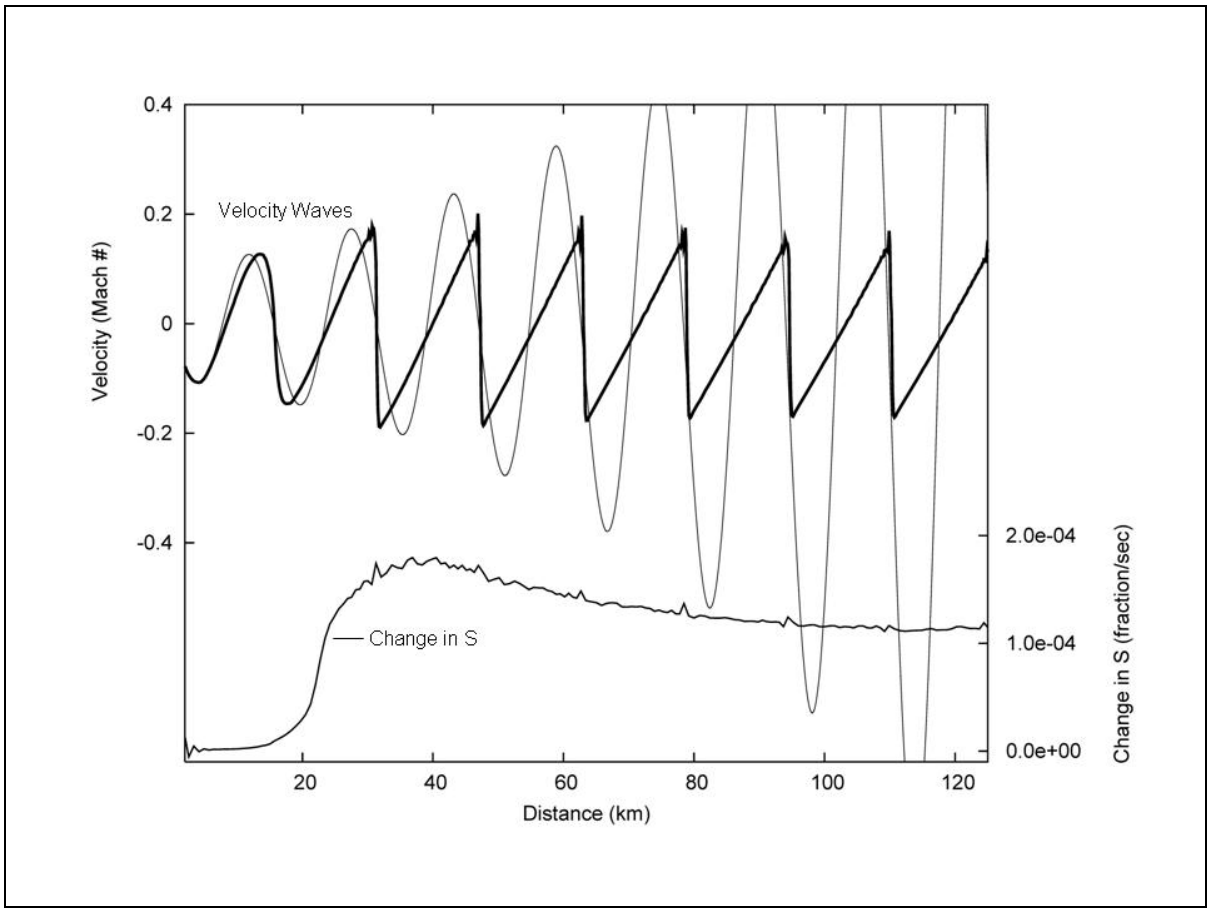

Figure 4.19 - The velocity wave and the rate of change of entropy are shown for ω = 1.26e4 rad/sec, with a Mach .002 perturbation. The dark line is velocity wave from the numerical simulation and the light line is the velocity wave from the linear analytical analysis.

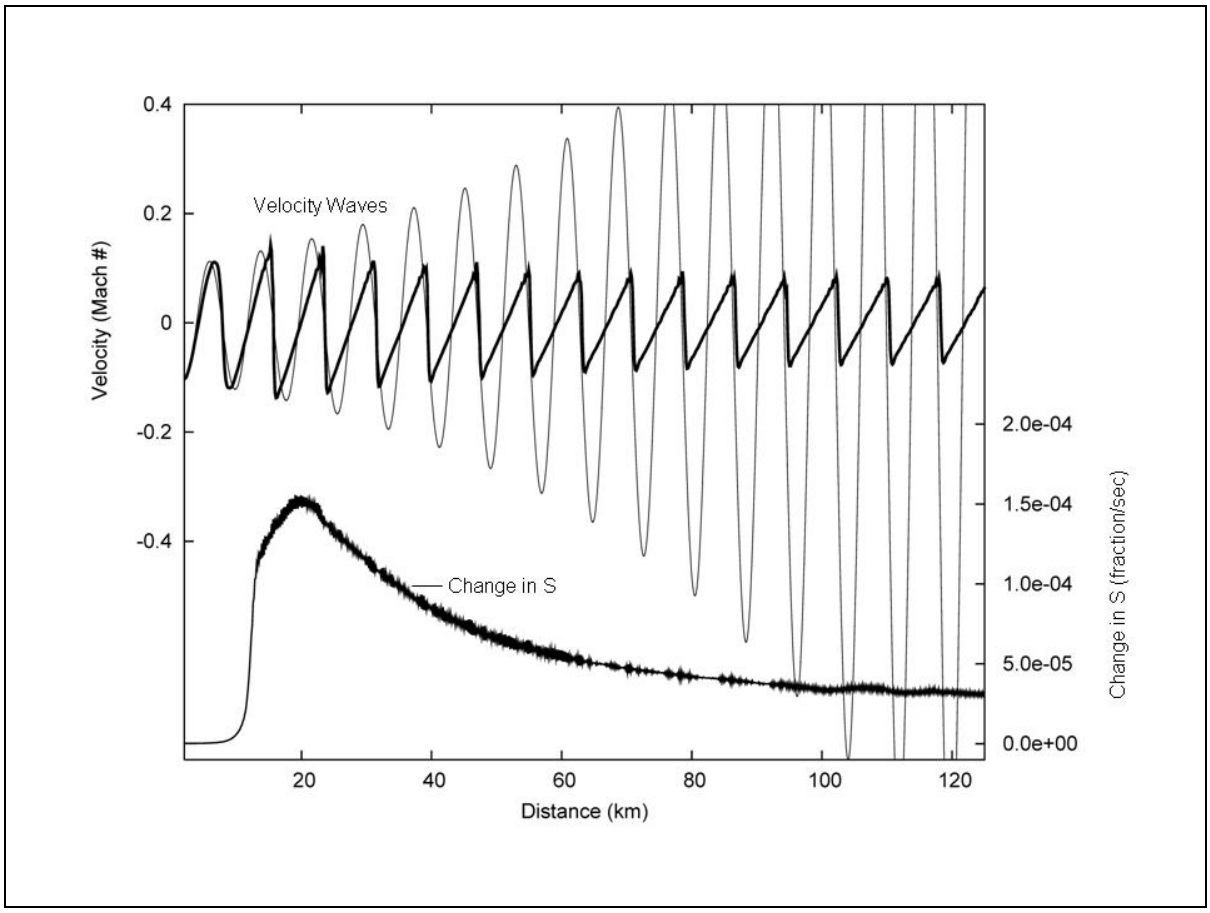

Figure 4.20 - The velocity wave and the rate of change of entropy are shown for ω = 2.52e4 rad/sec, with a Mach .002 perturbation. The dark line is velocity wave from the numerical simulation and the light line is the velocity wave from the linear analytical analysis.

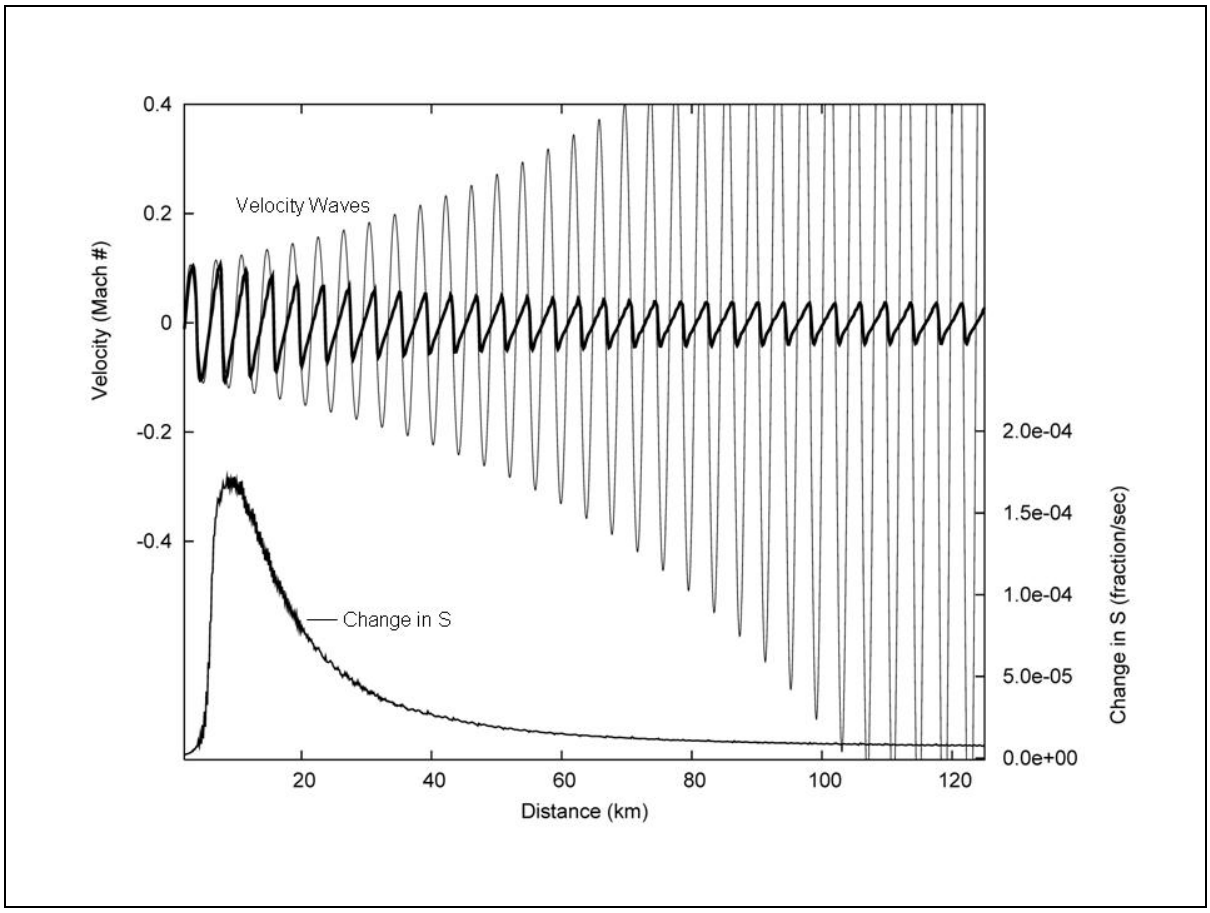

Figure 4.21 - The velocity wave and the rate of change of entropy are shown for ω = 5.04e4 rad/sec, with a Mach .002 perturbation. The dark line is velocity wave from the numerical simulation and the light line is the velocity wave from the linear analytical analysis.

Recall equation (4.19) in the analytical analysis that indicates that the driving frequency must be greater than $g/(2\sqrt{S})$. Plugging in values for g and S, this means that ω must be greater than 630 rad/sec. In numerical simulations, I found that acoustic waves became frozen in space and would not propagate with ω less than about 1,000 rad/s. Given that the upper end of this study is set by the radial oscillation frequency of the PNS around 12k rad/sec (refer to section 3.4), this is a reasonable agreement.

4.4 Case 3 – Varying Sound Speed

4.4.1 Description

We can create an atmosphere where the sound speed is inversely proportional to the square root of the distance (which agrees with the Janka hydrostatic model of the post-shock atmosphere) by setting the background pressure constant, $p_e = p_c$, and having the density increase directly with distance, $\rho_e = \rho_c x$. By making the background pressure constant, the gravitational force is zero, further simplifying the model.

To see that these definitions for p and ρ give the desired result, let's first write the equation for sound speed in a more useful form by substituting the equation of state (2.1) into the definition of sound speed (2.37) to obtain

$$c_s = \sqrt{\Gamma \frac{p_e}{\rho_e}} . \tag{4.20}$$

Now, by substituting the above definitions for p_e and ρ_e into (4.20), we obtain the desired sound speed for this case:

$$c_s = \sqrt{\Gamma \frac{p_c}{\rho_c x}} . \tag{4.21}$$

4.4.2 Linear Analytical Analysis

We will start the investigation with the usual linear analytical analysis. Begin with Euler's equations for momentum and energy in 1D, equations (2.6) and (2.7), and follow the usual prescription:

- Linearize the equations, where ρ_e and p_e are defined above and u_e =0.
- Drop small terms.
- Take the time-derivative of the momentum equation and the space-derivative of the energy equation.
- Subtract the two resultant equations.

The final result is the wave equation,

$$\rho_c x u'_{tt} - \Gamma p_c u'_{xx} = 0 \tag{4.22}$$

Making the substitution $u' = X(x)\ T(t)$ and separating variables, we obtain the temporal and spatial equations:

$$T_{tt} + \omega^2 T = 0$$
$$X_{xx} + \frac{\rho_c}{p_c}\frac{\omega^2}{\Gamma} xX = 0$$

As usual, the temporal solution is simply $\cos(\omega t)$. The solution to the spatial equation was found by using the general solution to this 2nd order differential equation on the EqWorld website [EqWorld]. With our coefficients, the solution is

$$u' = C\sqrt{x} J_{1/3}\left(\tfrac{2}{3}\omega\sqrt{\frac{\rho_c}{\Gamma p_c}}(x)^{3/2} \right), \tag{4.23}$$

where C is the normalization constant proportional to u_0 and $J_{1/3}$ is the Bessel function of the first kind with an index of ⅓. Substituting in the sound speed, this becomes

$$u' = C\sqrt{x} J_{1/3}\left(\frac{2\omega}{3c_s} x \right),$$

and letting $k = (2\omega)/(3c_s)$, the equation finally becomes

$$u' = C\sqrt{x}J_{1/3}(kx). \tag{4.24}$$

Equation (4.24) can be simplified by using the approximation for the non-integer Bessel function given in the *Handbook of Mathematical Functions* [Abramowitz and Stegun 1972]:

$$J_n(\bar{x}) \cong \sqrt{\frac{2}{\pi\bar{x}}}\cos\left(\bar{x} - \frac{n\pi}{2} - \frac{\pi}{4}\right), \tag{4.25}$$

where the bar is drawn over x to show that it is not the same x in equation (4.23). Equation (4.25) is exact for select indices, such as $n = ½$, though not for our case of $n = ⅓$. According to Abramowitz and Stegun, this approximation is valid for $x >> |n^2 - ¼|$. For $n = ⅓$ and using the argument of the Bessel function in equation (4.23), this means that equation (4.25) is valid for $x >> 0.3$. To further confirm the validity of this equation, I compared it to non-integer numerical solutions found in *Numerical Recipes* [Teukolsky], and to order 0 and 1 Bessel functions available in the plotting software, *Gnuplot*. The finding was that equation (4.25) showed agreement with the other solutions after the first quarter wavelength (about $x = 3$). This agreement is borne out in Figure 4.23. With this restriction in mind, this approximation for the Bessel function is very useful for comparison to the numerical result after the first quarter wavelength.

Plugging equation (4.25) into the velocity equation (4.23), along with $\Gamma = ⅔$ and $n = ⅓$, we arrive at the dispersion relation:

$$u' \cong C\left(\frac{2\sqrt{3}}{\omega\pi}\right)^{1/2}(x)^{-1/4}\cos\left(\frac{\omega}{\sqrt{3}}(x)^{3/2} - \frac{5\pi}{12}\right). \tag{4.26}$$

With this equation, we can see that in an atmosphere where the sound speed decreases with distance, there is a length scale not only in the amplitude, as in the isothermal atmosphere, but also in the wavelength:

1. Amplitude: The velocity amplitude decreases with distance, which is reasonable because the background density increases with distance, so there is more mass for a wave to push as it propagates with the same momentum. While this decreasing amplitude tends to decrease the rate that energy is dissipated, we can also note that the sound speed falls off at a greater rate than the wave amplitude ($x^{-½}$ versus $x^{-¼}$), which can be seen in Figure 4.22. By this argument, a wave such as one initially at Mach 0.5, could become supersonic by the time it reached the accretion shock; however, as indicated in the last section, this puts us into the non-linear regime where equation (4.26) is no longer valid, and we must rely on numerical analysis.
2. Wavelength: The wavelength decreases with distance, which is indicative of the decreasing sound speed. The implication of this is that the amount of energy dissipated in a volume depends on frequency.

These characteristics will be demonstrated in the numerical analysis.

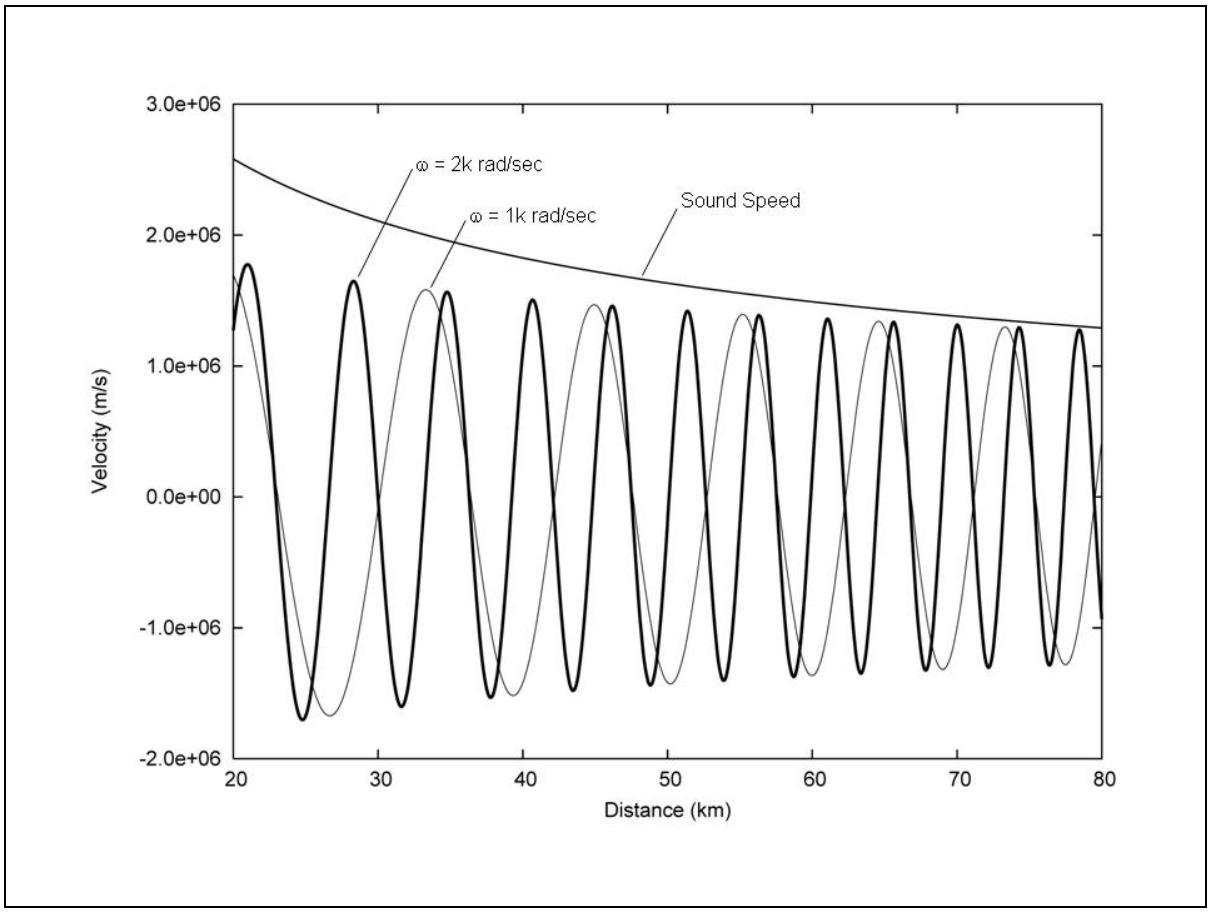

Figure 4.22 - Equation (4.26) from linear analysis is plotted for two frequencies along with the back ground sound speed.

4.4.3 Numerical Analysis

In the numerical simulations, the constant background pressure was given the value p_c = 1e27 N/m^2, which is a typical value for the post-shock atmosphere around 100 km from the surface of the PNS. The background density at the left-hand boundary (x = 0) was given the value ρ_c = 1e13 kg/m^3, which is also a typical value around 100 km from the surface of the PNS. The background density then increased with distance according to $\rho = \rho_c x$. The usual gamma of $\frac{4}{3}$ was used, and the typical driving frequency was 4,000 rad/sec.

Numerical Issues

In these simulations, there were two numerical issues to account for: peak shaving (discussed in section 5.2) and wave spreading. As previously discussed, the amount of peak shaving can be controlled by the resolution used. At the time, resolution was defined as the number of numerical zones per wavelength. In this case, the wavelength decreases with distance while the spatial resolution is fixed, so the number of zones per wavelength decreases with distance. In what follows, I will use the resolution at a distance of 100 km as a representative value for each simulation.

To investigate peak shaving, simulations with small perturbations were used so that shocks would not form in the frequency and spatial ranges being considered. The initial Mach value for these simulations was .001, and three different resolutions were used: 18, 36 and 91 zones/wavelength (at the 100 km point). While the Mach value for a wave in this atmosphere increases with distance, this initial Mach value keeps the perturbations well below the sound speed throughout the spatial range. As a result, shock waves do not form, and the associated energy dissipation and amplitude reduction are not an issue.

As can be seen in Figure 4.23, there was significant peak shaving for the two lower resolution simulations, and this peak shaving increased with distance, which is shown in Figure 4.24.

The other numerical issue encountered was wave spreading, which can also be seen in Figure 4.23, but is more noticeable in the larger perturbation shown in Figure 4.25. We can see here that the wave fronts spread out more at lower resolutions.

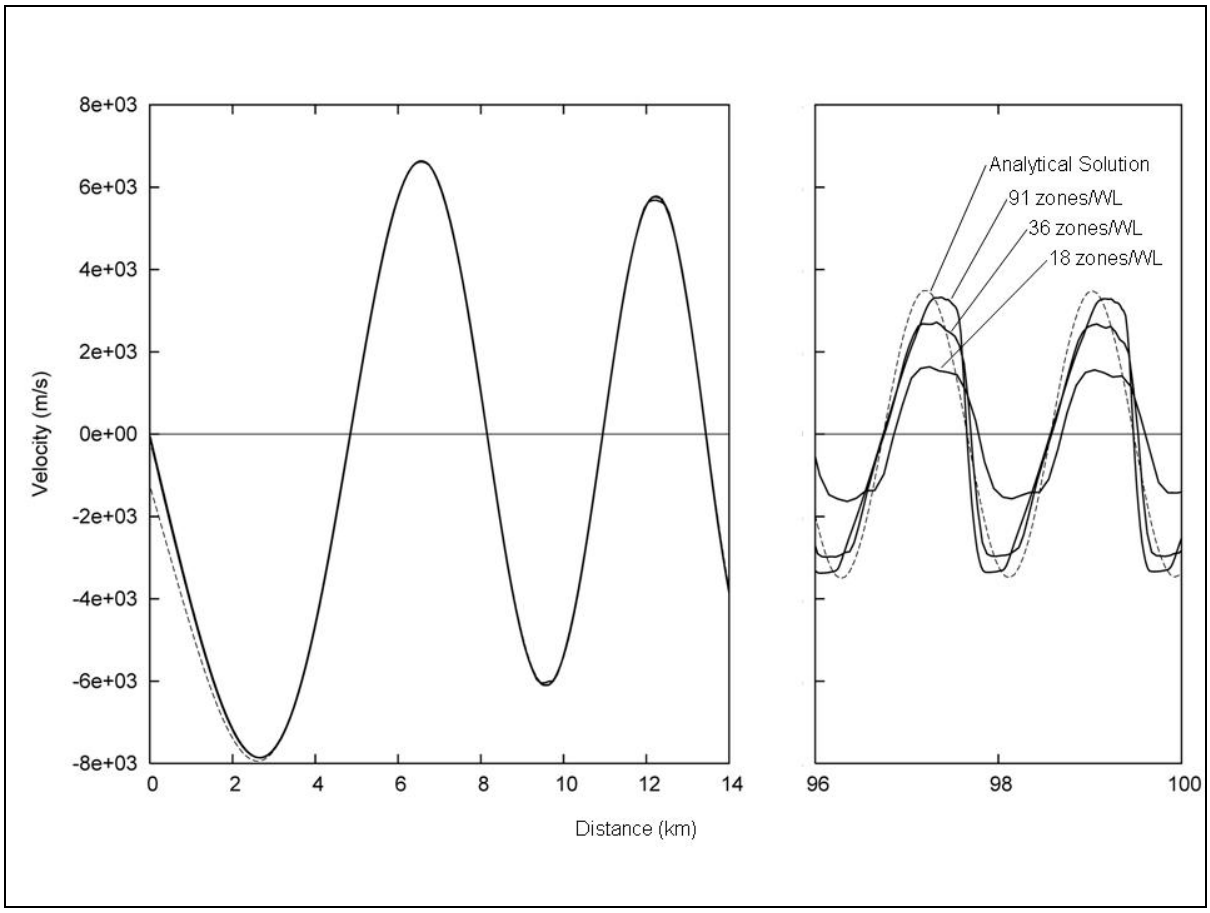

Figure 4.23 - Velocity waves with an initial Mach value of .001 are shown for numerical resolutions of 18, 36 and 91 zones/wavelength (solid lines) along with the linear approximation expressed by equation (4.26) (dashed line). The difference between the analytical solution and the numerical results in the first ¼ wavelength is caused by the approximation used in the analytical equation. Differences in the waves at greater distances are caused by non-linear wave steepening and numerical peak shaving.

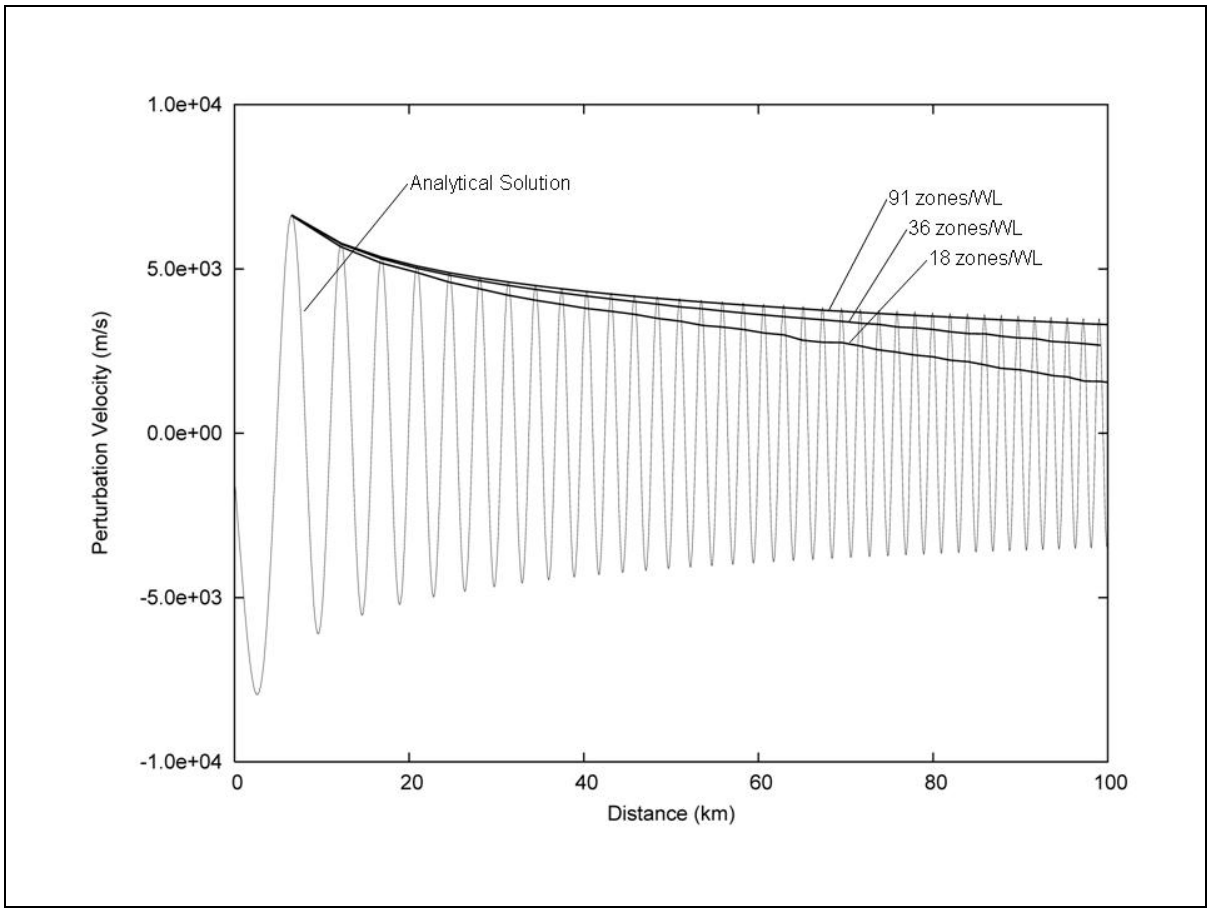

Figure 4.24 - Wave peaks for the velocity waves shown in Figure 4.23 are shown here with dark connecting lines. The full wave from the analytical solution is shown with the light line.

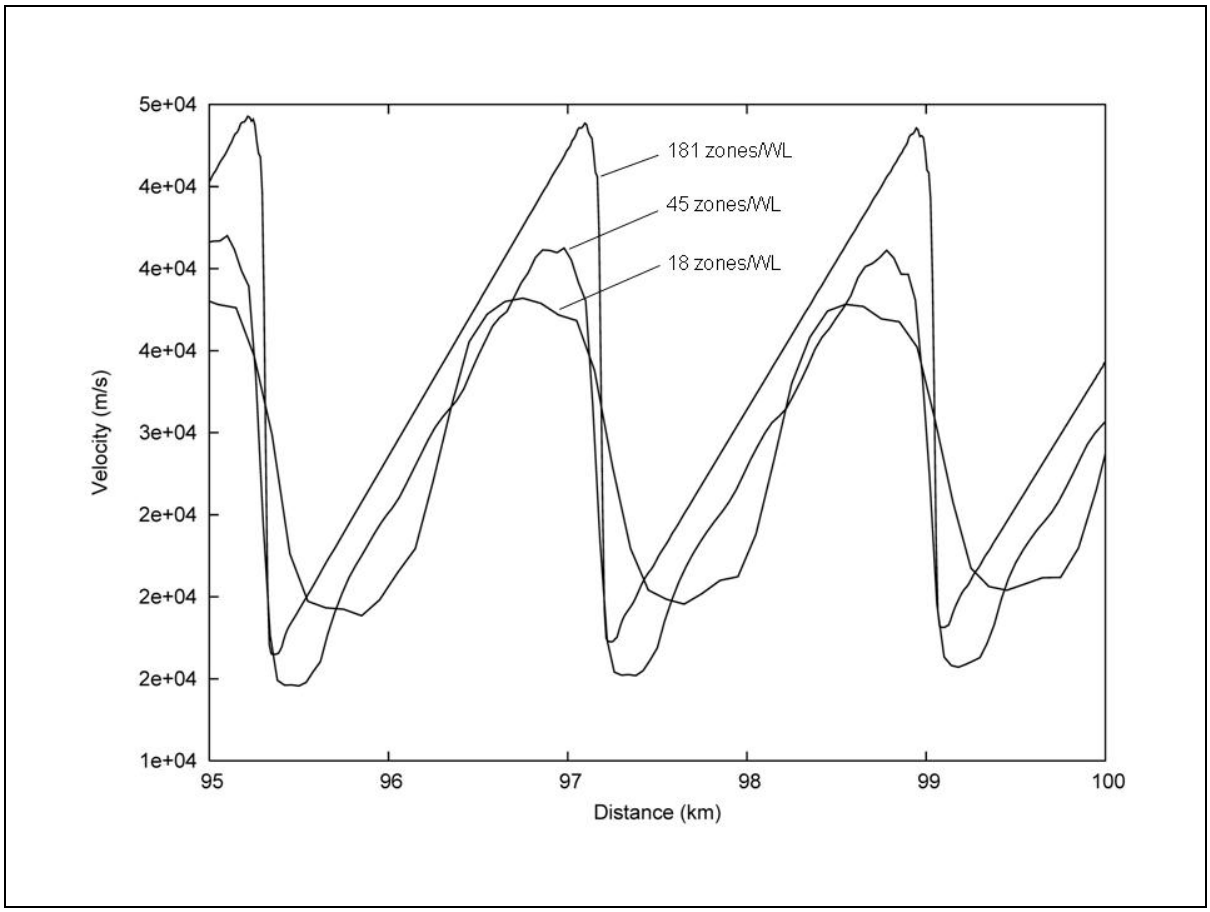

Figure 4.25 - Velocity waves with an initial Mach value of .1 are shown for numerical resolutions of 18, 45 and 181 zones/wavelength. Differences in the waves are caused by numerical peak shaving and wave spreading. Also, the velocity wave has shifted up in value so that it is entirely positive, indicative of bulk fluid flow caused by a large perturbation.

Peak shaving and wave spreading are not in and of themselves problems. The real issue is how energy dissipation measurements are affected by these numerical issues. The rate of energy dissipation (represented by the change in *S*) is shown in Figure 4.26 for four resolutions with initial Mach .001. There was increasing divergence between the simulations with distance. There was little difference between the two highest resolution runs, so using

the highest resolution as the standard, approximate errors were: 80% for res 18, 40% for res 36 and 7% for res 91.

The error seen at larger perturbations was more pertinent to this analysis. Simulations were run with 18, 36, 91 and 181 zones/WL. There was very little difference in the results between the resolutions of 91 and 181. Using the results from the res 181 simulation, therefore, as the standard, peak errors were 50% for res 18, 25% for res 36 and 2% for res 91. Figure 4.27 shows the energy dissipation for resolutions of 18 and 181 zones/WL. Other resolutions fell between these two curves.

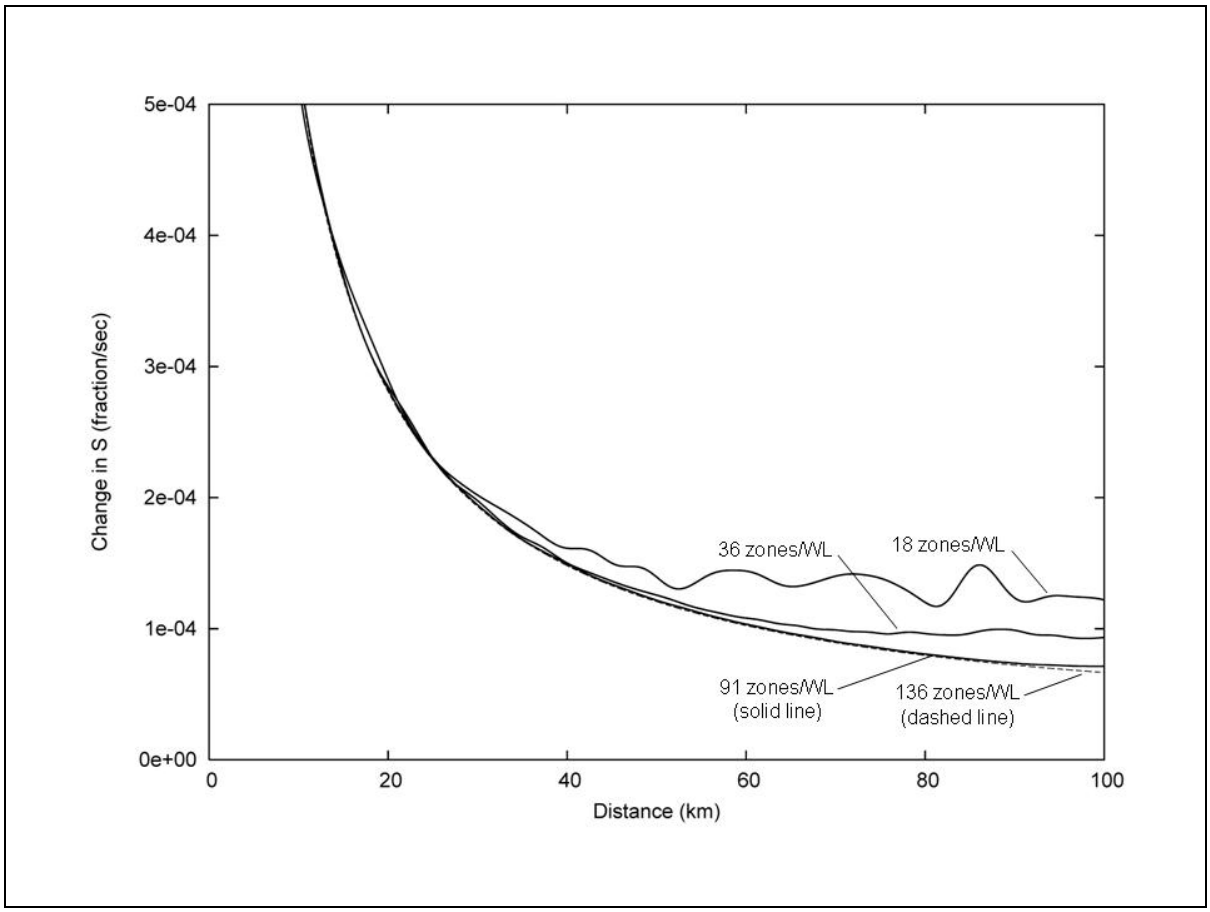

Figure 4.26 - Energy dissipation rate (represented by the change in S) for a perturbation with an initial Mach value of .001 are shown for numerical resolutions of 18, 36, 91 and 136 zones/wavelength. There was enough high frequency noise in the original data that the curves could not be easily distinguished from each other. For this reason, the curves were smoothed with a Bezier function.

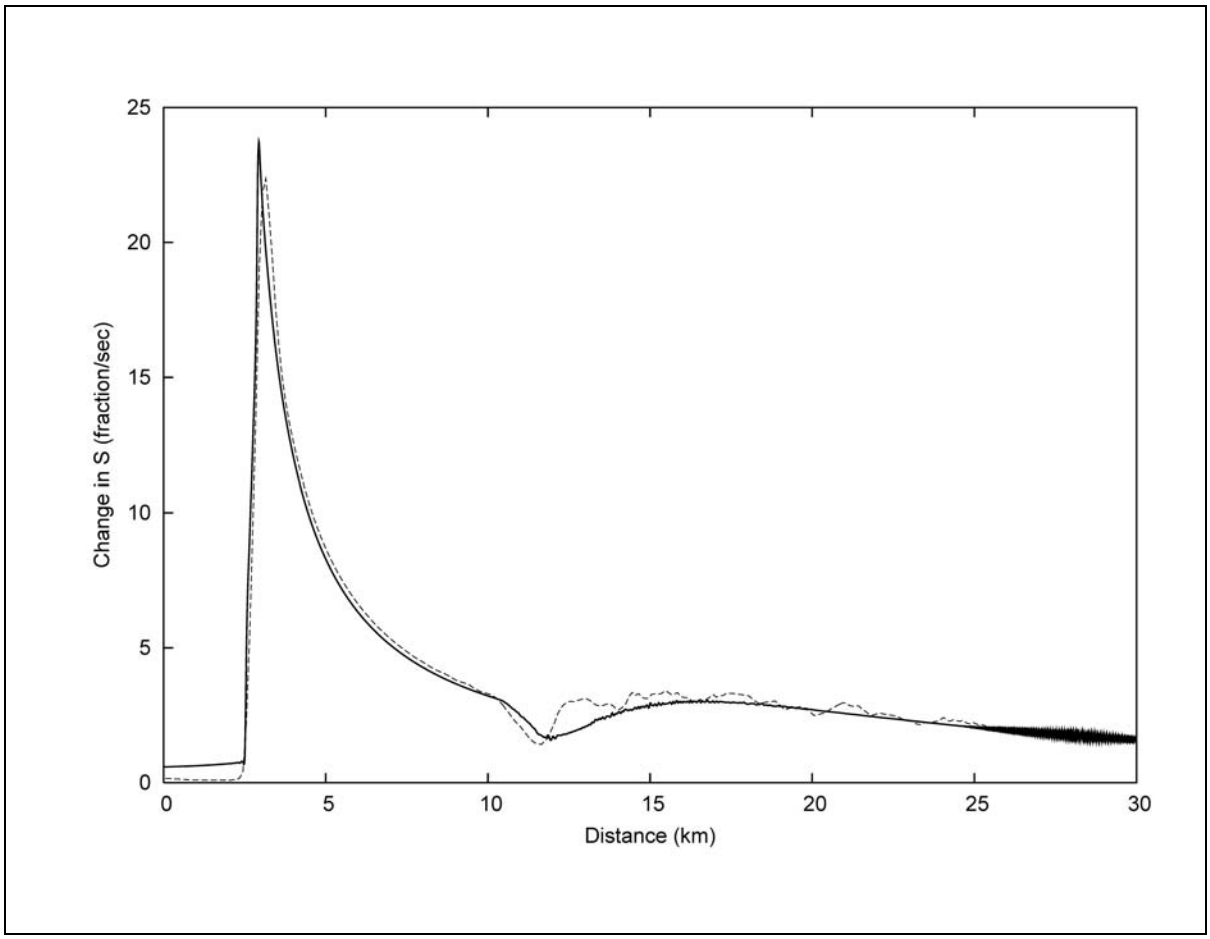

Figure 4.27 - Energy dissipation rate (represented by the change in S) for a perturbation with an initial Mach value of .1 is shown for numerical resolutions of 18 (dashed line) and 181 (dark line) zones/wavelength.

Frequency Dependence

Using the dispersion relation, equation (4.26), it was observed that energy dissipation in the volume would be frequency dependent. Figure 4.28 compares results for three different frequencies, showing how the dissipation profile was affected. Note that the peak dissipation value dropped as a result of changing the frequency in the simulations, but the initial velocity amplitude is arbitrary in this test case, so we should not infer a relationship

between amplitude and frequency here. For a relationship between the driving frequency and amplitude, we can refer back to the analysis of PNS oscillations in Section 3.4.

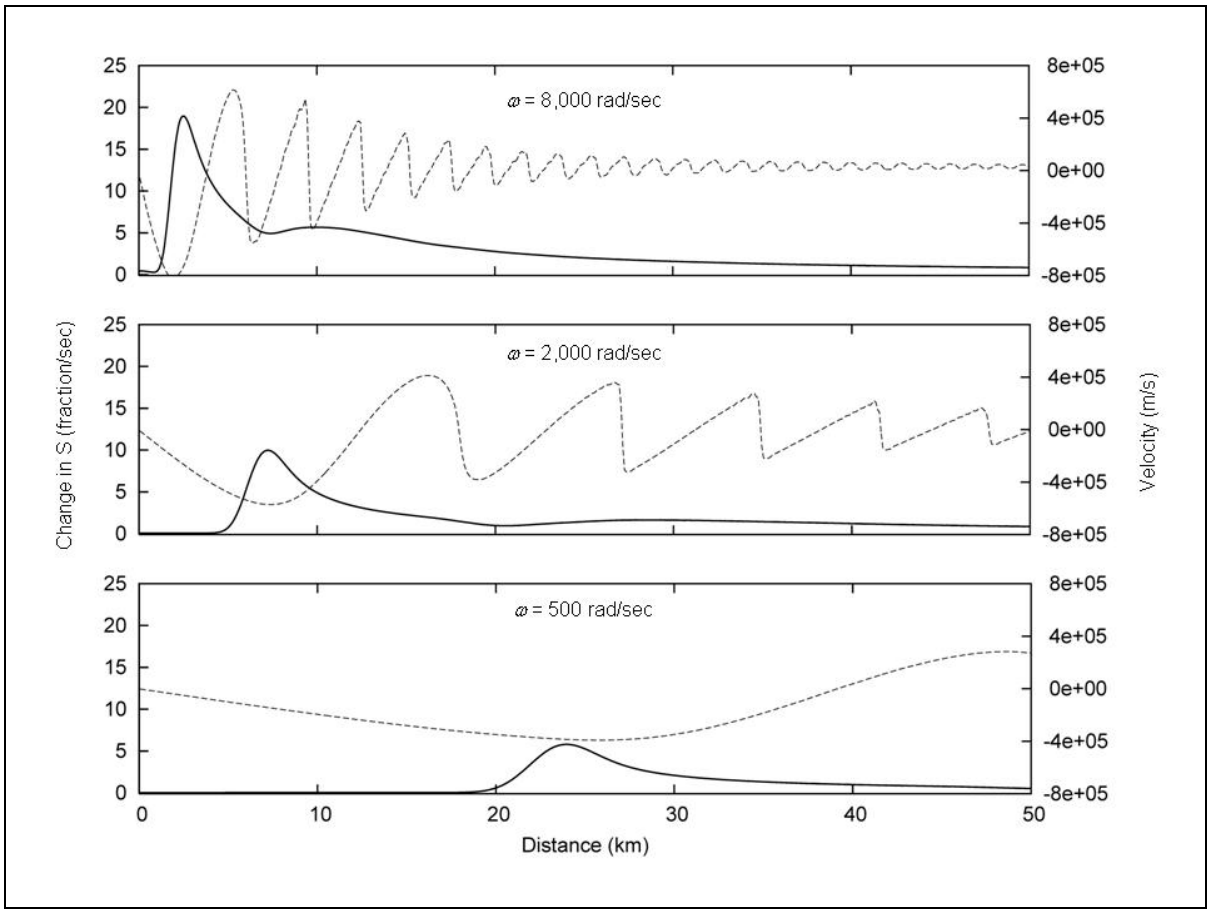

Figure 4.28 - Comparison of energy dissipation rates (represented by the change in S) for three different frequencies. Each perturbation had an initial Mach value of .1 and a resolution of 18 zones/WL. Again, Bezier functions were used to smooth out high frequency noise in these simulations to make the data more readable. The energy dissipation peaks were reduced by this smoothing, but the relative shapes of the curves remained the same.

Bulk motion

As in the uniform atmosphere (Test Case 1), large perturbations caused bulk motion in the isothermal atmosphere. Figure 4.29 shows how the average density in the volume (0-

200 km) decreased as a result over time for perturbations of various sizes. In addition to decreasing density, there was also evidence of bulk fluid motion in Figure 4.28 where the net velocity was positive. In addition to decreasing the density of the atmosphere, the bulk fluid motion increased the background sound speed over time, which in turn and increased the wavelength of the sound waves. This bulk motion was not as noticeable in Case 2. Some difference between Case 2 and the other two models that my have caused this were the decreasing density in Case 2 and the fact that Case 2 included a fixed source of gravity.

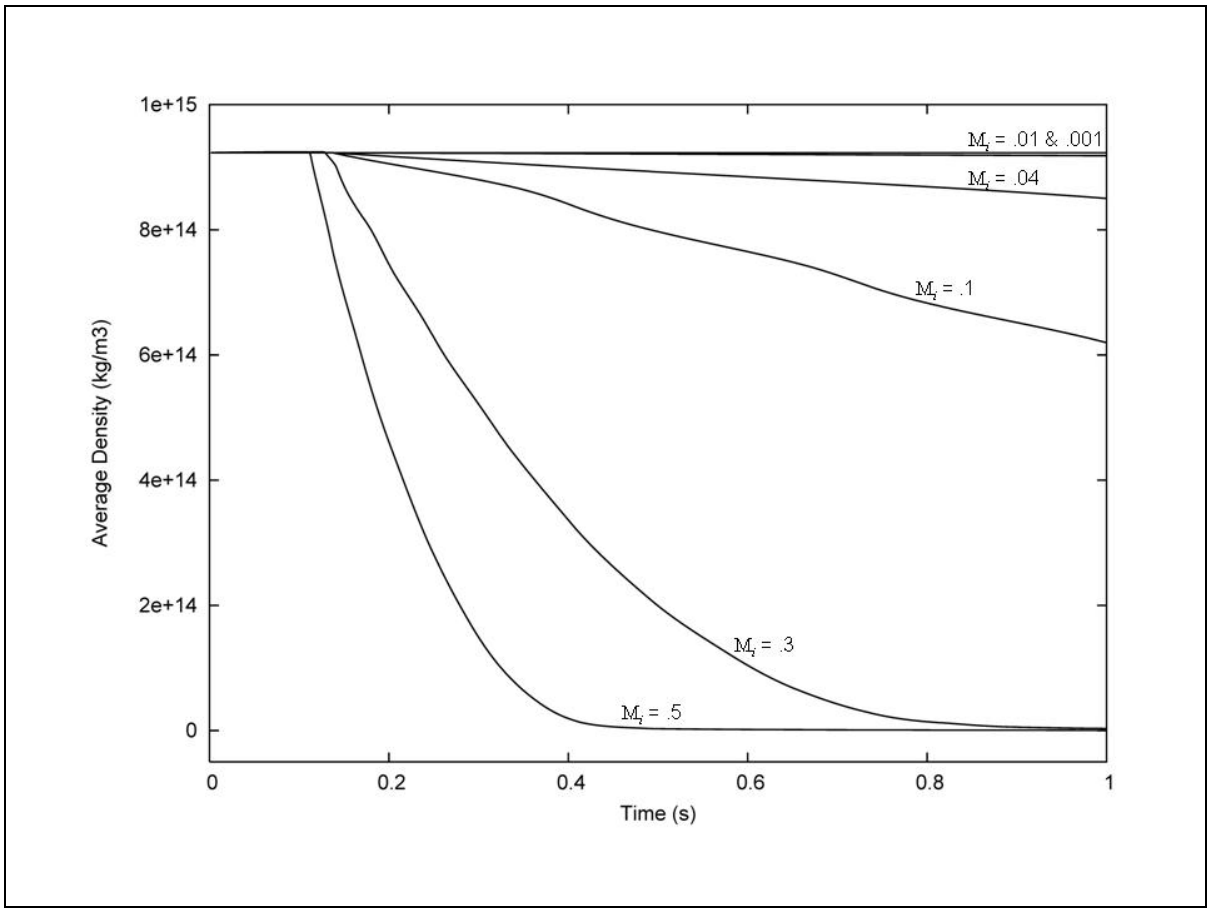

Figure 4.29 - The average density is shown for perturbations of various sizes. The density remains constant for all perturbations until the initial wave reaches the opposite boundary (between .1 and .2 seconds).

Energy dissipation

For all perturbations in this case, mass was pushed away from the oscillating boundary leaving a low density of ρ_0. Elsewhere in the volume, the density dropped nearly uniformly. The zone of low, flat density between the oscillating boundary and the point where the density begins to increase (marked with an 'A' in Figure 4.30) dissipated essentially no energy. At point 'A', the energy dissipation spiked up and then decayed exponentially. This decay in energy dissipation seems to be associated with the decreasing

velocity amplitude, which is a result of the increasing background density and energy dissipation.

For small perturbations, such as Mach .001, the zone of low, flat density was very small and the location of point 'A' was fixed, at least within the one second time frame of the stalled accretion shock.

For large perturbations, such as Mach 0.1, point 'A' moved with time in the positive *x*-direction, and the energy dissipation spike moved with it. This increased the size of the low, flat density zone over time. This motion coincided with the bulk motion of the atmosphere in the direction of wave propagation. The energy dissipation at point 'A' may be associated with mass being forced away from the oscillating boundary, and is only prominent when no gravity is included in the model. In the full supernova problem, the interface region between the PNS and the atmosphere is complex and cannot be adequately addressed by a purely hydrodynamic model. For this reason, further investigation using this hydrodynamic analysis was not warranted.

When the perturbation was large enough for the sound waves to develop into full shocks, a second surge in energy dissipation occurred at this point (marked with a 'B' in Figure 4.30), with a magnitude less than the original spike. From this point, the energy dissipation rate again decreased exponentially as a result of the decreasing velocity amplitude. This energy dissipation from shocked waves and subsequent decrease was also observed in the previous two test cases.

Predictably, the energy dissipation rate increased as the size of the perturbation increased. Figures 4.31 and 4.33 show the energy dissipation rate for several initial Mach values.

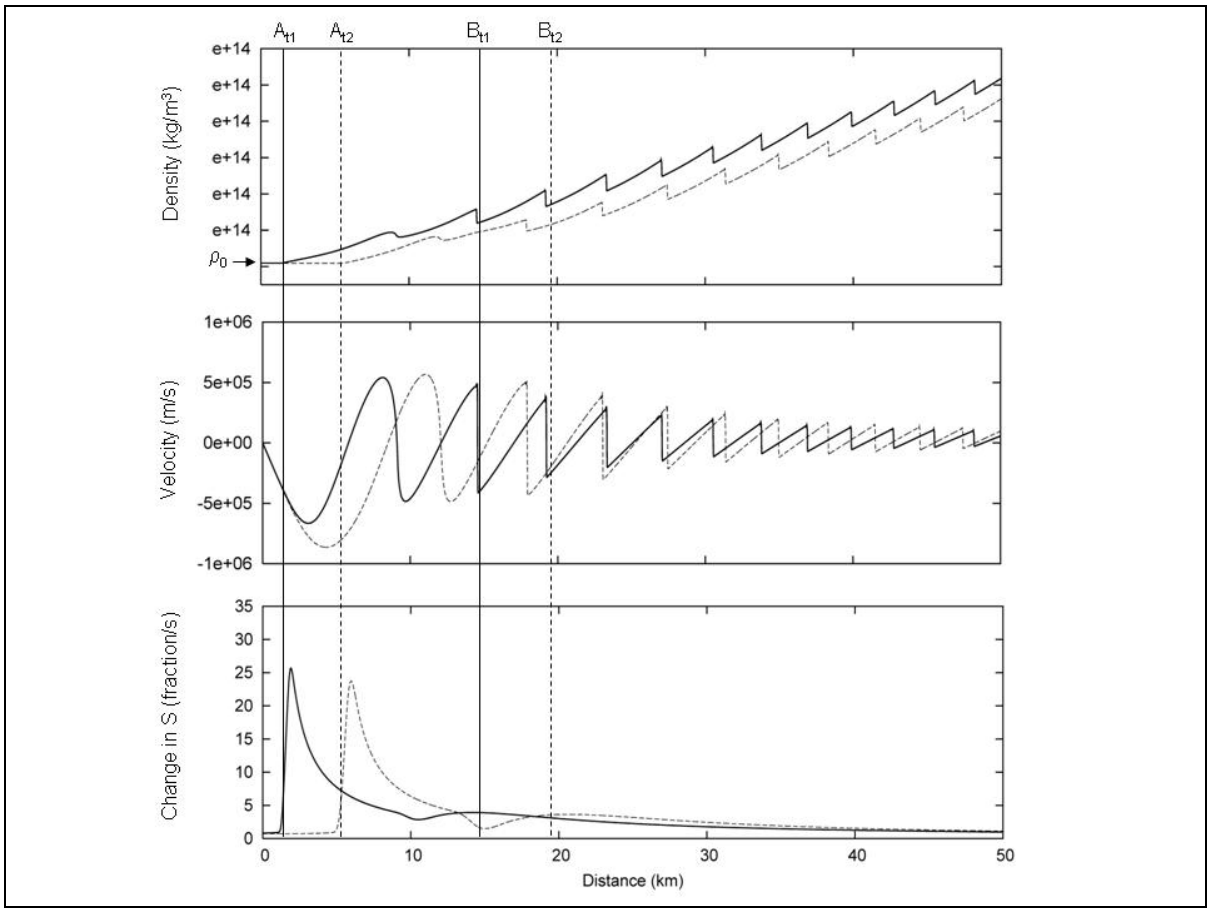

Figure 4.30 - Density, velocity and change in *S* are shown for a simulation with initial Mach value of 0.1. Data is shown for t_1 = .04s and t_2 = .2s. t_1 data is shown with a solid line, and t_2 data is shown with a dashed line. The point where the density begins to increase is marked with an 'A', and the approximate point where the wave turns into a full shock is marked with a 'B'.

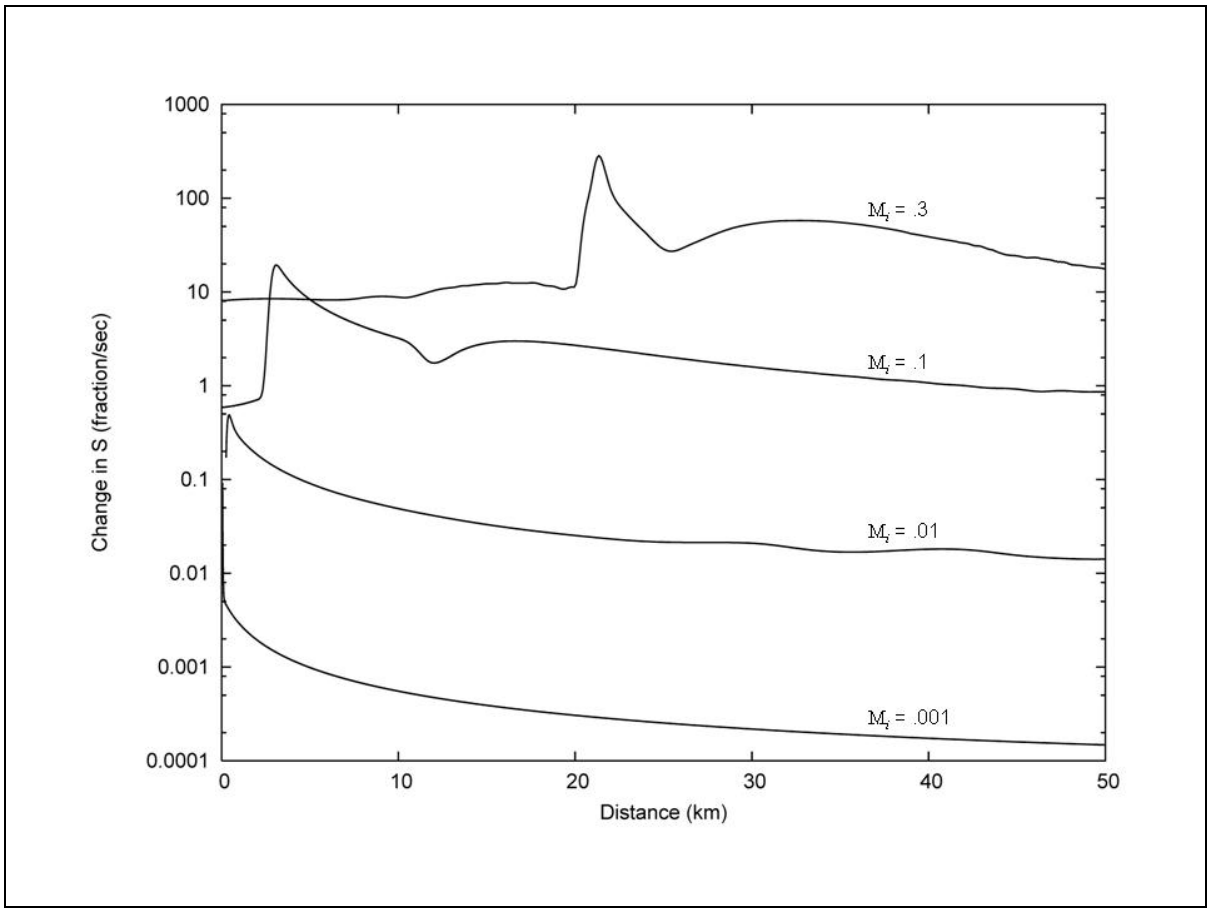

Figure 4.31 - The energy dissipation rate (represented by the change in *S*) is shown on a log scale for four different perturbations. The initial Mach value for each perturbation is indicated as M_i.

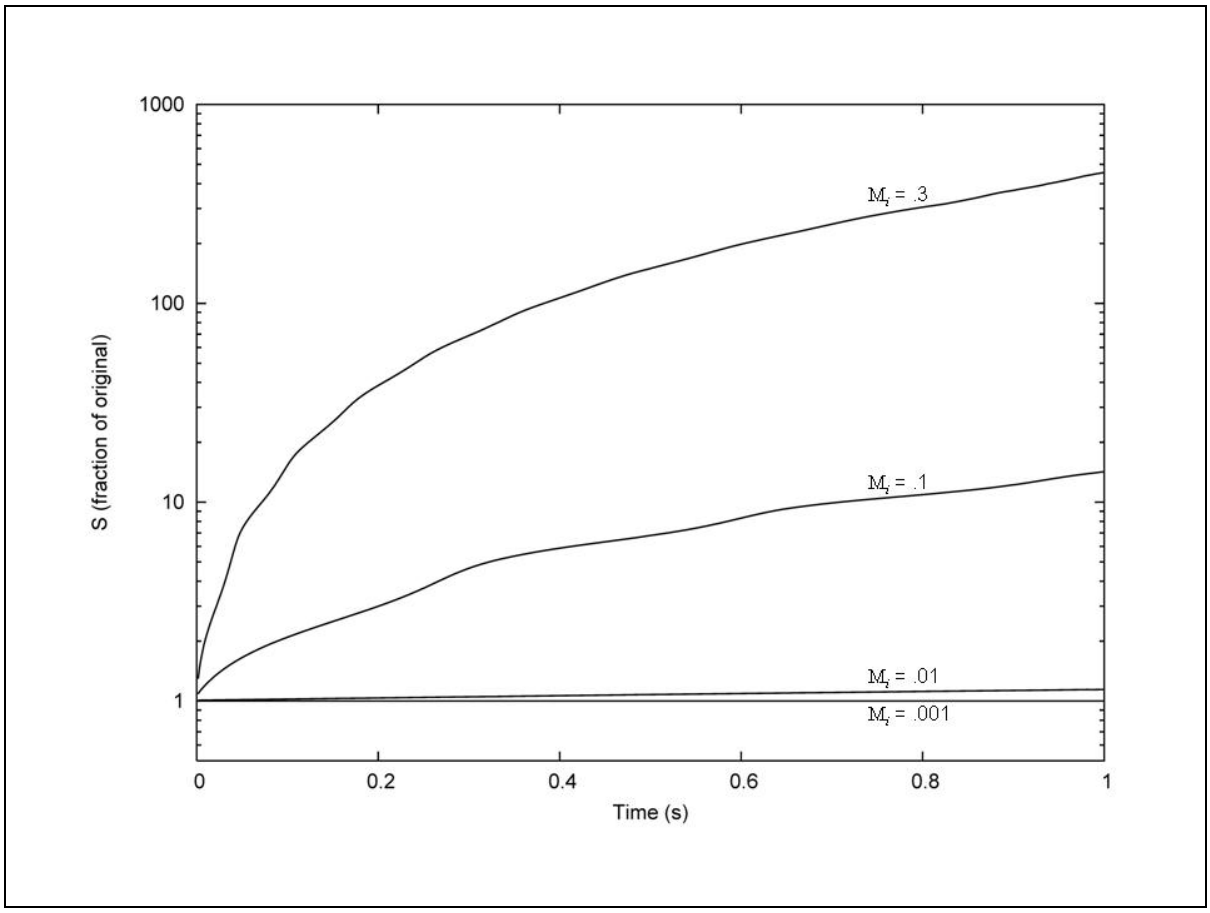

Figure 4.32 - Increasing *S* shows an increase in temperature of the atmosphere as a result of the wave dissipation shown in Figure 4.31.

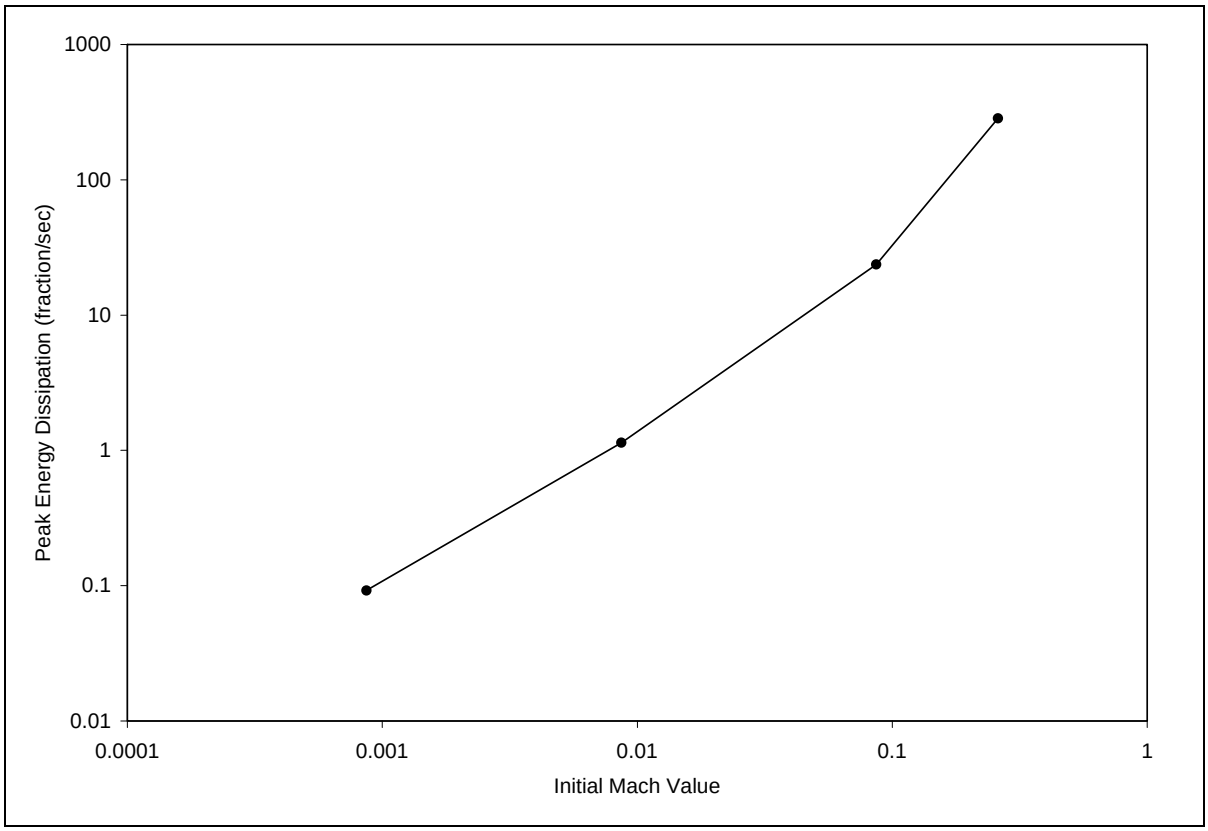

Figure 4.33 - The peak energy dissipation rate is shown for the perturbations in Figures 4.31 and 4.32.

4.5 Case 4 – Full Atmosphere

4.5.1 Description

With the results from the first three test cases, we are now poised to do the realistic atmosphere problem, incorporating the spherical nature of the star and appropriate density, pressure and sound speed profiles.

Up to this point, we have ignored spherical aspects of the problem; however, in the post-shock region, where the radius ranges from about 20 km to about 200 km, the surface area over which the acoustic energy is spread and the magnitude of the gravitational acceleration are sensitive to small changes in distance as waves propagate radially. For example, as a wave propagates 1 km from the surface of the PNS, the surface area over which the wave is spread increases by 10%, and the gravitational acceleration decreases by 9%. In this test case, the spherical geometry of the problem was included in the analytical and numerical analyses.

The background pressure and density in this model were set up with realistic values; pressure varied as $1/r^4$ and density varied as $1/r^3$ in agreement with the Chevalier/Janka model described in section 2.1. These background states can then be written as:

$$\rho_e = \frac{\rho_c}{r^3} \tag{4.27}$$

$$p_e = \frac{p_c}{r^4}, \tag{4.28}$$

where ρ_c is a constant equal to $\rho_{sh} R_{sh}^3$ and p_c is a constant equal to $p_{sh} R_{sh}^4$ (as discussed in section 2.1).

We can also relate ρ_c and p_c to each other with the equation of hydrostatic equilibrium:

$$\frac{dp_e}{dr} = -\rho_e g \,. \tag{4.29}$$

A point source of gravity was assumed with a fixed mass equal to that of the PNS. This simplification discounted the self-gravity of the atmosphere, but allowed the continued use of linear analytical analysis. The Newtonian definitions of gravitational potential and acceleration for a point source are, respectively,

$$\Phi = \frac{GM}{r} \tag{4.30}$$

and

$$g = -\frac{GM}{r^2} \,. \tag{4.31}$$

Ignoring the mass of the atmosphere has little effect on the calculation of gravity near the surface of the PNS, because little atmospheric mass is enclosed in the integration volume; however, the error becomes significant near the stalled accretion shock where the mass of the entire post-shock atmosphere comes into play. To compare the missing mass of the atmosphere at this point to the mass of the PNS, we can first calculate the mass of the atmosphere by integrating the density from a radius of 20 km to 200 km. Using the density equation (4.27), the integral in spherical coordinates is

$$\text{Mass} = \int_{r=20km}^{200km} \int_{\theta} \int_{\phi} \frac{\rho_c}{r^3} r^2 \sin\theta \, dr \, d\theta \, d\phi \,.$$

Solving this integral and using ρ_c = 1e28 kg/m^3, which will be explained subsequently, the mass of the post-shocked atmosphere is approximately 3e29 kg. We have been using a PNS

mass of 1.2 M_0, which is 2.4e30 kg, so the ratio of the missing mass to the total mass is about 1:9 (which also agrees with mass calculations performed in the numerical simulation).

As we can see, the self gravity of the atmosphere may have a significant effect on the results of this analysis, and will be included in the final 1-D and 2-D coupled models. For the purpose of this test case, however, we can leave out this self-gravity and still draw conclusions about acoustic wave behavior in the post-shock atmosphere.

Substituting (4.27), (4.28) and (4.31) into (4.29), we obtain the relationship:

$$p_c = \frac{GM}{4}\rho_c ,$$

so that (4.28) becomes:

$$p_e = \frac{GM}{4}\frac{\rho_c}{r^4} . \tag{4.32}$$

This establishes the initial state of the system for both the numerical and analytical problems and we can begin the analysis using each method.

4.5.2 Linear Analytical Analysis

To solve this system, we will use all three of Euler's equations: (2.5), (2.6) and (2.7). As the waves are now spherical, the analysis will be done in spherical coordinates so that Euler's equations in 1D become:

$$\rho_t + \frac{1}{r^2}(r^2 \rho u)_r = 0 \tag{4.33}$$

$$(\rho u)_t + \frac{1}{r^2}(r^2 \rho u^2)_r + p_r = -\rho g \tag{4.34}$$

$$(\rho \mathrm{E})_t + \frac{1}{r^2}(r^2 \rho u \mathrm{E})_r + \frac{1}{r^2}(r^2 u p)_r = 0, \tag{4.35}$$

where the total energy, E, is defined by equation (2.8). Once again, follow the usual procedure:

- Linearize these equations and drop small terms.
- Take the time-derivative of the momentum equation and the space-derivative of the energy equation, and combine the resultant equations to eliminate the p' terms.
- Incorporate the continuity equation to eliminate the ρ' terms.

The final result is the wave equation:

$$u'_{tt} - \frac{\Gamma GM}{4r} u'_{rr} + \frac{\Gamma GM}{2r^2} u'_r + \frac{(5\Gamma - 8)GM}{2r^3} u' = 0,$$

and setting Γ=4/3 this becomes

$$u'_{tt} - \frac{GM}{3r} u'_{rr} + \frac{2GM}{3r^2} u'_r + \frac{2GM}{3r^3} u' = 0, \tag{4.36}$$

Using the separation of variables technique, we obtain the temporal and spatial solutions below:

$$u'_t = \cos(\omega t) \tag{4.37}$$

$$u'_r = C r^{3/2} J_{1/3}\left(\frac{2\omega}{\sqrt{3GM}} r^{3/2} \right), \tag{4.38}$$

where C is the normalization constant proportional to u_0, u_t' and u_r' are the temporal and spatial components of the velocity, and $J_{1/3}$ is the Bessel function of the first kind with an index of 1/3.

We can again use the Bessel function approximation from the last section, equation (4.25), and write the velocity wave as

$$u_r' \cong Cr^{3/2}\sqrt{\frac{\sqrt{3GM}}{\pi\omega r^{3/2}}}\cos\left(\frac{2\omega}{\sqrt{3GM}}r^{3/2}-\frac{5\pi}{12}\right). \tag{4.39}$$

From this equation, we see a combination of characteristics that were observed in the previous two test cases:

1. Amplitude: The amplitude in the realistic atmosphere increases with distance because the density decreases, as we saw in the isothermal atmosphere (Test Case 2). We also see that the amplitude increases as $r^{3/4}$ while the sound speed decreases as $r^{-1/2}$, so waves again approach the sound speed of the atmosphere as they progress. Both of these conditions tend to increase the dissipation of energy, though as stated before, this equation becomes invalid in the non-linear regime.
2. Wavelength: As in the last test case, the wavelength decreases with distance because the sound speed decreases with distance, a feature that tends to dissipate more energy in the same volume.

These observations can be seen in Figure 4.34.

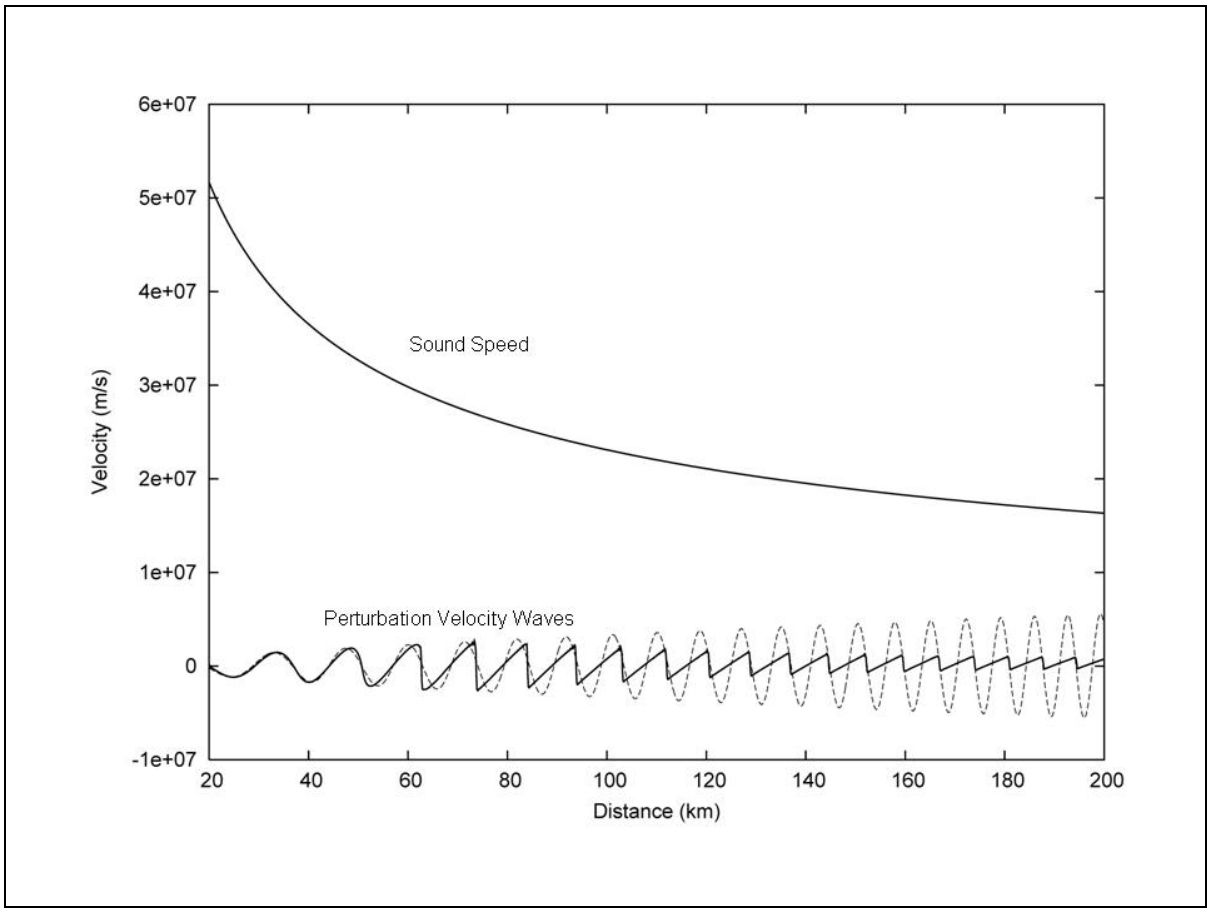

Figure 4.34 - Velocity waves compared to the background sound speed for a perturbation with initial Mach of 0.02. The solid velocity wave is from the numerical simulation and the dashed velocity wave is the linear analytical prediction according to equation (4.39).

4.5.3 Numerical Analysis

In the numerical simulations, the oscillating boundary was set at a radius of 20 km, the approximate radius of the PNS, and the outer boundary was set at a radius of 200 km, the approximate radius of the stalled accretion shock. The background density and pressure were defined by equations (4.27) and (4.28), with ρ_c = 1e28 kg/m^3. This constant was set by applying a typical value of 1.25e15 kg/m^3 for the density just outside the PNS to equation (4.27) (or a typical value of 2.5e30 N/m^2 for the pressure could have been used). M was set

to the estimated PNS mass of 1.2 M_0. The usual gamma of $\frac{4}{3}$ was used, and unless noted otherwise, the driving frequency was 16,000 rad/sec.

Numerical Issues

Peak shaving appeared in this test case as it did in the others. As before, it was controllable by resolution. Wave spreading was less of an issue in this case. Wave spreading is associated with bulk motion of the fluid and subsequent changes in fluid properties. Bulk motion, which will be discussed later in this section, appears to be less of an issue when gravity is included as it is in this case. As these topics have been discussed in some detail already, and recognizing the ultimate goal of understanding energy dissipation, I will jump directly to how resolution affects energy dissipation in this test case.

Resolution will again decrease with distance as it did in Test Case 3. For this reason, I will again use the resolution at the 100 km mark to reference the resolution for each simulation.

As previous discussed, no measurable energy should be dissipated at very low Mach values. Using a small perturbation with an initial Mach of 2e-5 (which becomes about 6e-5 by the time a wave reaches the outer boundary), any energy dissipated in the simulation can be defined as numerical error. When performing simulations with small perturbations, the energy dissipation rate was found to be very stable throughout the simulation. For a simulation with a moderate resolution of 38 zones/WL, the energy dissipation rate (and therefore the numerical error) was 6e-7 fraction/sec. At twice the resolution, or 76 zones/WL, the error was 1e-7 fraction/sec. These and other results are plotted in Figure 4.35.

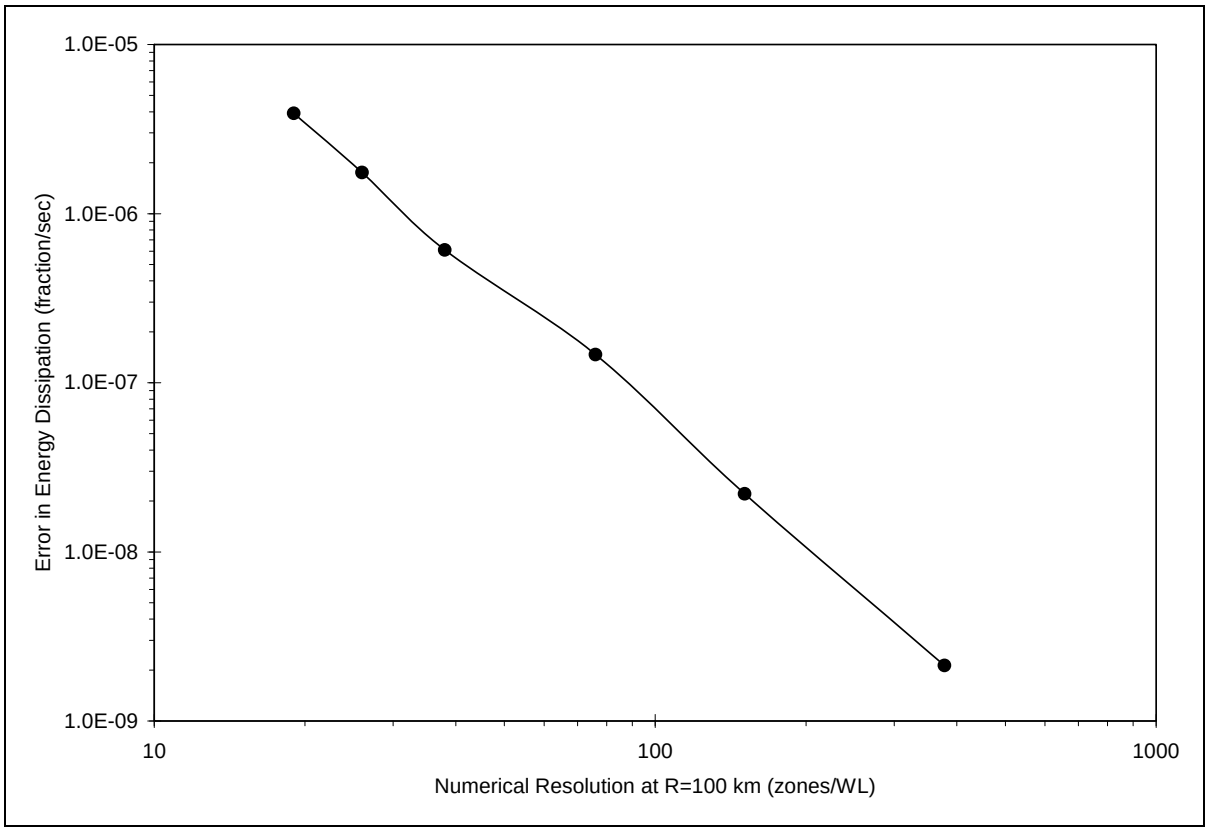

Figure 4.35 - Error in energy dissipation is plotted as a function of resolution, where the resolution was defined at a radius of 100 km. By plotting the logs of *x* and *y* values, the order of convergence was found to be 2.5.

Error analysis was performed with Mach .02 simulations. Less than 1% difference in peak energy dissipation was seen among very high resolutions of 529, 378 and 302 zones/WL. Therefore, using 529 zones/WL as the standard, the following errors were found: 1% at res 151; 2% at res 76; 4% at res 38; 10% at res 23.

Bulk Motion

When using a perturbation with an initial velocity of Mach .02 in the realistic atmosphere, mass was slowly pushed out of the volume, so that after 1 second the average density and therefore total mass had dropped to about half of its original value. Interestingly, the properties of the atmosphere (e.g. wavelength and sound speed) did not significantly change over this time frame. Perturbations much larger than Mach .02 pushed the atmosphere out of the volume much more rapidly, such that many of the simulations could not be completed probably because the density near the oscillating boundary went to zero. The average density for each of these perturbations is plotted versus time in Figure 4.36.

In general, the effect was more pronounced in the full atmosphere model than in the other test models. This may be related to how fast the perturbed velocity caught up to the sound speed of the atmosphere.

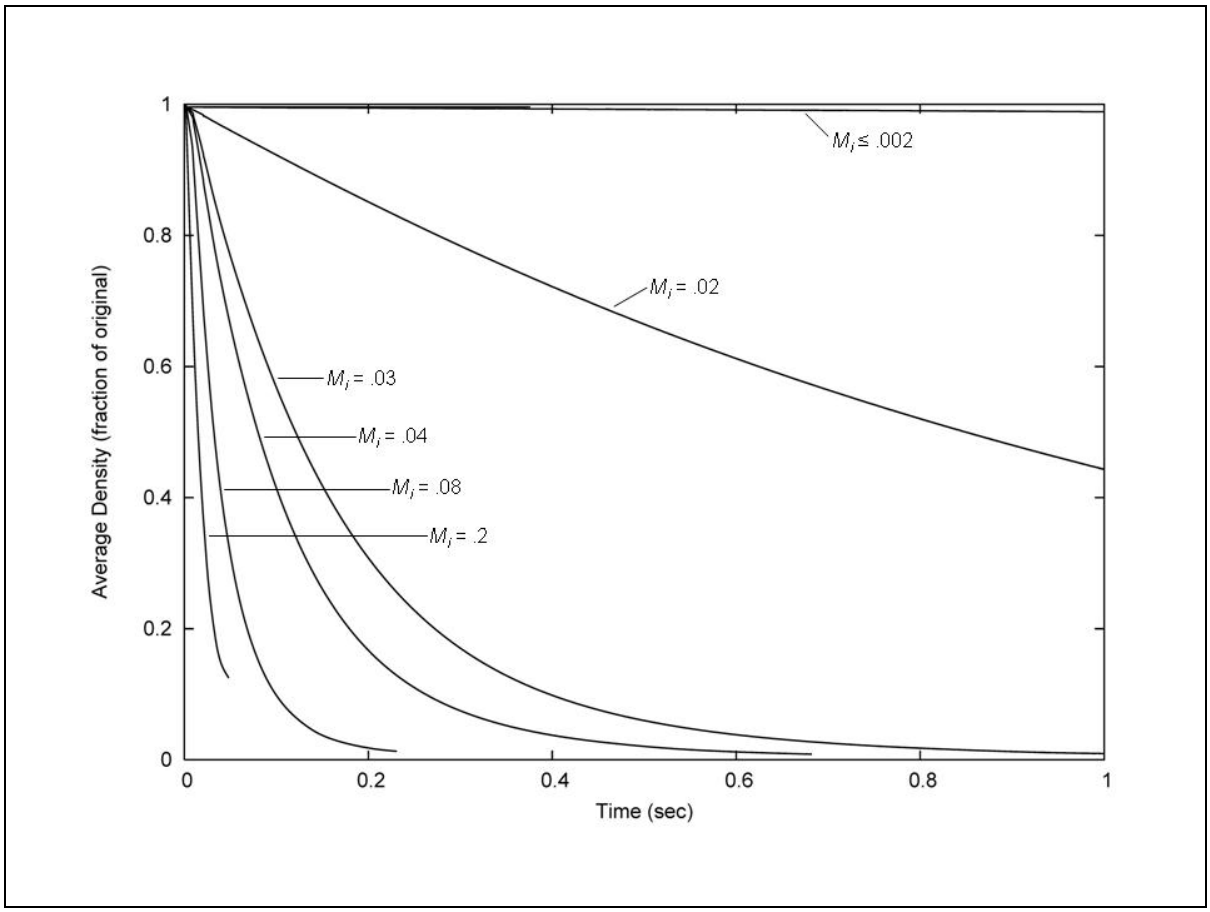

Figure 4.36 - Average density in the volume (r=20 to 240 km) over time. The M_i = .04, .08 and .2 simulations stopped early, apparently because the density next to the oscillating boundary dropped completely to zero and caused a divide by zero error (though the average densities shown in this figure did not).

Energy Dissipation

In the full atmosphere, we observe the now familiar energy dissipation profile associated with a shocked wave and subsequent amplitude decay, shown in Figure 4.37 for a .02 Mach simulation. This energy dissipation profile was typical for all of the simulations performed. For larger perturbations, energy dissipation began at a smaller radius because the full shock formed sooner, and the peak rate of dissipation was larger because the amplitude

was larger. Conversely, for smaller perturbations, dissipation began at a larger radius and the peak rate was smaller. The energy dissipation rate profiles, such as that shown in Figure 4.37, were all steady in time. The average energy dissipation rate in the volume for different size perturbations is shown in Figure 4.38.

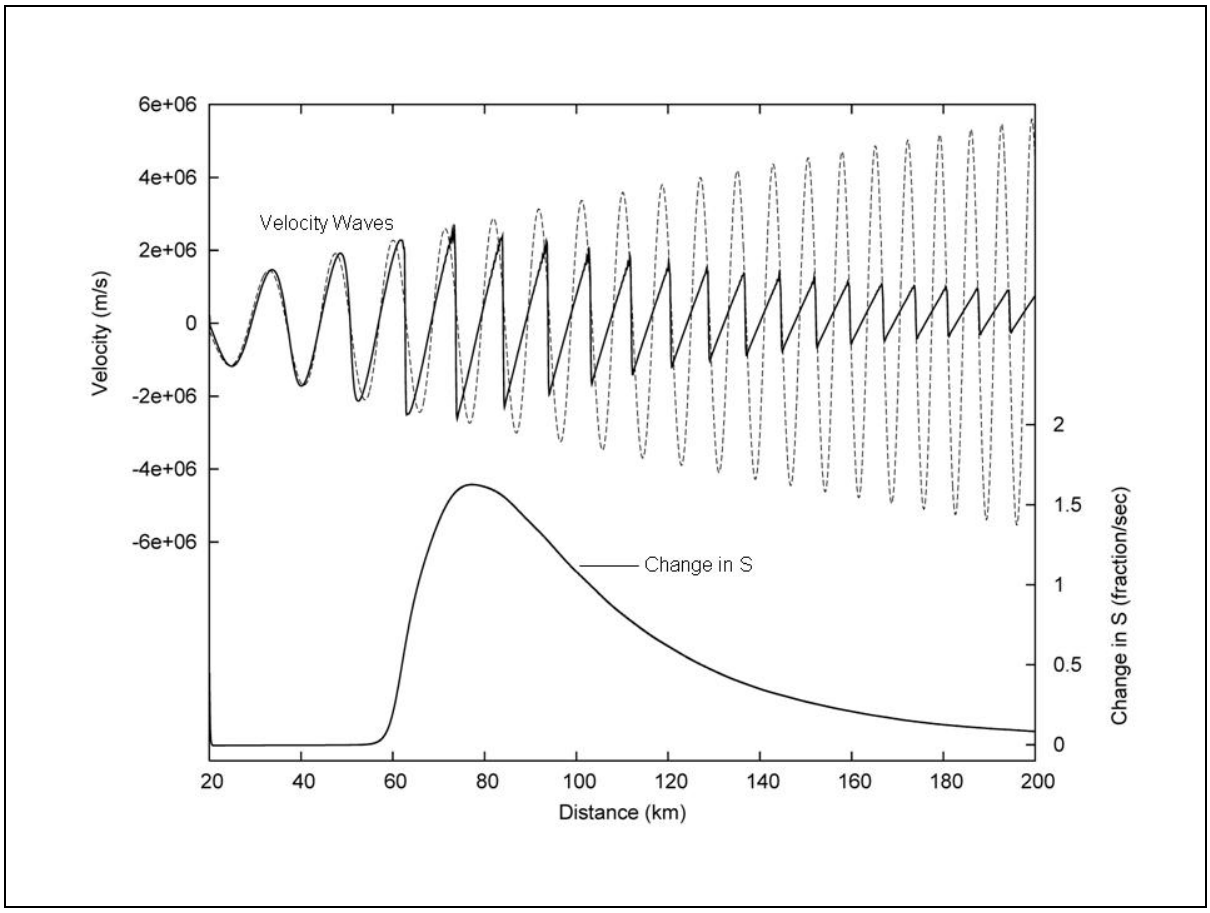

Figure 4.37 - The energy dissipation rate (represented by the change in S) is shown for a Mach 0.02 perturbation. Velocity waves from both the numerical simulation (solid line) and linear analysis (dashed line) are shown.

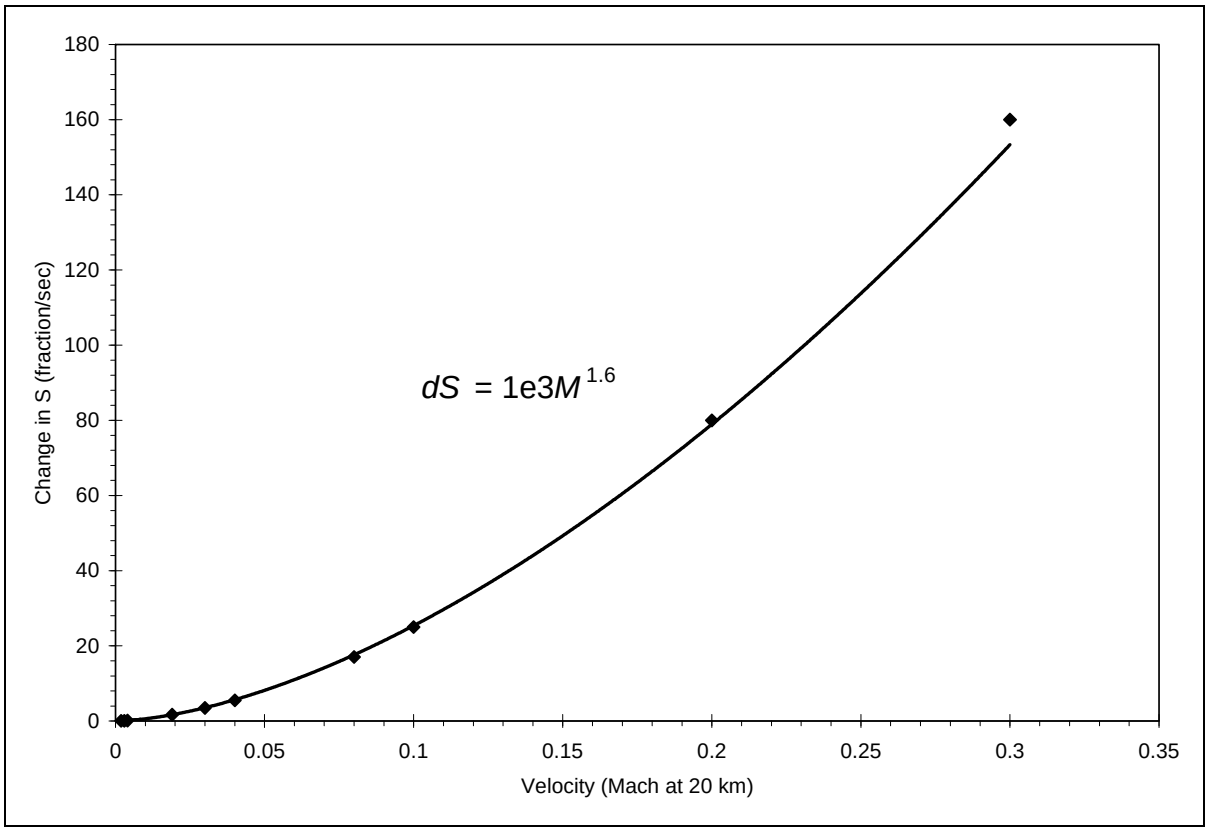

Figure 4.38 - The peak energy dissipation rate (represented by the change in S) is shown for several Mach values. In the best-fit equation, *dS* represents the energy dissipation rate (fraction/sec) and *M* represents the Mach number.

Frequency

According to Foglizzo et al. [2007], the SASI is not driven by standing acoustic waves because acoustic waves will not propagate in the post-shock region at such a low frequency, but according to the dispersion relation that was just derived, there is no restriction on ω. According to Blondin et al., the SASI oscillates around 40 rad/sec [Blondin 2003], so numerical simulations were run down to 20 rad/sec. In all cases, waves propagated successfully. A "snapshot" from the $\omega = 1{,}000$ rad/sec simulation is shown in Figure 4.39. This image also demonstrates how the wavelength decreases with radius. The total

wavelength from the 20 km face of the PNS was a little over 150 km. For $\omega = 40$ rad/sec, the wavelength was about 1200 km.

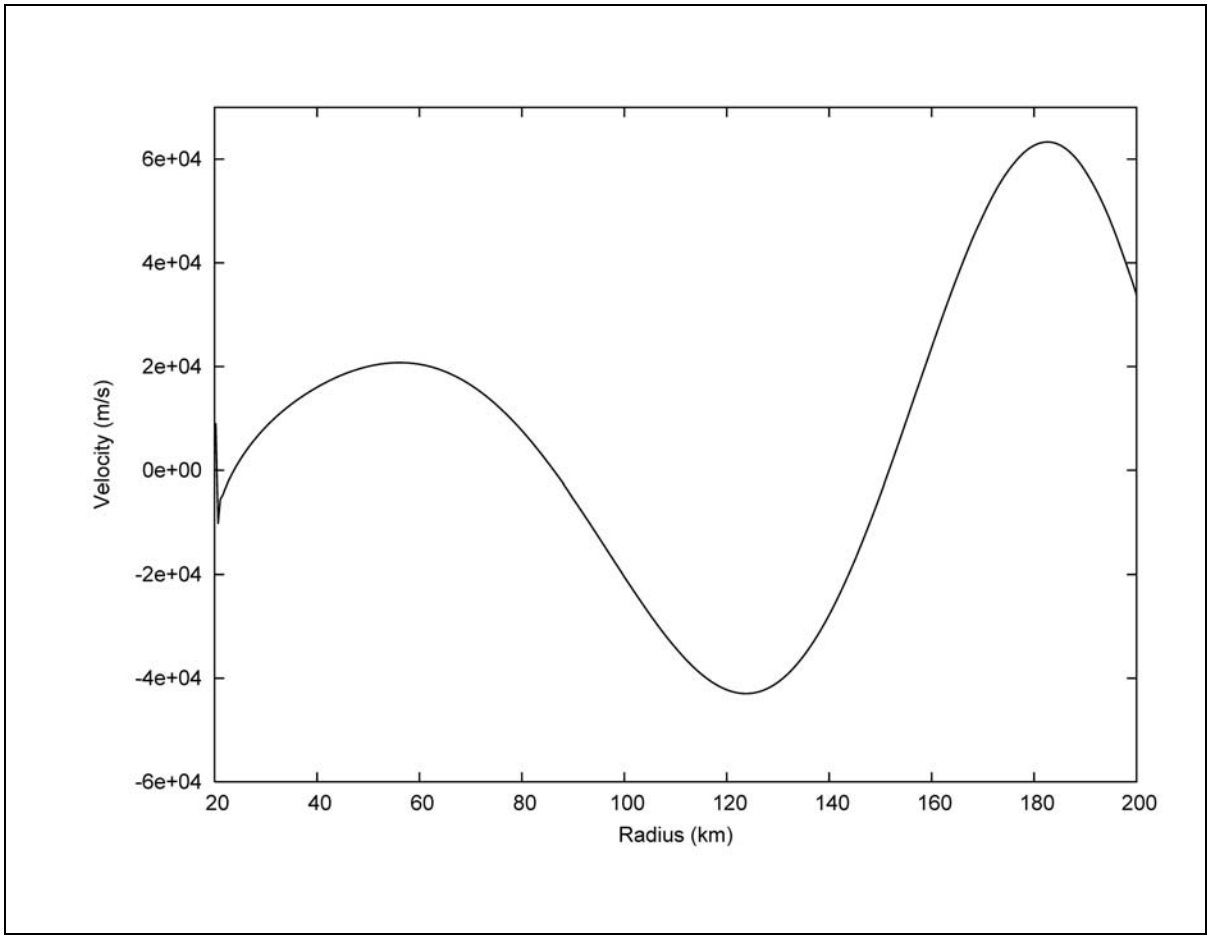

Figure 4.39 – The velocity wave for a 1,000 rad/sec oscillation is shown. Frequencies down to 20 rad/sec were tested, and all waves propagated successfully.

Chapter 5 - Full Coupled Model

5.1 Description

The "coupled model" was used to investigate how dynamic coupling between the PNS and the post-shock atmosphere affected PNS oscillations and subsequent acoustic energy dissipation. Because of the complexity of the problem, these dynamics could only be investigated numerically. Many of the results found in the full atmosphere test case also apply to the coupled model. A key difference between the models is that the oscillations in the PNS were not driven continuously. In the coupled model, the PNS was initially perturbed and then lost energy as acoustic waves were driven into the atmosphere. As a result, the oscillation amplitude decreased over time and the acoustic energy decreased with it. In an actual supernova, it has been suggested that the PNS oscillations are maintained by turbulence in the surrounding atmosphere [Burrows 2006], which is what was assumed in the four atmospheric test models. Whether or not this is a realistic assumption is beyond the scope of this paper.

Simulations were performed in one and two dimensions on a spherical grid. Each model included the PNS and post-shock atmosphere in hydrostatic equilibrium. Self gravity was also calculated in these models. The PNS was modeled as a polytropic star of index $n=\frac{2}{3}$ (equivalent to a polytropic gamma of 2.5). The adiabatic gamma for the PNS was 2.5 and for the post-shock atmosphere was $\frac{4}{3}$. The adiabatic gamma was smoothed over a 9 km region near the surface of the PNS. The background density for the post-shock atmosphere was defined by the Chevalier/Janka model (equation (2.3)), and the background pressure

profile was established to balance the self gravity of the system (close to equation (2.4)). These background values are shown in Figure 5.1.

Establishing hydrostatic equilibrium at the interface between the PNS and the atmosphere was problematic. A satisfactory solution was ultimately found by running a series of simulations with a damping function and using time averaged results. In the final version, small disturbances occurred initially at the interface, but the Mach value of the biggest disturbance was about 3e-4, which had little effect on the energy measurements or qualitative results.

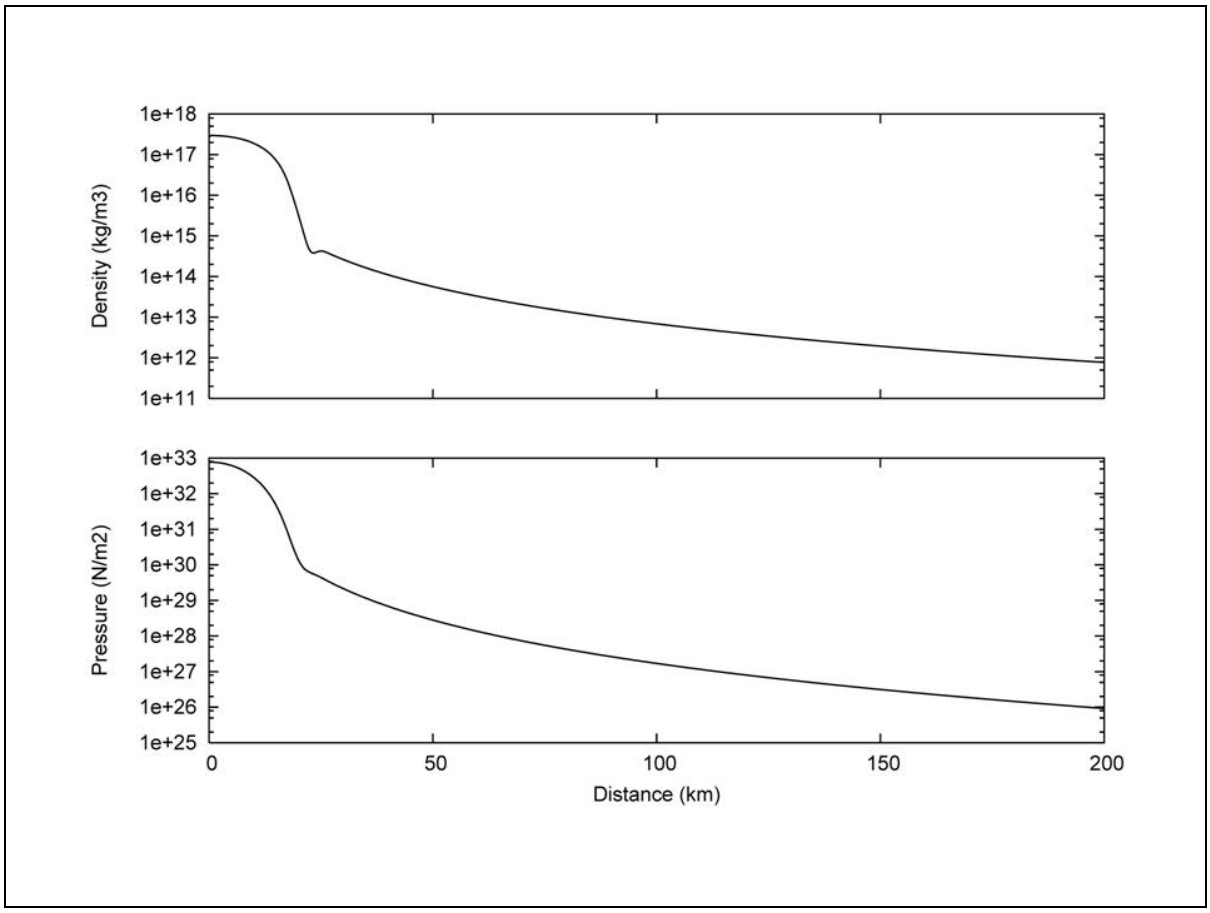

Figure 5.1 - Initial density and pressure. A dip in the density at the PNS surface formed when developing the hydrostatic profile. This dip may be tied to the change in adiabatic gamma and background sound speed, though it did not impact the results and was not further investigated.

5.2 Analysis

In the following analyses, the size of the perturbation was characterized by the acoustic wave Mach number at the surface of the PNS.

PNS Oscillation Modes and Frequency

Using the coupled model with realistic density, pressure and gamma profiles, allowed the oscillation modes and frequency of the PNS to be determined. In the 2D simulations previously performed in a thin atmosphere (where the PNS was essentially in isolation), the L0 mode was preferred by the PNS, and non-radial modes would eventually evolve into a purely radial mode. In 2D simulations performed in the coupled model, l=2 and l=4 modes oscillations continued throughout the simulation. All radial harmonics higher than 1st order died out within just a few milliseconds, which was also seen in the 1D analysis discussed in Chapter 3. Both l=2 and l=4 modes can be seen in Figure 5.2.

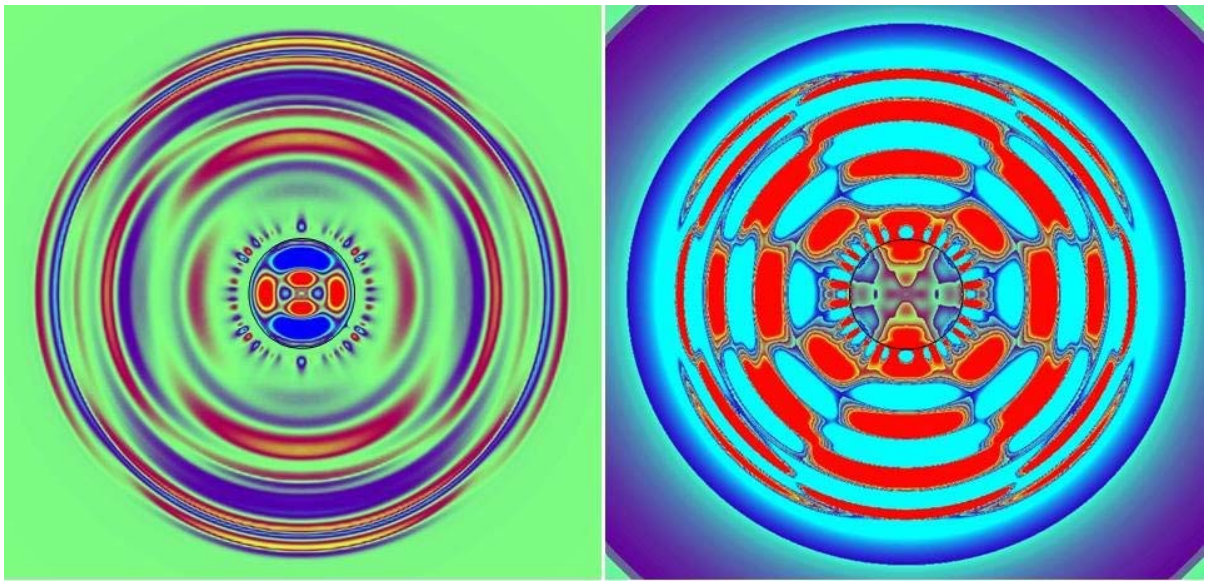

Figure 5.2 - Velocity wave results are shown from 2D simulations for l=2 (on the left) and l=4 (on the right) modes. The color schemes were chosen to highlight the l=2 and l=4 behavior of each simulation. The l=2 image is a composite of two color schemes, one for the acoustic waves and one for the PNS to enhance visibility. The PNS in each image was outlined in black to make it more visible. The l=2 simulation is a 2nd harmonic oscillation, which can be seen in the PNS image. The image is shown in the early stages of the oscillation when this harmonic was still present. The 2nd harmonic died out rapidly in the simulation ultimately leaving only the 1st harmonic.

Based on these results, it seems most likely that the PNS would settle into 1st order oscillations though non-radial modes are possible. The fundamental radial oscillation frequency for the PNS was measured in both 1D and 2D numerical simulations to be about 12k rad/sec. Even these fundamental radial oscillations were observed to decay rapidly. Useful oscillations (i.e. within a couple of orders of magnitude) died out in 30-50 ms, depending on the size of the initial perturbation. Radial oscillations were sustained longer in the PNS tests discussed in Chapter 3, because the surrounding atmosphere was very thin. This result supports the premise that the decreasing PNS amplitude was largely due to energy loss to the atmosphere, as opposed to internal dissipation or numerics. The magnitude of this effect can be approximated by considering equation (3.8) that describes the total oscillation energy in the PNS, and the rate of energy transport (P) by an acoustic plane wave (using the linear approximation for acoustic energy by Lighthill [2005]):

$$P = \tfrac{1}{2}\rho u_0^2 A c_s, \tag{5.1}$$

where A is the area, in this case $4\pi r^2$. Dividing the total energy by the transport rate, we obtain a rough idea how long it takes to empty the PNS oscillation energy into the atmospheric wave energy. The result of this division is

$$t = \frac{.36M}{8\pi\rho R^2 c_s},$$

where M is the mass of the PNS, R is the radius of the PNS and ρ is 1.25e15 kg/m^3 , the atmospheric density just outside the PNS. This equates to t=1.5 ms, which is an extremely short time. This result does not take into account non-linear effects of the PNS or the atmosphere.

In the computer simulation, the transfer of energy followed an exponential decay with time. Figure 5.3 shows the decreasing amplitude of wave oscillations at the surface of the PNS with a best-fit exponential curve, which has a decay timescale of 7.2 ms. Using this result, we can find that the velocity amplitude drops by one order of magnitude in 15 ms. As the energy scales as the square of the velocity, the energy would then drop by two orders of magnitude in the same time frame.

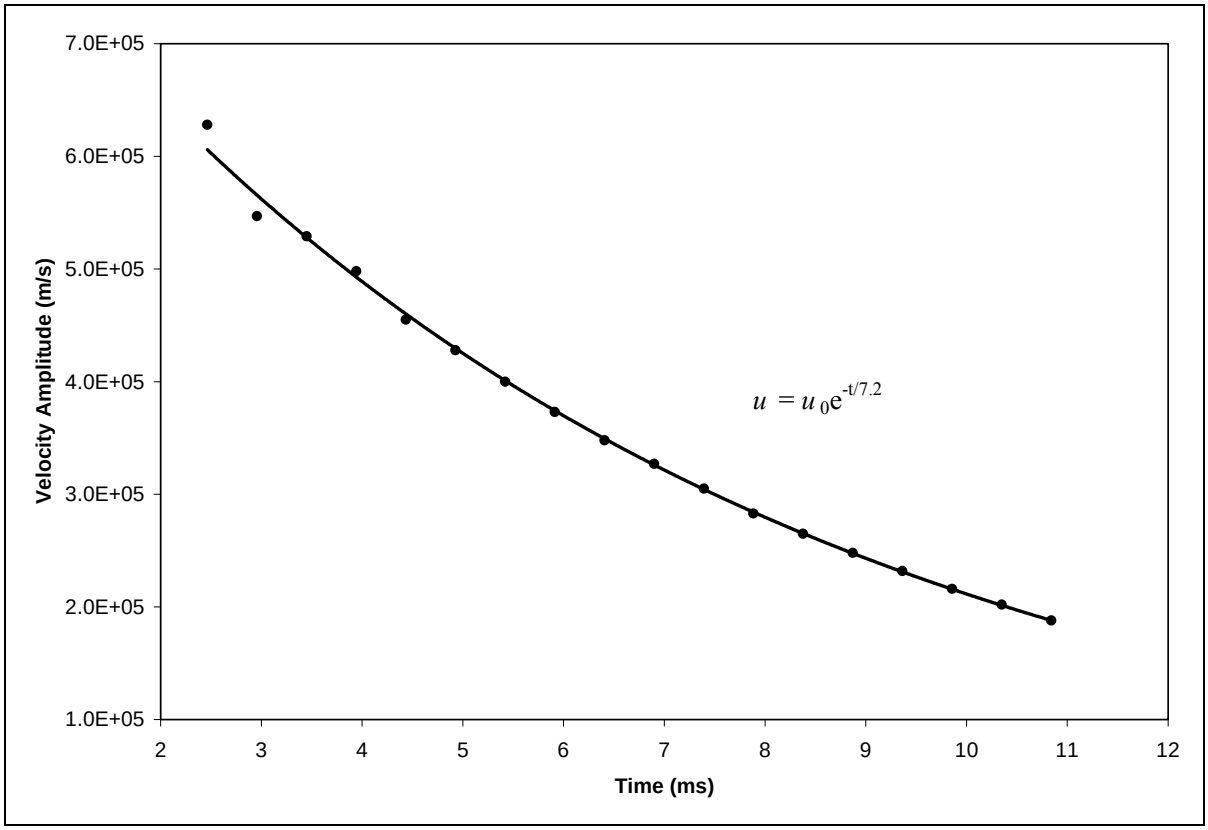

Figure 5.3 - Velocity amplitude decay at the surface of the PNS for a 1D simulation. The initial perturbation was equivalent to Mach .01. The exponential decay rate had a decay timescale of 7.2.

This result generally agrees with the 30 ms time frame observed, as the amplitude would drop two orders of magnitude in this time. This highlights how quickly the PNS will lose oscillation energy in the full model without some mechanism to replace it.

Bulk Motion

The bulk motion observed in the coupled models was essentially the same as that observed in the full atmosphere test model (section 4.5). In addition to this bulk motion, large perturbations also ejected mass from the PNS into the atmosphere. This appeared to occur only when the PNS was initially perturbed, and only for a few oscillations. At Mach 1.0, about 0.5% of the PNS was initially ejected, and this amount became negligible at lower Mach values tested.

Energy Dissipation

The rates of energy dissipation by acoustic waves in a realistic atmosphere were satisfactorily quantified in Section 4.5. The pattern of shock formation and energy dissipation that was seen in Section 4.5 was repeated in the 1D and 2D coupled models, which are shown in Figures 5.4 and 5.5 respectively, for a Mach .01 perturbation.

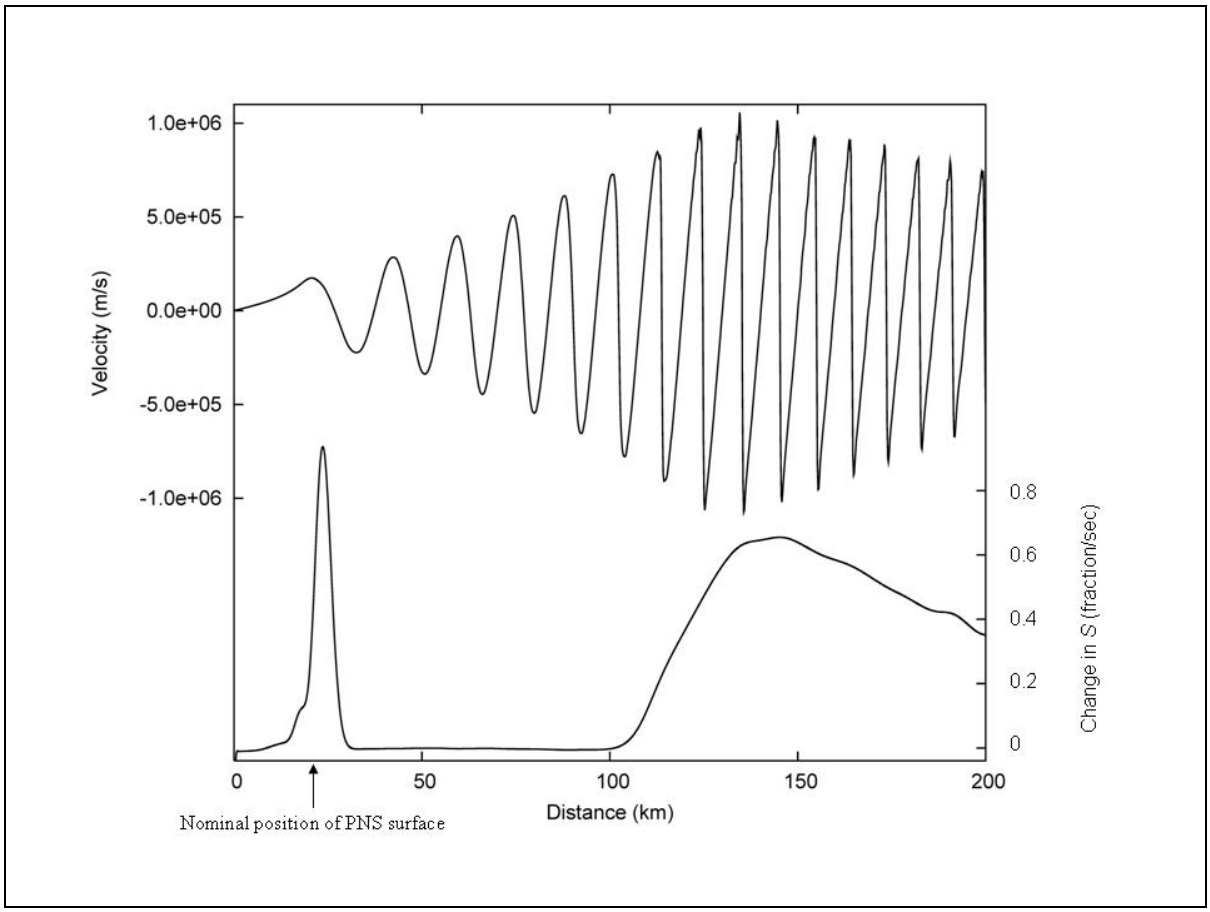

Figure 5.4 - Results from a 1D coupled model simulation for a Mach .01 perturbation. Velocity waves show the characteristic steepening and shock formation. The energy dissipation rate is shown below the velocity. A spike in energy dissipation can be seen at the face of the PNS and then again where shock waves have developed.

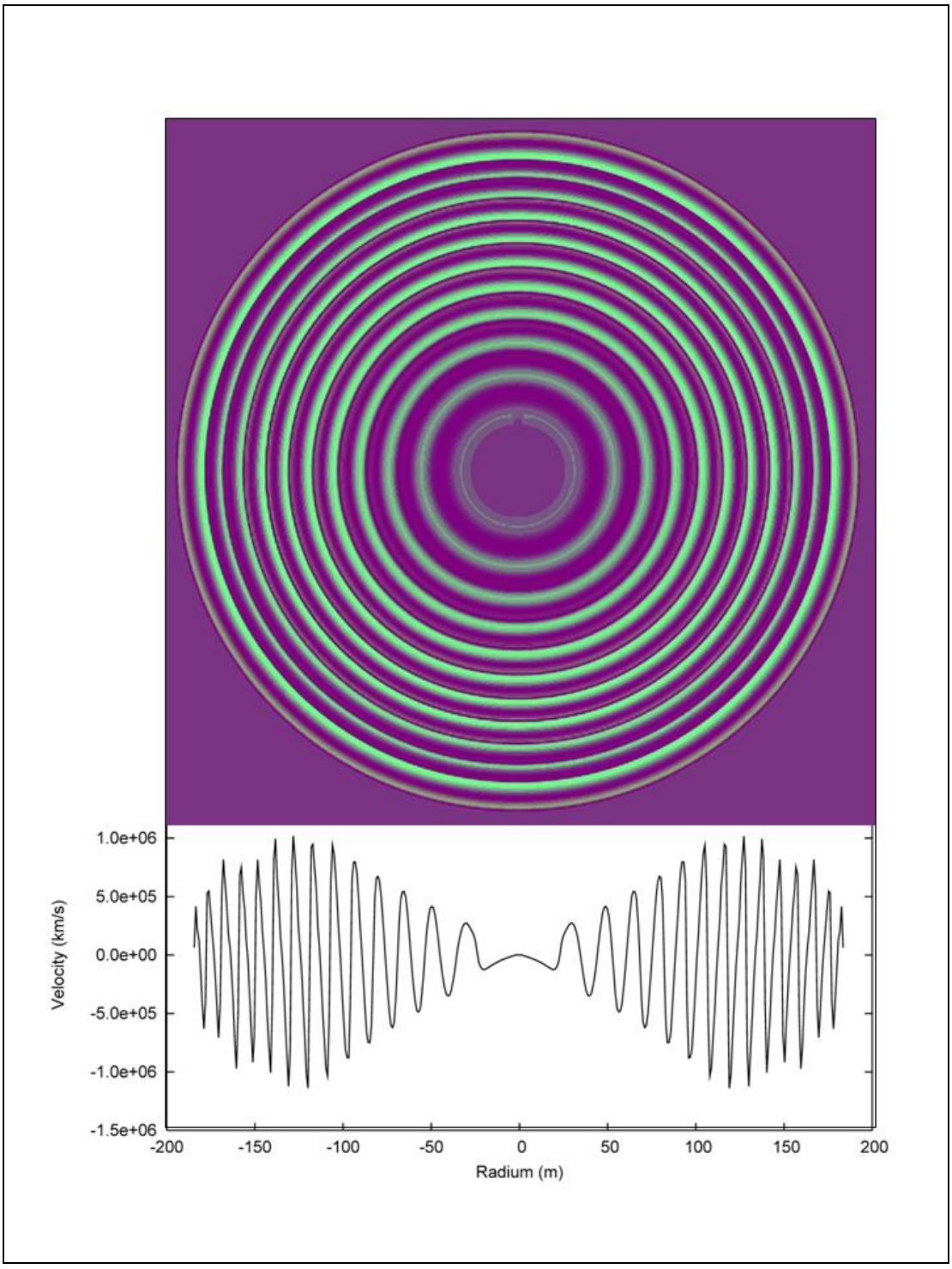

Figure 5.5 - Velocity wave results from a 2D coupled model simulation with Mach .01 radial oscillations. The bottom plot is a slice through the center of the star showing wave steepening and subsequent amplitude decay.

In these figures, the shock begins in earnest around the 140 km mark. Though it is difficult to define the exact radius where shocks fully formed, using the peak amplitude as an indicator of this point, the radius of shock formation was recorded for several perturbations and plotted versus Mach number. The results, which are shown in Figure 5.6, indicate that perturbations at the PNS surface had to be greater than Mach .004 for the wave to develop into a shock before reaching the radius of the stalled accretion shock.

Figure 5.4 also show an energy dissipation spike at the face of the PNS. This spike occurred where the atmosphere was forced back and forth by the oscillating PNS face, an effect which was also seen at the oscillating boundary for atmospheric Test Cases 1 and 3. These are also the test cases that had significant bulk movement. A closer look at the acoustic wave at this point showed kinks in pressure, density and velocity that are too small to show up in Figure 5.4. It is not clear what the source of this energy dissipation spike is, but further testing to investigate its cause did not seem warranted. The region near the PNS surface is complex, and this research is focused more on energy deposition into the rest of the post-shock region. In the region just outside the neutrinosphere, neutrinos escape to cool the star, mass accretes onto the PNS and matter properties dynamically change. For all of these reasons, it is unrealistic to represent energy transfer in this narrow region with just the hydrodynamic model.

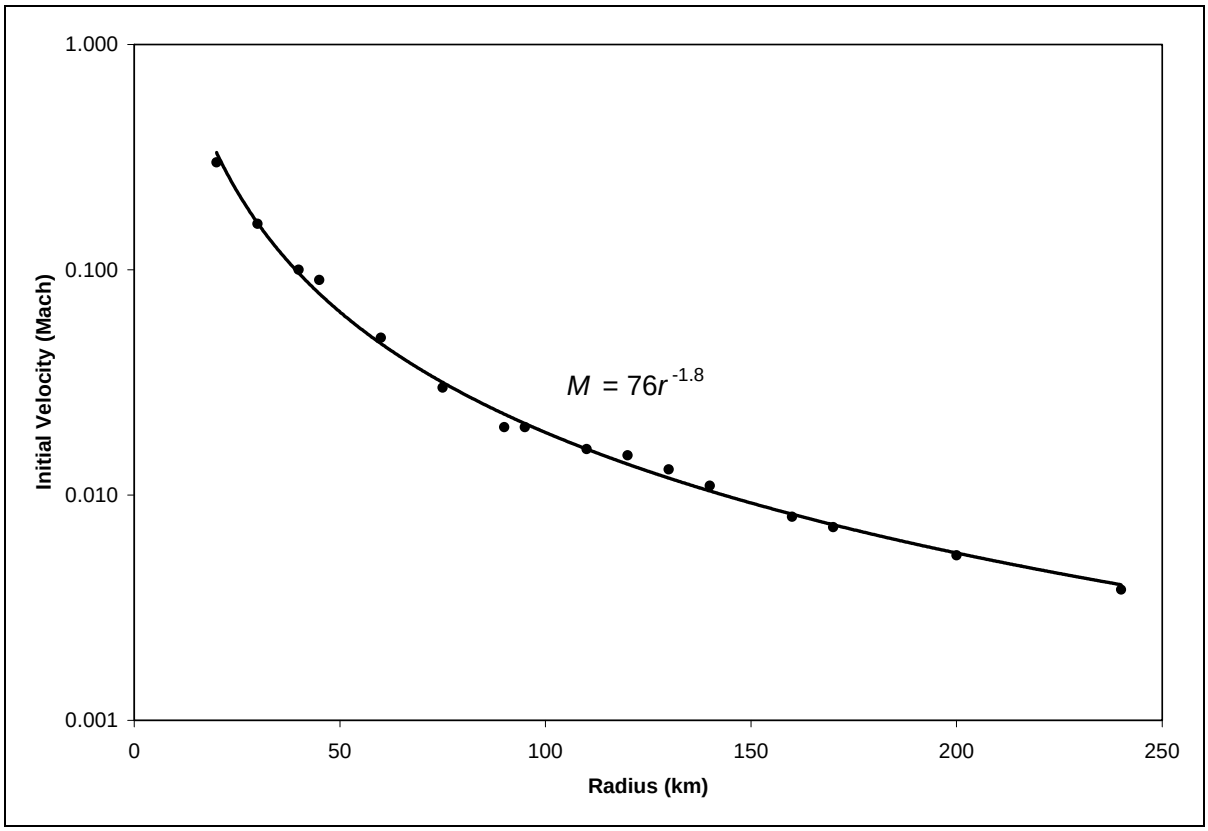

Figure 5.6 - Radius where shocks form as a function of Mach number. The point where velocity amplitude began to decrease was used to define this point. In the best fit equation shown, *M* is the Mach number and *r* is the radius in km.

Chapter 6 – Summary and Conclusions

The essential questions addressed by this paper are:

1. How much energy can be transferred from an oscillating PNS to the post-shock atmosphere as thermal energy?
2. Where in the region will the thermal energy be deposited?
3. Will this thermal energy help to restart the stalled accretion shock?

The final energy picture is an interesting one. Before describing this picture, I will summarize the findings that are needed to address these questions.

6.1 Summary of Results

A wide range of results were found in the atmospheric test cases, demonstrating how different background conditions, especially density and pressure profiles, produce significantly different results with regard to acoustic waves and energy dissipation. Figure 6.2 provides an overview of the conditions and energy dissipation results that were found in these test cases. Of note are: 1) That the atmosphere was severely pushed out above Mach .2, especially in Test Cases 3 and 4 such that reasonable data were not collected much above this point; 2) the dissipation rate varied a great deal depending on the background conditions. Some cause and effect relationships that were reviewed in the body of this paper are summarized below. These items are noted in the velocity wave and energy dissipation results for the full atmosphere model shown in Figure 6.1.

- Velocity waves initially increase in amplitude as they progress because the background density decreases. The spherical nature of the problem works to reduce wave amplitude, but the overall result, as can be seen in the figure, is for amplitudes to increase. Shocks form sooner as a result of this increasing amplitude.
- The wavelength of these waves decreases with radius because the background sound speed decreases. This also causes shocks to form sooner.
- At the point where shocks form, wave energy is dissipated into the atmosphere as thermal energy, and wave amplitudes begin to decay.
- Thermal energy deposited in the atmosphere tends to remain where it is deposited.

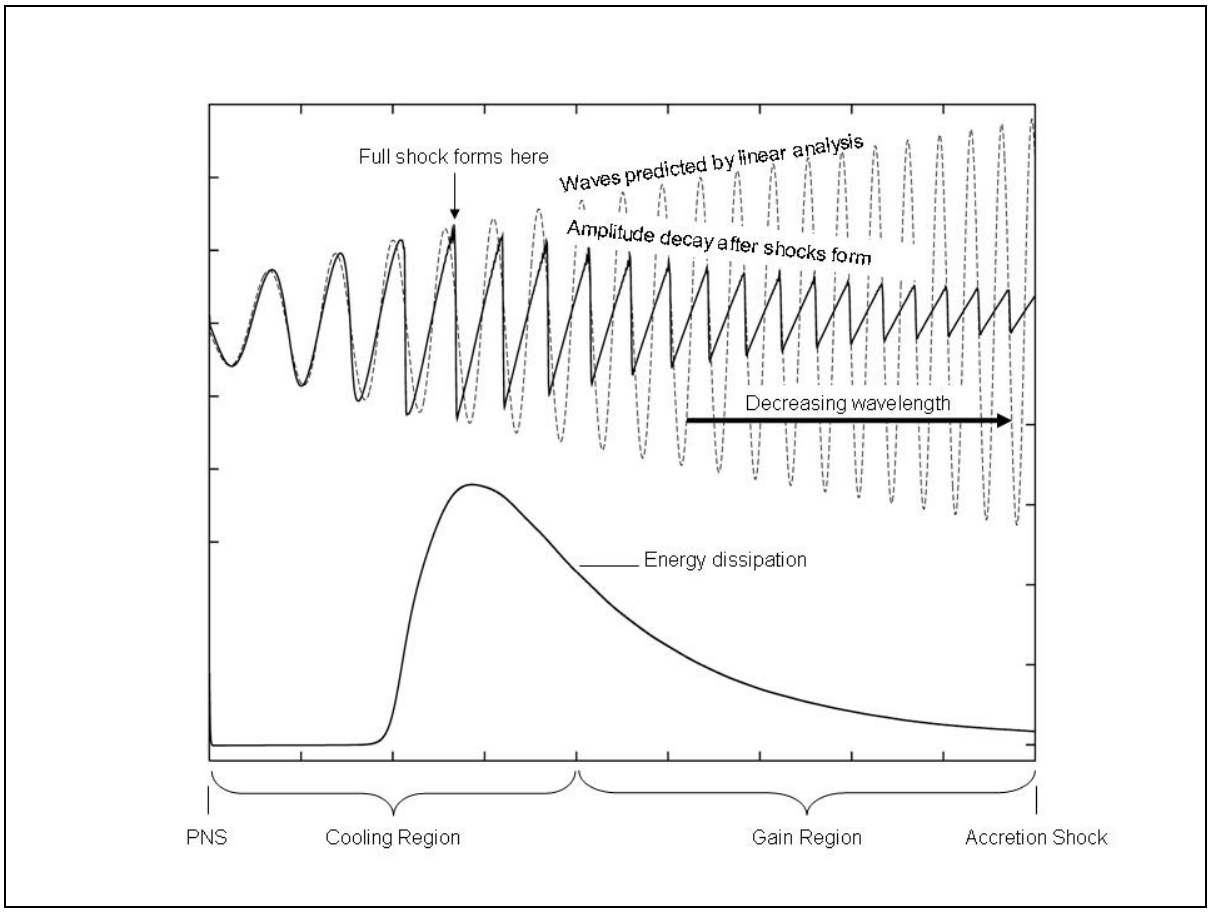

Figure 6.1 - Basic components of an acoustic wave and energy dissipation in the post-shock region are shown for a simulation performed with the full atmosphere test model. The energy dissipation curve in the plot can represent either the dissipation rate or the change in internal energy of the atmosphere.

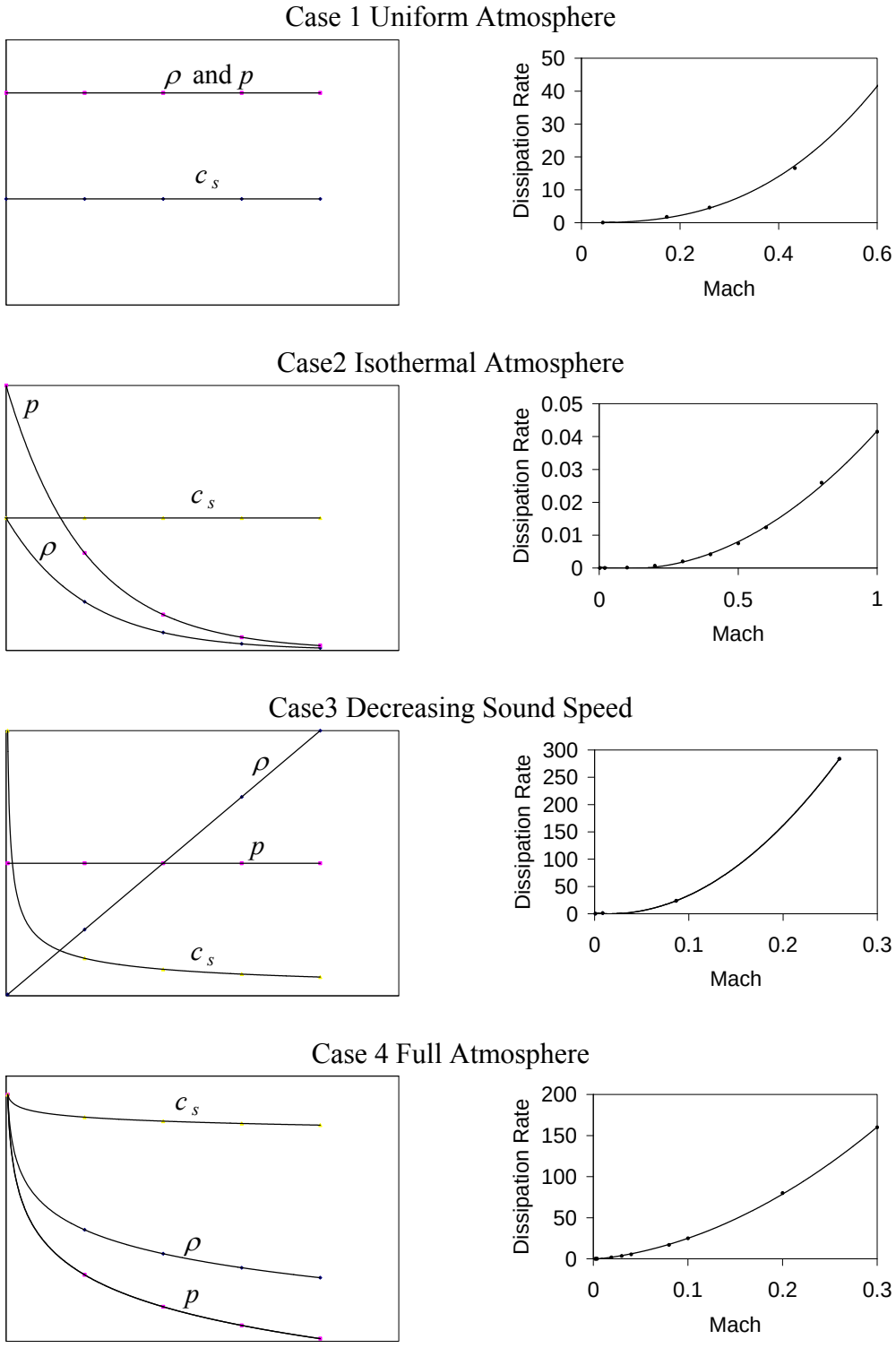

Figure 6.2 - Overview of atmospheric test cases.

6.2 Energy Dissipation and Effect on Restart

The overall energy picture as shown in Figure 6.3 begins with 10^{53} ergs of energy from the gravitational collapse of the star core that forms the PNS. 99% of that energy escapes, so there is about 10^{51} ergs of energy available to explode the star. The PNS is theorized to oscillate from this initial collapse, interaction with infalling matter, turbulence in the surrounding atmosphere or some combination of all three. These oscillations are theorized to drive acoustic waves in the post-shock atmosphere that steepen into shocks and dissipate thermal energy into the atmosphere. This additional thermal energy may assist with the restart of the stalled accretion shock.

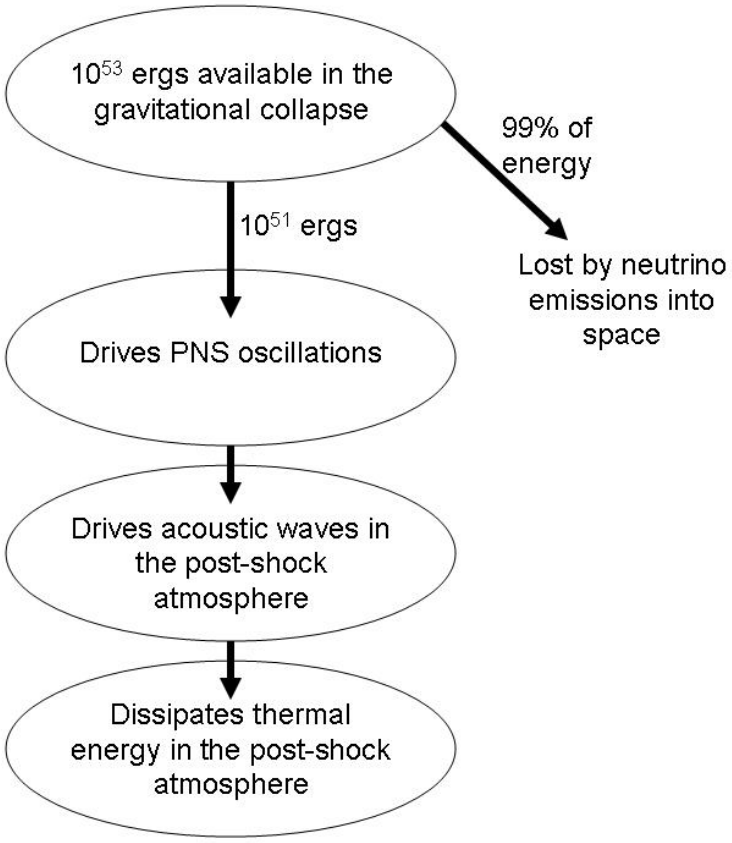

Figure 6.3 - Overall energy picture.

The work in this paper begins with an already oscillating PNS. The results presented tell us that the PNS is likely to oscillate at 12 krad/sec in the fundamental mode and perhaps higher in non-radial modes. The surface velocity of the PNS driving the acoustic waves is a critical aspect to this problem. The magnitude of this oscillation potentially covers a wide range, but can be constrained by a few observations. Some key velocities are shown in Figure 6.4. The available energy of 10^{51} ergs corresponds to an oscillation amplitude of 2e7 m/s (or Mach .4 relative to the atmospheric sound speed at this point), assuming the fundamental radial mode frequency of 12 krad/sec. Even if higher orders or modes are achieved by the PNS, a more limiting issue is that the atmosphere was severely forced away from the PNS at velocities greater than Mach .2. For all practical purposes, this becomes the ceiling.

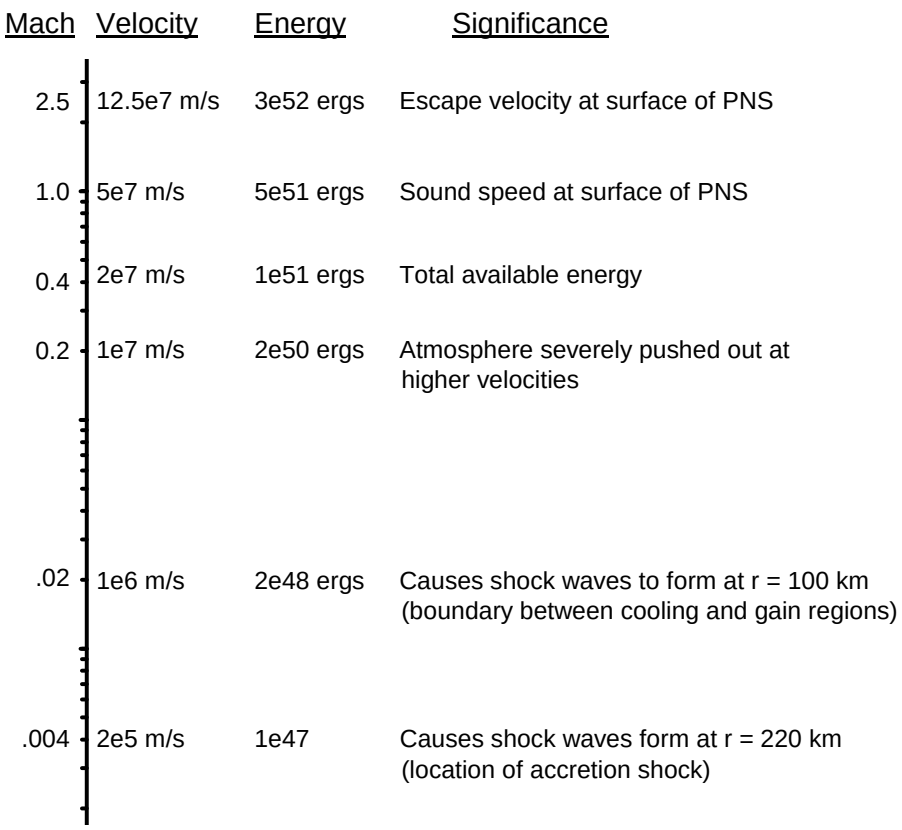

Figure 6.4 - Key velocity amplitude levels are shown along with the PNS oscillation energy required to produce them. These energy values assume that the PNS oscillates with a frequency of 12 krad/sec.

The lower limit is set by the requirement that waves form shocks and dissipate energy before they reach the stalled accretion shock. This lower limit is Mach .004. It is also important to consider where within the post-shock region this energy is dissipated. As was seen throughout this paper, thermal energy was dissipated where shocks developed, and barring mass movement in the post-shock atmosphere that was not captured in these simulations, this thermal energy essentially remains where it is deposited. For example, the system shown in Figure 6.1 deposits most of the dissipated energy into the Cooling Region.

In the Janka model, thermal energy must be added to the Gain Region to assist with expansion of the accretion shock. The Gain Region starts around a radius of 100 km and goes to the accretion shock. A perturbation of Mach .02 produces waves that will turn into shocks around this 100 km point. Therefore perturbations between Mach .004 and .02 will deposit more thermal energy in the Gain Region. Perturbations higher than Mach .02 will deposit more thermal energy in the Cooling Region. Figure 6.5 shows this graphically.

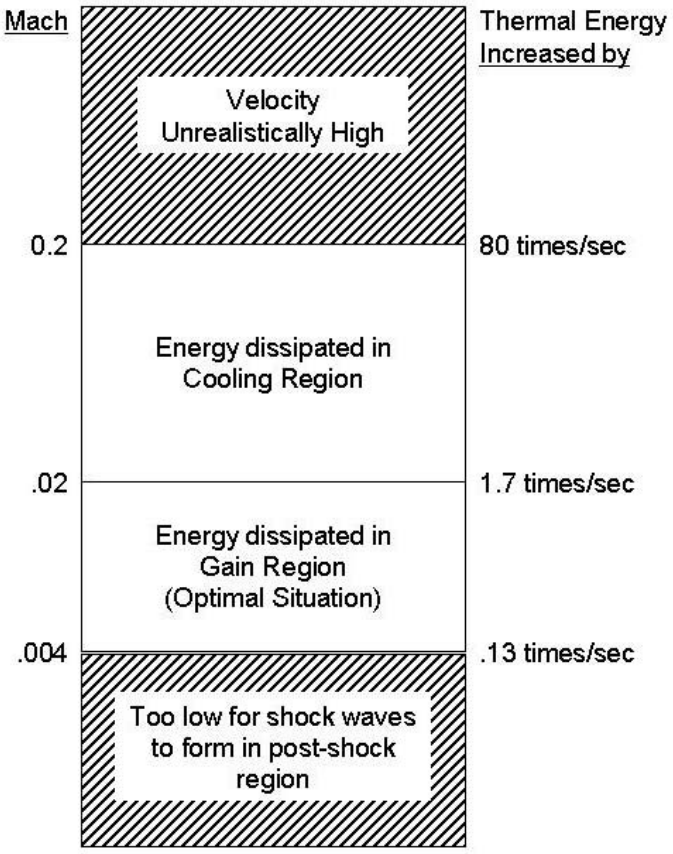

Figure 6.5 – Location of energy dissipation in the post-shock region based on the size of the perturbation (represented by Mach number) and the maximum thermal energy gain in the atmosphere that can be anticipated.

Using the energy dissipation information in Section 4.5, we can define the energy dissipation rates that can be expected at the boundaries of the Cooling and Gain Regions. At the beginning of the cooling region, energy is dissipated at 80 times/sec; at the point between the cooling and gain regions, energy is dissipated at 1.7 times/sec; and at the end of the gain region, energy is dissipated at .13 times/sec. These rates are also shown in Figure 6.5.

This analysis tells us how much the internal energy of the atmosphere may be increased. The fraction of the original PNS oscillation energy that is transferred to acoustic waves and then to thermal energy in the first few milliseconds can also be approximated from the information we have seen. Using the exponential decay rate found in the last chapter (decay timescale of 7.2 ms), the velocity amplitude of the PNS will decrease by 50% in about 5 ms. According to equation (3.7) the energy, T, is proportional to u_0^2, so in the same 5 ms the oscillation energy of the PNS will be reduced to 25% of its original value. Or said another way, 75% of the PNS oscillation energy is lost to acoustic waves in 5 ms. We can similarly analyze the dissipation of this acoustic energy. The amplitude for a typical acoustic wave in the full atmosphere model, such as that shown in Figure 6.1, decreases by 50% in 2 ms. Again, the energy is proportional to the square of the velocity, so 75% of this wave energy is dissipated as heat in 2 ms.

The impact of these dissipation rates in the post-shock atmosphere has yet to be determined. A critical factor is how large the perturbations are as this determines where the energy would be deposited. In the Janka model, if thermal energy is deposited in the Gain Region then this would assist expansion to some degree. On the other hand, if thermal energy is deposited in the cooling region, this may restrict the cooling and settling of mass

into the PNS, which would hinder the restart process. If a range of oscillation amplitudes are to be expected from the PNS throughout the post-bounce phase, then the fact that dissipation rates are higher in the Cooling Region than in the Gain Region must also give one concern.

6.3 SASI

One of the many outstanding supernova questions is what the mechanism is that drives the SASI. Foglizzo contends that the SASI cannot be driven by acoustic waves because low frequency waves will not propagate in the post-shock atmosphere. Recall the SASI frequency is about 40 rad/sec. One of the benefits of the analytical analyses that were performed is that we now have dispersion relations to consider. Using these analytical results (with the caveat that waves were assumed to be linear), the only atmospheric model that showed a restriction on frequency was the isothermal atmosphere. The dispersion relation for the full atmosphere was

$$u_r' \cong Cr^{3/2}\sqrt{\frac{\sqrt{3GM}}{\pi\omega r^{3/2}}}\cos\left(\frac{2\omega}{\sqrt{3GM}}r^{3/2}-\frac{5\pi}{12}\right),$$

which clearly does not have a restriction on frequency. Numerical simulations were conducted down to 20 rad/sec in the full atmospheric test model, and no restrictions on ω were found.

6.4 Numerical Issues

One can anticipate when modeling hydrodynamic systems where shock waves are anticipated that there will be numerical challenges. When reviewing the atmospheric test cases, errors associated with peak shaving, wave spreading and energy measurement were discussed. Numerical error associated with energy measurements is central to this study and will be summarized here.

Convergence analysis showed that the order of convergence for errors in energy measurements ranged between 2.3 and 2.5. The amount of error varied between simulations. In the isothermal model, errors were found to be:

50% for a resolution of 18 zones/WL

25% for a resolution of 36 zones/WL

2% for a resolution of 91 zones/WL

In the full atmosphwere model, errors were found to be:

10% for a resolution of 23 zones/WL

4% for a resolution of 38 zones/WL

2% for a resolution of 76 zones/WL

1% for a resolution of 151 zones/WL

As can be seen, achieving results with a 1% accuracy can be very expensive computationally. Even a resolution such as 18 zones/WL may still be computationally expensive when considering the full spatial scale of the model. In the atmospheric full model, there were about 16 wavelengths in a 200 km span, which means that the full spatial resolution would be 288 zones. This value would increase if the model went beyond the

accretion shock and high frequency waves needed to be captured, or if the accretion shock moved to a larger radius (which is exactly what would happen with a successful explosion. While energy measurements may not always demand 1% accuracy and 91+ zones/WL, it must be a consideration.

REFERENCES

Abramowitz, Milton and Stegun, Irene A. 1972, *Handbook of Mathematical Functions*, Dover Publications, Inc., Chapter 10: *Bessel Functions of Fractional Order*.

Bethe, H. A., Brown, G. E., Applegatge, J. and Lattimer, J. M. 1979, *Nuclear Physics*, A324: 487-533

Bethe, H. A. and Wilson, J. R. 1985, *Astrophysical Journal*, 295: 14-23

Bethe, H. A. 1993, *Astrophysical Journal*, 412, 192.

Blondin, John M., Mezzacappa, Anthony, Demarino, Christine 2003, *Astrophysical Journal*, 584:971-980.

Blondin, John M., Shaw, Samantha, 2007, *Astrophysical Journal*, 656: 366-371.

Burrows, Adam, Livne, Eli, Dessart, Luc, Ott, Christian D. and Murphy, Jeremiah 2006, *Astrophysical Journal*, 640: 878-890.

Chevalier, R. A. 1989, *Astrophysical Journal*, 346, 849.

Clarke, C.J. and Carswell, R.F. 2007, *Principles of Astrophysical Fluid Dynamics, Cambridege University Press*, Section 6.6 *Propagation of Sound Waves in a Stratified Atmosphere*.

Colella, P., and Woodward, P. R. 1984, J. Comp. Phys., 54, 174.

Colgate, S. A. and White, R. H. 1966, *Astrophysical Journal*, 143, 626.

Cox, John P. 1980, *Theory of Stellar Pulsation*, Princeton University Press.

EqWorld website, (n.d.) Retrieved May 8, 2008, Website location: Institute for Problems in Mechanics, Russian Academy of Sciences, Moscow, Russia, Website address: http://eqworld.ipmnet.ru/, *Second-Order Linear Ordinary Differential Equations*.

Foglizzo, T., Galletti, P., Scheck, L. and Janka, H-Th., 2007, *Astrophysical Journal*, 654: 1006-1021.

Fryer, C. L., Benz, W., and Herant, M. 1996, *Astrophysical Journal*, 460, 801.

Hansen, Carl J. and Kawaler, Steven D. 1994, *Stellar Interiors*, Springer-Verlag New York, Inc.

Herant, M., Benz, W. and Colgate, S. A. 1992, *Astrophysical Journal*, 395: 642

Janka, H.-Th., 2001, *Astronomy and Astrophysics*, 368: 527-560.

Lighthill, James 2005,*Waves in Fluids*, Cambridege University Press

LeVeque, Randall J. 1992, *Numerical Methods for Conservation Laws*, Section 5.1.2 *Entropy*

Press, William H., Teukolsky, Saul A., Vetterling, William T. and Flannery, Brian P. 2001, *Numerical Recipes in Fortran 77, The Art of Scientific Computing*, Cambridge University Press.

Shu, Frank H., 1992, *The Physics of Astrophysics Volume II Gas Dynamics*, University Science Books, 205.

Williams, Thomas and Kelley, Colin 2007, *Gnuplot*

APPENDIX

Polytropic Star Model

A polytropic star model describes the pressure and density of a self gravitating star, where the state variables are independent of temperature so that the equation of state is of the form:

$$p = K\rho^{\left(\frac{n+1}{n}\right)},$$

where p is the pressure, ρ is the density, K is a constant and n is the polytropic index. This equation of state is then combined with the equation of hydrostatic equilibrium:

$$\frac{dp}{dr} = -\rho\frac{d\Phi}{dr},$$

where Φ is defined by Newton's equation of gravitational potential:

$$\nabla^2\Phi = 4\pi G\rho$$

resulting in the Lane-Emden equation:

$$\frac{d^2\omega}{dz^2} + \frac{2}{z}\frac{d\omega}{dz} + \omega^n = 0,$$

where ω is the dimensionless potential, z is the dimensionless radius and n is the polytropic index.

By solving the Lane-Emden equation for a given polytropic index, pressure, density and radius are then calculated from the following relationships:

$$\rho = \rho_c\omega^n$$

$$p = p_c\left(\frac{\rho}{\rho_c}\right)^{\left(\frac{n+1}{n}\right)}$$

$$r = z\sqrt{\frac{p_c(n+1)}{4\pi G\rho_c^2}},$$

where ρ_c and p_c are the density and pressure at the center of the star.